[American Journal of Science, Vol. 321, May, 2021, P. 579–642, DOI 10.2475/05.2021.03]

PRESENTATION AND APPLICATIONS OF MIXING ELEMENTS AND DISSOLVED ISOTOPES IN RIVERS (MEANDIR), A CUSTOMIZABLE MATLAB MODEL FOR MONTE CARLO INVERSION OF DISSOLVED RIVER CHEMISTRY

PRESTON COSSLETT KEMENY*,† and MARK ALBERT TORRES**

ABSTRACT. The dissolved chemistry of rivers has been extensively studied to elucidate physical and climatic controls of chemical weathering at local to global spatial scales, as well as the impacts of chemical weathering on climate over short to geologic temporal scales. Within this effort, mixing models with Monte Carlo uncertainty propagation are a common tool for inverting measurements of dissolved river chemistry to distinguish among contributions from end-members with distinct elemental and/or isotopic compositions. However, the methods underlying prior river inversion models have typically been opaque. Here we present Mixing Elements ANd Dissolved Isotopes in Rivers (MEANDIR), a set of MATLAB scripts that enable highly customizable inversion of dissolved river chemistry with Monte Carlo propagation of uncertainty. First, we present an overview of the mathematics underlying MEANDIR. This overview includes, among other topics, derivation of equations for mass balance, implementation of chlorine critical values, construction of cost functions, normalization to the sum of dissolved variables, quantification of river sulfate sourced from pyrite oxidation, resolution of petrogenic organic carbon oxidation, representation of secondary phase formation with isotopic fractionation, and calculation of the impact of weathering on atmospheric carbon dioxide. Second, we apply MEANDIR to five previously published datasets to demonstrate the sensitivity of results to parameter choices. We invert data from two global compilations of river chemistry (Gaillardet and others, 1999; Burke and others, 2018), the major element chemistry and sulfate sulfur isotope ratios of rivers in the Peruvian Amazon (Torres and others, 2016), the major element chemistry of Icelandic rivers (Gíslason and others, 1996), and the major and trace element chemistry of water samples from the Mackenzie River (Horan and others, 2019). MEANDIR and its user guide are freely available online.

Key words: River inversion, river geochemistry, chemical weathering, sulfide oxidation, petrogenic organic carbon, RZC, pCO_2

INTRODUCTION TO MEANDIR

Chemical weathering modulates the partial pressure of atmospheric carbon dioxide (CO_2) by sourcing alkalinity (ALK) and dissolved inorganic carbon (DIC) to the coupled ocean-atmosphere system (Gaillardet and others, 1999). Although silicate weathering is generally thought to regulate atmospheric CO_2 over geologic timescales (Urey, 1952; Walker and others, 1981), recent efforts have shown that the negative ALK flux from sulfide oxidation can also substantially impact CO_2 over the duration for which seawater sulfate (SO_4^{2-}) concentrations remain elevated (Spence and Telmer, 2005; Lerman and others, 2007; Calmels and others, 2007; Torres and others, 2016; Burke and others, 2018). Similarly, the oxidation of petrogenic organic carbon (C_{org}) exerts a major influence on atmospheric CO_2 by adding DIC into the ocean-atmosphere system (France-Lanord and Derry, 1997; Bolton and others, 2006; Bouchez and others, 2010; Horan and others, 2019). Because the impact of weathering on the global carbon cycle depends on mineralogy, the relative importance of

* Geological and Planetary Sciences, California Institute of Technology, Pasadena, California, USA
** Earth, Environmental, and Planetary Sciences, Rice University, Houston, Texas, USA
† Corresponding author: pkemeny@caltech.edu, preston.kemeny@gmail.com

acids, and petrogenic carbon fluxes, it is crucial to quantitatively constrain the prevalence and controls of different mechanisms of chemical denudation.

The primary tool for quantifying chemical weathering is measurement of the concentrations ($[Ca^{2+}]$, $[Mg^{2+}]$, $[Sr^{2+}]$, $[Na^{+}]$, $[K^{+}]$, $[Cl^{-}]$, $[SO_4^{2-}]$, [Si], *et cetera*) and isotopic ratios ($^{87}Sr/^{86}Sr$, $^{34}S/^{32}S$, $^{44}Ca/^{40}Ca$, $^{30}Si/^{28}Si$, *et cetera*) of elements dissolved in river water (Stallard and Edmond, 1983; Négrel and others, 1993; Gaillardet and others, 1999; Moon and others, 2014; Burke and others, 2018). By inverting the relative abundance of dissolved variables with knowledge of weathering lithologies, researchers model the provenance of each constituent and the associated weathering fluxes of ALK and DIC (Négrel and others, 1993; Gaillardet and others, 1999). One common form of such inversions takes a Monte Carlo approach to propagation of uncertainty, in which the chemical composition of end-members and samples is varied throughout the calculation in order to constrain the range of possible results. However, Monte Carlo inversion models are subject to many assumptions that alter both the results and the efficiency with which they are attained. As river inversion models expand in scope to utilize large new data sets, such as Hartmann and others (2014), it becomes increasingly important to use efficient, reliable schemes for calculating the fractional contributions of weathering lithologies. Although the nuances of inverting river dissolved load may seem esoteric, these calculations are critical for quantifying the fluxes of ALK and DIC from carbonate and silicate weathering, which are used to calibrate models of the global carbon cycle (Li and Elderfield, 2013; Caves and others, 2016).

Here we introduce Mixing Elements ANd Dissolved Isotopes in Rivers (MEANDIR), a customizable set of MATLAB scripts for inverting the dissolved chemistry of rivers for the fractional contributions of end-members and for constraining the chemical and isotopic compositions of those end-members (fig. 1). The required inputs to MEANDIR are measurements of major or trace element concentrations and isotope ratios, a user-defined set of initial end-member chemical compositions, and choices for how to perform the inversion. In turn, MEANDIR inverts the dissolved observations for the fractional contributions of each end-member to the budget of each dissolved variable; this attribution includes solute sources such as silicate weathering and atmospheric deposition, as well as solute sinks such as the formation of isotopically fractionated secondary phases. By isolating successful simulations following user-defined criteria, the model constrains the chemical composition of each end-member. Moreover, when a pollution end-member is well-defined, MEANDIR is capable of modeling the contributions of anthropogenic inputs to dissolved river data (Berner, 1971). MEANDIR can also utilize a novel normalization strategy to model chemical processes as independent end-members, including sulfide oxidation, organic carbon oxidation, and CO_2 exchange between the atmosphere and river. Furthermore, MEANDIR quantifies the ratio of changes in ALK to changes in DIC associated with chemical weathering upstream of a water sampling site.

MEANDIR allows users to select among different data normalizations, variable combinations of observations and end-members, different types of precipitation corrections, and several standard or custom cost functions for performing the inversion. MEANDIR currently supports inversion of the following variables, where brackets represent concentration and δ represents the normalized isotopic ratio ($R_{sample}/R_{standard}$-1, where R is an isotopic ratio, and δ is typically reported in ‰) following standard conventions: [ALK], [DIC], $[Ca^{2+}]$, $[Mg^{2+}]$, $[Na^{+}]$, $[K^{+}]$, $[Sr^{2+}]$, $[HCO_3^{-}]$, $[Cl^{-}]$, $[SO_4^{2-}]$, $[NO_3^{-}]$, $[PO_4^{3-}]$, [Si], [Ge], $[Li^{+}]$, $[F^{-}]$, [Fe], [B], [Re], [Mo], [Os], δ^7Li, HCO_3^{-} or DIC $\delta^{13}C$ and normalized $^{14}C/^{12}C$ ratio, SO_4^{2-} $\delta^{34}S$ and $\delta^{18}O$, $\delta^{26}Mg$, $\delta^{30}Si$, $\delta^{44/40}Ca$ and $\delta^{44/42}Ca$, $\delta^{56}Fe$, $^{87}Sr/^{86}Sr$, $\delta^{98}Mo$, and $^{187}Os/^{188}Os$.

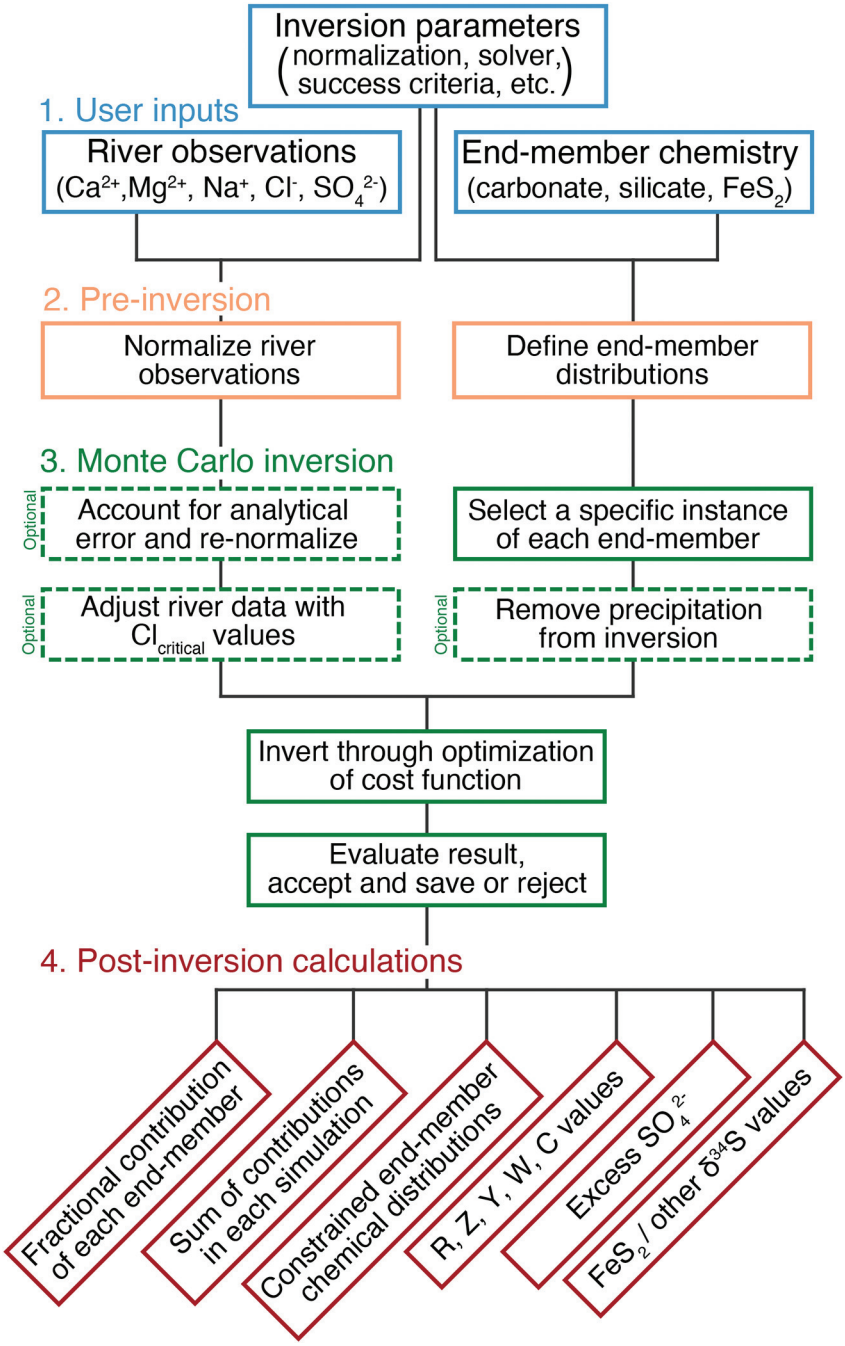

Fig. 1. Architecture of MEANDIR. Users supply observations of dissolved river chemistry, choices for how to perform the inversion, and the chemical composition of end-members (blue boxes). MEANDIR then prepares inputs (orange boxes), conducts the Monte Carlo inversion (green boxes), and calculates variables of interest (red boxes). Many of these steps are highly customizable to suit the needs of individual datasets and research questions.

Additional dissolved constituents can be added to the model or can utilize the slot of an otherwise unused variable.

The fundamental mass balance equation for river inversion models has been presented previously (Négrel and others, 1993; Gaillardet and others, 1999; Moon and others, 2014; Torres and others, 2016; Burke and others, 2018), but few detailed discussions or line-by-line calculations have been published. Existing calculations are also mostly written in code, such as the MATLAB files of Torres and others (2016) and the Python files of Hemingway and others (2020), rather than being written symbolically. Overall, methods previously used to invert observations of dissolved river chemistry are relatively opaque and difficult to modify for new applications. A major goal of our work in this article is thus to provide a flexible tool to the geochemical community for inverting observations of dissolved river chemistry, as well as to describe the choices inherent in river inversion models and clarify how the decisions during model construction impact results.

An extensive literature exists on the mathematics of numerical inversion, including published models for treating geochemical data (Pisias and others, 2013), quantification of uncertainty in source partitioning (Phillips and Gregg, 2001, 2003; Parnell and others, 2010), the selection of end-members (Dunlea and Murray, 2015), and the statistics of data with sum equal to 1 (known as a "unit-sum" constraint or, more broadly, "compositional" data; Miesch, 1976; Aitchison, 1983). However, no dedicated tool exists for customizable inversion of dissolved river chemistry and the problems that naturally arise during such calculations. Unlike MEANDIR, existing tools are not constructed to quantify the fraction of carbonate weathering relative to sulfuric acid weathering (Torres and others, 2016), or to constrain the chemical composition of secondary phases formed with isotopic fractionation. Although the mathematics underlying river inversion have been established for decades, MEANDIR is a new and useful tool because it is tailored to address the issues typically encountered by river geochemists inverting observations of dissolved chemistry. MEANDIR is freely available online, commented, and accompanied by a user guide, making the code substantially more accessible than prior inversion models. We readily acknowledge that ample opportunity remains to improve MEANDIR, such as through implementation of Markov Chain methods, programs for identification of end-members based on raw chemical observations, and refactoring to improve efficiency and readability. We hope such improvements may be implemented in future releases.

In this article we first present the mathematics of MEANDIR, beginning with the derivation of the fundamental mass balance equations. We then test the performance of MEANDIR using several previously published datasets. We apply the model to two global compilations of dissolved river chemistry (Gaillardet and others, 1999; Burke and others, 2018), river data from Iceland (Gíslason and others, 1996), river data from the Peruvian Amazon (Torres and others, 2016), and river data from the Mackenzie River basin (Horan and others, 2019). We explore the sensitivity of model results to the variable or combination of variables used for normalization (for example, dividing all solute observations by the amount of Na^+ or the sum of dissolved cations), the distribution of possible end-member chemistry, the cost function of the inversion, and whether all samples use the same end-member selections. We also demonstrate the ability of MEANDIR to quantify the loss of dissolved constituents into secondary phases such as clays, validate different approaches for calculating the $\delta^{34}S$ of river SO_4^{2-} derived from the oxidation of pyrite (FeS_2) (Torres and others, 2016; Burke and others, 2018; Hemingway and others, 2020; Kemeny and others, 2021a), and extend a formalism previously defined in Torres and others (2016) to account for oxidation of petrogenic organic carbon.

MATHEMATICS OF MEANDIR

Overview

This section is concerned with the mathematics of river mixing models utilizing Monte Carlo propagation of uncertainty. We attempt to present existing inversion methods and extend those quantitative frameworks for novel applications. Table 1 summarizes the key points of this section. After deriving the mass balance equations that underlie MEANDIR, we discuss three core components of river inversions: selection of end-members, construction of a cost function, and selection of successful simulations. We identify many additional complexities: normalizing to the sum of cations or sum of other dissolved variables (including SO_4^{2-}, ALK, and DIC), accounting for Cl^- from meteoric precipitation, quantifying the formation and chemistry of secondary phases formed with isotopic fractionation, calculating the fractions of river SO_4^{2-} sourced from oxidation of FeS_2 and DIC sourced from oxidation of petrogenic C_{org}, including HCO_3^- in the inversion, and calculating the impacts of carbonate weathering, sulfuric acid weathering, and organic carbon oxidation on atmospheric CO_2. Each of these components is discussed below and several are demonstrated in the text by applying MEANDIR to published datasets. The variables, superscripts, and subscripts used throughout this article are summarized in tables 2 and 3.

Mass Balance Equations

We first consider inversion of a single river water sample with known end-member chemistry. The number of moles (χ) of an element in a river water sample is the sum of contributions from n distinct end-members (eq 1; Négrel and others, 1993). End-members in our formalism are indexed by s between 1 and n, where s refers to a source or sink; χ is given the superscript s to refer to the s^{th} end-member and the superscript riv to indicate a river water sample. To indicate that the chosen χ is merely one dissolved variable from a set of k observations, χ is given a subscript i between 1 and k to refer to the i^{th} variable. When the i^{th} variable is a dissolved element, χ_i^{riv} indicates the number of moles of the i^{th} variable in a sample of river water and χ_i^s indicates the number of moles of the i^{th} variable derived from the s^{th} end-member (eq 1). In general, we will use rectangular brackets to indicate expressions within summations.

$$\chi_i^{riv} = \Sigma_s^n \left[\chi_i^s\right] \tag{1}$$

For isotopic variables, each contribution is weighted by the corresponding isotopic composition (eq 2). When the i^{th} variable is an isotopic observation, we represent the isotopic information of the s^{th} end-member as ${}^A R_i^s$ where R represents an isotopic ratio, i takes on the relevant element or molecule for the given isotopic system, and A represents the cardinal mass of the heavier isotope. For example, ${}^{34}R_{SO_4^{2-}}^{riv}$ refers to the ${}^{34}S/{}^{32}S$ ratio of river SO_4^{2-}, and ${}^{44}R_{Ca^{2+}}^s$ refers to the ${}^{44}Ca/{}^{40}Ca$ ratio of Ca^{2+} released by the s^{th} end-member. Note that in all equations ${}^A R_i^s$ should formally refer to the isotopic mass fraction, but here we use the isotopic ratio for simplicity.

$$\chi_i^{riv} \cdot {}^A R_i^{riv} = \Sigma_s^n \left[\chi_i^s \cdot {}^A R_i^s\right] \tag{2}$$

Solute observations are typically measurements of abundance normalized by liquid volume (μM or mg/L), while measurements of solids are typically abundance normalized by mass (ppm or wt%). The two sets of measurements are made comparable through molar ratios. One dissolved variable, or a combination of variables, will thus

TABLE 1

Summary of choices during construction of inversion models. For some categories (for example, normalization) all variables must use the same selection, while in other categories (for example, cost function) each variable has an independent selection

Topic	Parameter choice	Pros	Cons
Normalization	Na^+	Intuitive, values exist from prior studies	End-members must all contain Na^+
	$\Sigma^+(+ALK,\ DIC,\ SO_4^{2-})$	End-members not required to contain same element, model FeS_2 ox. or C_{org} ox. directly	Unintuitive, imposes unit-sum constraint on end-member ratios
End-member distribution	Normal	Generate more simulations near expected values for each end-member	Must trim distributions to avoid unphysical values (for example, Ca^{2+}/Na^+ ratios < 0)
	Uniform	Low impact on posterior distribution	Unlikely to represent natural data
Precipitation correction	Cl^- critical	Constrains precipitation contribution	Cl^- critical values often unavailable
	Precipitation as an end-member	Treats precipitation the same way as any other end-member in the inversion	Generally difficult to distinguish precipitation from evaporite or hot springs
Cost function	Absolute misfit	Can fit variables with value of 0, is useful when modeling isotopic ratios in δ notation	Hard to fit at low abundances, although partially alleviated with weighting terms
	Relative misfit	Better fit at low abundances, isotope ratios	Likely a worse fit to total charge
Culling simulation results	By sample matching	Guarantees results match observations within user-specific criteria	May be impossible to achieve desired precision for user-supplied end-members
	By fraction with lowest misfit	Ensures model results are found and minimizes total error	Model-constructed chemistry may differ from observations, sensitive to cost function
Using HCO_3^- in inversion	From titration	Independent data constrains the inversion	Should be viewed as ALK, not HCO_3^-
	From charge balance	Ensures results match river observations	Typically degenerate with other equations
Quantifying FeS_2 oxidation	SO_4^{2-} excess	Non-specific to origin of excess SO_4^{2-}	Can predict negative values of excess SO_4^{2-}
	End-member SO_4^{2-}	Constrains lithologic weathering fractions	Results subject to statistical influence
	FeS_2 ox. end-member	Constrains FeS_2 oxidation directly	Requires relatively complex normalization
Secondary phases	Negative fractional contributions	Enables estimates for chemical composition of secondary phases, with fractionation	Secondary phases must be chemically or isotopically distinct from primary phases
Calculating R, Z, C	Include Na^+, K^+	Reflects full alkalinity of weathering	Not all Na^+ and K^+ contribute to DIC loss
	Do not include Na^+, K^+	Accounts for reverse weathering when calculating DIC loss	Assumes Na^+ and K^+ in steady-state when evaluating effects of weathering on pCO_2

TABLE 2
Variables used throughout the text

Variable	Description
χ	Number of moles
${}^{A}R$	Isotopic ratio, where A is the cardinal mass of the heavy isotope
f	Fraction of river observation
A	Matrix of end-member chemistry
f	Vector of fractional contributions
b	Vector of river observations
α	Factor converting concentration to charge equivalents
Δ	Fractionation of river water and secondary phase (negative means secondary products are enriched in the lighter isotope)
$\boldsymbol{\Upsilon}$	Weighting terms in the cost function
$\boldsymbol{\omega}$	Vector of 0 and 1 controlling absolute or relative cost function
$\boldsymbol{\xi}$	Vector of 0 and 1 controlling if variable is in cost function
ϕ	Alkalinity released through carbonate weathering
β	Alkalinity released through silicate weathering
γ	Alkalinity consumed through FeS_2 oxidation
θ	Dissolved inorganic carbon released through C_{org} oxidation
R	Carbonate weathering fraction
Z	Sulfuric acid weathering fraction
Y	Fraction of river SO_4^{2-} from FeS_2 oxidation
W	SO_4^{2-} from FeS_2 oxidation relative to normalization variable
C	Organic weathering fraction

serve as a "normalization variable" in order to generate a set of molar ratios from measurements of dissolved concentrations or the relative mass abundances in solid end-members. We indicate the normalization variable with the subscript norm. Although commonly $\chi_{norm} = \chi_{Na^+}$ (Négrel and others, 1993), alternative choices are possible and discussed extensively later in this article.

The contribution of the s^{th} end-member to χ_i^{riv} (eq 3) or to $\chi_i^{riv}.{}^{A}R_i^{riv}$ (eq 4) is found by scaling χ_{norm}^{s} by the ratio χ_i^s/χ_{norm}^s or the ratio $(\chi_i^s.{}^{A}R_i^s)/\chi_{norm}^s$. In turn, we can define f_i^s as the fractional contribution of the s^{th} end-member to the i^{th} variable either for elemental (eq 5) or isotopic information (eq 6). The ratios $\chi_i^{riv}/\chi_{norm}^{riv}$ or $\left(\chi_i^{riv}.{}^{A}R_i^{riv}\right)/\chi_{norm}^{riv}$ can then be expressed as the sums of fractional contributions from each of n end-members to χ_{norm}^{riv} multiplied by the corresponding χ_i^s/χ_{norm}^s (eq 7) or $\left(\chi_i^s.{}^{A}R_i^s\right)/\chi_{norm}^s$ (eq 8) of each end-member.

$$\chi_i^{riv} = \Sigma_s^n\left[\chi_{norm}^s\left(\frac{\chi_i^s}{\chi_{norm}^s}\right)\right] \tag{3}$$

$$\chi_i^{riv}.{}^{A}R_i^{riv} = \Sigma_s^n\left[\chi_{norm}^s\left(\frac{\chi_i^s.{}^{A}R_i^s}{\chi_{norm}^s}\right)\right] \tag{4}$$

TABLE 3

Subscripts and superscripts on variables used throughout the text

Subscripts	Description
i	Generic dissolved observation, ranges from 1 to k
i_1, i_2, i_3	Example of three dissolved observations
i_{norm}	A single variable contributing to normalization, ranges from 1 to k_{norm}
i_{RZC}	A single variable in the denominator of R, Z, C, ranges from 1 to k_{RZC}
$i_{RZC} \ldots k_{RZC}$	List of variables in denominator of R, Z, C. For example, Ca^{2+}, Mg^{2+}, Na^+
norm	Normalization, either an individual variable or sum of variables
Σ^+	Charge-equivalent sum of cations, typically Ca^{2+}, Mg^{2+}, Na^+, and K^+
Cl^- critical	Cl^- attributable to precipitation
excess SO_4^{2-}	SO_4^{2-} in excess of mixing (calculated without SO_4^{2-} in inversion)
FeS_2 SO_4^{2-}	SO_4^{2-} from end-members representing FeS_2 oxidation
sc (left-hand)	Scaled values after normalizing by the sum of all fractional contributions
Superscripts	**Description**
riv	Sample of river water
s	Generic inversion end-member (a source or sink), ranges from 1 to n
s_1, s_2, s_3	Example of three end-members
s′	Generic inversion end-member (a source or sink), ranges from 1 to n, used when equations require independent summations over end-members
s^{second}	End-member representing a secondary phase, such as clay
s_i^{source}	End-member sources of the variable i, ranges from 1 to n_i^{source}
$s_{FeS_2\ SO_4^{2-}}$	End-member source of FeS_2-derived SO_4^{2-}, ranges 1 to $n_{FeS_2\ SO_4^{2-}}$
$s_{SO_4^{2-}}$	End-member source of non-FeS_2-derived SO_4^{2-}, ranges 1 to $n_{SO_4^{2-}}$
s_{carb}	Carbonate end-member, ranges from 1 to n_{carb}
s_{weath}	Weathering end-member, ranges from 1 to n_{weath}
$s_{i_{RZC}}^{source}$	End-member sources of the variable i_{RZC}, ranges from 1 to $n_{i_{RZC}}^{source}$
$s_{i_{RZC}}^{sink}$	End-member sinks of the variable i_{RZC}, ranges from 1 to $n_{i_{RZC}}^{sink}$
source	Gross input from primary end-members (not including secondary phases)
other	The 'other' end-member, which sources SO_4^{2-} to river water
FeS_2 ox. ALK	On Z, Y, W, means numerator from FeS_2 end-member, ALK
FeS_2 ox. SO_4^{2-}	On Z, Y, W, means numerator from FeS_2 end-member, SO_4^{2-}
excess SO_4^{2-}	On Z, Y, W, means numerator from river excess SO_4^{2-}
FeS_2 SO_4^{2-}	On Z, Y, W, means numerator from end-members weathered with H_2SO_4
g (left-hand)	Gross (not accounting for formation of secondary phases)
n (left-hand)	Net (accounting for formation of secondary phases)

$$f_i^s = \frac{\chi_i^s}{\chi_i^{riv}} \tag{5}$$

$$f_i^s = \frac{\chi_i^s \cdot {}^A R_i^s}{\chi_i^{riv} \cdot {}^A R_i^{riv}} \tag{6}$$

$$\frac{\chi_i^{riv}}{\chi_{norm}^{riv}} = \frac{\Sigma_s^n \left[\chi_{norm}^s \left(\frac{\chi_i^s}{\chi_{norm}^s} \right) \right]}{\chi_{norm}^{riv}} = \Sigma_s^n \left[\left(\frac{\chi_{norm}^s}{\chi_{norm}^{riv}} \right) \left(\frac{\chi_i^s}{\chi_{norm}^s} \right) \right] = \Sigma_s^n \left[f_{norm}^s \left(\frac{\chi_i^s}{\chi_{norm}^s} \right) \right] \tag{7}$$

$$\left(\frac{\chi_i^{riv}.{}^A R_i^{riv}}{\chi_{norm}^{riv}}\right) = \Sigma_s^n\left[\left(\frac{\chi_{norm}^s}{\chi_{norm}^{riv}}\right)\left(\frac{\chi_i^s.{}^A R_i^s}{\chi_{norm}^s}\right)\right]$$
$$= \Sigma_s^n\left[f_{norm}^s\left(\frac{\chi_i^s.{}^A R_i^s}{\chi_{norm}^s}\right)\right] \quad (8)$$

A single sample defines k linear equations that can be written in matrix form as $\mathbf{b} = \mathbf{A} \cdot \mathbf{f}$. The i^{th} position of the observation vector $\mathbf{b}$ (size k x 1) is either a normalized elemental concentration or the normalized product of an element and its isotopic ratio (eq 9). Matrix $\mathbf{A}$ (size k x n) is defined to contain the end-member elemental or isotopic compositions, using the same χ_{norm} as used in $\mathbf{b}$ (eq 10). The solution vector $\mathbf{f}$ (size n x 1) contains the fractional contributions from each end-member to the normalization variable (the f_{norm}^s values) for the sample described in $\mathbf{b}$ with end-member matrix $\mathbf{A}$ (eq 11).

$$\mathbf{b}(i) = \left(\frac{\chi_i^{riv}}{\chi_{norm}^{riv}}\right) \text{or } \mathbf{b}(i) = \left(\frac{\chi_i^{riv}.{}^A R_i^{riv}}{\chi_{norm}^{riv}}\right) \quad (9)$$

$$\mathbf{A}(i,s) = \left(\frac{\chi_i^s}{\chi_{norm}^s}\right) \text{ or } \mathbf{A}(i,s) = \left(\frac{\chi_i^s.{}^A R_i^s}{\chi_{norm}^s}\right) \quad (10)$$

$$\mathbf{f}(s) = f_{norm}^s \quad (11)$$

Generic (eq 12) and specific (eq 13) examples of the equation $\mathbf{b} = \mathbf{A} \cdot \mathbf{f}$ are given below for three dissolved concentrations and one isotope ratio (indexed by i_1, i_2, i_3, with the isotopic ratio on the i_3 variable, or Na^+, Cl^-, Ca^{2+}, and $^{44}Ca/^{40}Ca$) and three end-members (indexed by s_1, s_2, and s_3, or carbonate (carb), silicate (slct), and precipitation (prec)) where $\chi_{norm} = \chi_{Na^+}$. Note that, because one of the dissolved variables is equal to the normalization variable, the corresponding equation simplifies to $1 = \Sigma_s^n\left[f_{Na^+}^s\right] = \Sigma_s^n[f_{norm}^s]$ (first row of eq 13). We stress that this equation results from our starting point of fundamental mass balance and is not taken axiomatically; not all choices of χ_{norm} lead directly to an equation comparable to $1 = \Sigma_s^n[f_{norm}^s]$. For example, when normalization is to the sum of dissolved variables instead of a single dissolved variable, an equation of this type does not appear without summing multiple normalized mass balance equations.

$$\begin{bmatrix} \left(\frac{\chi_{i_1}^{riv}}{\chi_{norm}^{riv}}\right) \\ \left(\frac{\chi_{i_2}^{riv}}{\chi_{norm}^{riv}}\right) \\ \left(\frac{\chi_{i_3}^{riv}}{\chi_{norm}^{riv}}\right) \\ \left(\frac{\chi_{i_3}^{riv}.{}^A R_{i_3}^{riv}}{\chi_{norm}^{riv}}\right) \end{bmatrix} = \begin{bmatrix} \left(\frac{\chi_{i_1}^{s_1}}{\chi_{norm}^{s_1}}\right) & \left(\frac{\chi_{i_1}^{s_2}}{\chi_{norm}^{s_2}}\right) & \left(\frac{\chi_{i_1}^{s_3}}{\chi_{norm}^{s_3}}\right) \\ \left(\frac{\chi_{i_2}^{s_1}}{\chi_{norm}^{s_1}}\right) & \left(\frac{\chi_{i_2}^{s_2}}{\chi_{norm}^{s_2}}\right) & \left(\frac{\chi_{i_2}^{s_3}}{\chi_{norm}^{s_3}}\right) \\ \left(\frac{\chi_{i_3}^{s_1}}{\chi_{norm}^{s_1}}\right) & \left(\frac{\chi_{i_3}^{s_2}}{\chi_{norm}^{s_2}}\right) & \left(\frac{\chi_{i_3}^{s_3}}{\chi_{norm}^{s_3}}\right) \\ \left(\frac{\chi_{i_3}^{s_1}.{}^A R_{i_3}^{s_1}}{\chi_{norm}^{s_1}}\right) & \left(\frac{\chi_{i_3}^{s_2}.{}^A R_{i_3}^{s_2}}{\chi_{norm}^{s_2}}\right) & \left(\frac{\chi_{i_3}^{s_3}.{}^A R_{i_3}^{s_3}}{\chi_{norm}^{s_3}}\right) \end{bmatrix} \begin{bmatrix} f_{norm}^{s_1} \\ f_{norm}^{s_2} \\ f_{norm}^{s_3} \end{bmatrix} \quad (12)$$

$$\begin{bmatrix} \left(\frac{\chi^{riv}_{Na^+}}{\chi^{riv}_{Na^+}}\right) = 1 \\ \left(\frac{\chi^{riv}_{Cl^-}}{\chi^{riv}_{Na^+}}\right) \\ \left(\frac{\chi^{riv}_{Ca^{2+}}}{\chi^{riv}_{Na^+}}\right) \\ \left(\frac{\chi^{riv}_{Ca^{2+}} \cdot {}^{44}R^{riv}_{Ca^{2+}}}{\chi^{riv}_{Na^+}}\right) \end{bmatrix} = \begin{bmatrix} \left(\frac{\chi^{carb}_{Na^+}}{\chi^{carb}_{Na^+}}\right) = 1 & \left(\frac{\chi^{slct}_{Na^+}}{\chi^{slct}_{Na^+}}\right) = 1 & \left(\frac{\chi^{prec}_{Na^+}}{\chi^{prec}_{Na^+}}\right) = 1 \\ \left(\frac{\chi^{carb}_{Cl^-}}{\chi^{carb}_{Na^+}}\right) & \left(\frac{\chi^{slct}_{Cl^-}}{\chi^{slct}_{Na^+}}\right) & \left(\frac{\chi^{prec}_{Cl^-}}{\chi^{prec}_{Na^+}}\right) \\ \left(\frac{\chi^{carb}_{Ca^{2+}}}{\chi^{carb}_{Na^+}}\right) & \left(\frac{\chi^{slct}_{Ca^{2+}}}{\chi^{slct}_{Na^+}}\right) & \left(\frac{\chi^{prec}_{Ca^{2+}}}{\chi^{prec}_{Na^+}}\right) \\ \left(\frac{\chi^{carb}_{Ca^{2+}} \cdot {}^{44}R^{carb}_{Ca^{2+}}}{\chi^{carb}_{Na^+}}\right) & \left(\frac{\chi^{slct}_{Ca^{2+}} \cdot {}^{44}R^{slct}_{Ca^{2+}}}{\chi^{slct}_{Na^+}}\right) & \left(\frac{\chi^{prec}_{Ca^{2+}} \cdot {}^{44}R^{prec}_{Ca^{2+}}}{\chi^{prec}_{Na^+}}\right) \end{bmatrix} \begin{bmatrix} f^{carb}_{Na^+} \\ f^{slct}_{Na^+} \\ f^{prec}_{Na^+} \end{bmatrix} \tag{13}$$

The system of equations defined by $\mathbf{b} = \mathbf{A} \cdot \mathbf{f}$ is solved by optimizing a cost function to minimize the misfit of inversion results from observations. In turn, the inversion-constrained f^s_{norm} values are scaled to reach end-member contributions to the other variables. For elemental observations these values are reached through multiplication with χ^s_i/χ^s_{norm} and division by $\chi^{riv}_i/\chi^{riv}_{norm}$ (eq 14). In the case of isotopes, values are reached through multiplication with $(\chi^s_i \cdot {}^A R^s_i)/\chi^s_{norm}$ and division by $(\chi^{riv}_i \cdot {}^A R^{riv}_i)/\chi^{riv}_{norm}$ (eq 15).

$$f^s_i = \frac{\chi^s_i}{\chi^{riv}_i} = \left(\frac{\chi^s_i}{\chi^{riv}_i}\right)\left(\frac{f^s_{norm} \cdot \chi^{riv}_{norm}}{\chi^s_{norm}}\right) = f^s_{norm} \frac{\left(\frac{\chi^s_i}{\chi^s_{norm}}\right)}{\left(\frac{\chi^{riv}_i}{\chi^{riv}_{norm}}\right)} \tag{14}$$

$$f^s_i = \frac{\chi^s_i \cdot {}^A R^s_i}{\chi^{riv}_i \cdot {}^A R^{riv}_i} = \left(\frac{\chi^s_i \cdot {}^A R^s_i}{\chi^{riv}_i \cdot {}^A R^{riv}_i}\right) \cdot \left(\frac{f^s_{norm} \cdot \chi^{riv}_{norm}}{\chi^s_{norm}}\right) = f^s_{norm} \frac{\left(\frac{\chi^s_i \cdot {}^A R^s_i}{\chi^s_{norm}}\right)}{\left(\frac{\chi^{riv}_i \cdot {}^A R^{riv}_i}{\chi^{riv}_{norm}}\right)} \tag{15}$$

Monte Carlo Propagation of Uncertainty

The preceding discussion focused on a single instance of inverting a single river water sample with known values of end-member χ^s_i/χ^s_{norm} and ${}^A R^s_i$. However, due to the lithological heterogeneity of most river catchments, it is common to employ a Monte Carlo approach to account for the uncertainty in end-member chemical composition. Although in principle one could address uncertainty propagation analytically, and indeed quantifying the uncertainty associated with mixing is analytically tractable in certain cases (Genereux, 1998; He and others, 2020), a Monte Carlo approach generally provides much more flexibility. The Monte Carlo formulation implemented in MEANDIR allows end-members to have different types of chemical distributions while also being subject to solution constraints. The uncertainty due to both of these conditions may be very difficult or impossible to solve analytically.

Application of a Monte Carlo technique entails repeatedly re-defining the entries of the end-member chemical matrix **A** and repeatedly inverting the mass balance equations for each sample. Prior river inversion models have commonly defined the entries of **A** as having either uniform or normal distributions of possible values. On each inversion instance, a value from each distribution is selected for use in the calculation. MEANDIR currently performs this repeated re-definition of **A** without knowledge of prior results, but implementation of more complex methods for selecting end-member chemistry could be implemented in future releases. MEANDIR can also repeatedly re-define entries of **b**, allowing the model to account for analytical error associated with measurements of dissolved chemistry.

The output of Monte Carlo river mixing models is two sets of distributions for each sample: one set consists of separate distributions of the fraction of each dissolved variable from each end-member (f_i^s values), and the second set consists of separate distributions of the normalized elemental (χ_i^s/χ_{norm}^s) or isotopic ($^A R_i^s$) ratios of each end-member. The nature of these two sets of distributions depends on user choices regarding the selection of successful results. For example, when each river water sample uses the same selections from end-member distributions, the distributions describing inversion-constrained end-member chemistry converge. The fundamental problem of river inversion is how to generate these two sets of distributions for each sample using measurements of dissolved chemistry, the analytical error of those measurements, and an initial set of end-member distributions. Once determined, analysis of the inversion-constrained distributions of fractional contributions and end-member chemistry can provide information on chemical weathering upstream of the river water sampling site.

The application of Monte Carlo techniques to river mixing produces many sets of results. Throughout this article we will use "simulation" to refer to the set of results arising from an individual instance of calculating fractional contributions from river observations (one single solution to the equation $\mathbf{b} = \mathbf{A} \cdot \mathbf{f}$) and "scenario" to distinguish among inversions conducted on different river data, end-members, or model parameters.

Selection of End-members

MEANDIR requires a user-defined number of end-members with defined chemical distributions, although exceptions to the latter condition arise when end-member ratios are set relative to sample chemistry or through fractionation factors. Previously, selection of the number of end-members has relied mostly on lithologic context. Prior work has often included a carbonate lithology and a silicate lithology, where the chemistry of the latter is informed by fluorescence measurements or acid digestions of local bedrock and/or suspended sediment. Additionally, most studies have included an end-member with non-zero $\chi_{Cl^-}^s/\chi_{norm}^s$, typically called either precipitation or evaporite.

An alternative approach for quantifying the number of end-members is Principal Component Analysis (PCA), which is a statistical technique that identifies combinations of variables that minimize variance. Following PCA, a scree test can help inform the user of the number of significant components, which approximates the number of unique sources of variance. Identification of the number of significant components can thus help to identify the number of end-members contributing to the observed river chemistry (Christophersen and Hooper, 1992; Négrel and others, 1993). Importantly, however, when performing PCA on ratios or data subject to a unit-sum constraint, the effects of auto-correlation and closure may require data transformations prior to analysis (Aitchison, 1983).

It is possible to uniquely deconvolve k variables among contributions from n linearly independent end-members when $k = n$. However, this condition does not constrain end-member contributions to be positive and negative contributions are typically unphysical, although exceptions arise when modeling the formation of secondary phases. In an overdetermined system where $k>n$, the system of equations has excess information for constraining fractional contributions to measured dissolved chemistry. In this case exact agreement between end-members and observations is unlikely due to both analytical error and the chemical heterogeneity of bedrock. Conversely, in an under-constrained system where $k < n$, multiple combinations of end-member contributions may explain observations equally well. The number of

independent end-members should generally not greatly exceed the number of observations, but can be less than or equal to the number of observations.

In addition to defining the number of end-members, users must also define the allowable ranges in end-member chemical composition. The spread associated with the composition of an end-member, which is used in the Monte Carlo analysis, is typically described as either uniform or normal. In either case, concern is warranted regarding how the structure of the initial distribution may influence the distribution of end-member chemistry in successful simulations. When end-member uncertainty is described with a uniform distribution over a positive domain, no negative end-member ratios are possible and MEANDIR selects end-member ratios from the user-defined distributions. Conversely, when the chemical range of an end-member is described as a normal distribution, a subset of the possible values are likely to be negative. For example, if selecting values from the normal distribution $\mu \pm \mu$, approximately 16% of selections will be negative. If independently selecting multiple ratios for multiple end-members, many sets of values are likely to contain at least 1 negative term. A similar challenge occurs when selecting end-member ratios subject to a unit-sum constraint, such as when normalizing to the sum of cations; in this case, values greater than 1 are a common, but unphysical, outcome of selecting values from normal distributions. To address these problems, when the user defines end-member uncertainty to be distributed normally, MEANDIR selects end-member chemical ratios from truncated normal distributions. When the normalization is to a dissolved concentration such as χ_{Na^+}, distributions are bound on the lower side at 0. When normalization is to the sum of dissolved variables, ratios with a variable in the numerator constituent to the denominator are bounded between 0 and 1. Notably, the lower truncation is not applied when end-members ratio are allowed to be negative, which can occur when modeling FeS_2 oxidation. Furthermore, an additional constraint from charge balance occurs when all major cations and anions are included in the inversion. In most cases an inversion including $\chi^{riv}_{Ca^{2+}}$, $\chi^{riv}_{Mg^{2+}}$, $\chi^{riv}_{Na^+}$, $\chi^{riv}_{K^+}$, $\chi^{riv}_{SO_4^{2-}}$, $\chi^{riv}_{Cl^-}$, and $\chi^{riv}_{HCO_3^-}$ will represent most of the positive and negative charge in solution. In this case, the sum of an end-member's normalized cation ratios should equal the sum of its normalized anion ratios.

An additional question is whether separate river samples should use the exact same set of end-member values or if samples should be treated independently. For river waters from the same location, such as a time series, it may be appropriate to evaluate all samples using the same set of end-member compositions. However, if there are large seasonal changes in the source of river water, it can be more appropriate to evaluate each sample independently. MEANDIR can run simulations where all samples use independently drawn end-member chemical ratios or where all samples use the same set of end-member ratios.

Cost Functions

The equation $\mathbf{b} = \mathbf{A} \cdot \mathbf{f}$ (eqs 9, 10, and 11) is solved through optimization of a cost function, indicated as $c(\mathbf{f})$. That is, MEANDIR solves for the vector $\mathbf{f}$ that minimizes a function $c(\mathbf{f})$ given the current end-member matrix $\mathbf{A}$ and observations vector $\mathbf{b}$. Least-squares optimization in MATLAB can be called using the command mldivide, and the command lsqnonneg returns a non-negative least-squares solution. Both of these programs optimize a cost function for absolute misfit between observations and inversion results (eq 16; where subscripts on b, A, and f indicate positions within the relevant vectors or matrix), while lsqnonneg also constrains fractional contributions to be positive. The functions mldivide and lsqnonneg are both available for use in MEANDIR. However, MEANDIR can also solve the equation $\mathbf{b} = \mathbf{A} \cdot \mathbf{f}$ through optimization of custom cost functions. An important custom function, further discussed

below, is one that evaluates the proportional misfit between observations and reconstructed river chemistry (eq 17).

$$c(\mathbf{f}) = \sqrt{\Sigma_i^k \left[\Upsilon_i \left(\Sigma_s^n [A_{i,s} f_s] - b_i \right)^2 \right]} \tag{16}$$

$$c(\mathbf{f}) = \sqrt{\Sigma_i^k \left[\Upsilon_i \left(\frac{\Sigma_s^n [A_{i,s} f_s] - b_i}{b_i} \right)^2 \right]} \tag{17}$$

The results of river inversion reflect the choice of cost function. For example, if a water sample has $\chi^{riv}_{Ca^{2+}}/\chi^{riv}_{Na^+} = 10$ and $\chi^{riv}_{K^+}/\chi^{riv}_{Na^+} = 1$, an absolute cost function would assign the same cost to a simulation generating $\chi^{riv}_{Ca^{2+}}/\chi^{riv}_{Na^+} = 11$ and $\chi^{riv}_{K^+}/\chi^{riv}_{Na^+} = 1$ as a simulation generating $\chi^{riv}_{Ca^{2+}}/\chi^{riv}_{Na^+} = 10$ and $\chi^{riv}_{K^+}/\chi^{riv}_{Na^+} = 2$. In both cases one ratio contributes a misfit of 0 and the other contributes a misfit of 1, and these two scenarios would result in the same evaluation of an absolute cost function (eq 16). However, the two scenarios are different in proportional cost (eq 17), where the difference between model results and observations are compared to the observations. The first simulation generates a 10% proportional misfit for $\chi^{riv}_{Ca^{2+}}/\chi^{riv}_{Na^+}$ and no misfit for $\chi^{riv}_{K^+}/\chi^{riv}_{Na^+}$, while the latter generates no misfit for $\chi^{riv}_{Ca^{2+}}/\chi^{riv}_{Na^+}$ and a 100% proportional misfit for $\chi^{riv}_{K^+}/\chi^{riv}_{Na^+}$.

The results of the proportional cost function could be reached using the absolute cost function by including weighting terms, indicated as values contained within the vector Υ (size k x 1) (eqs 16 and 17). Continuing the above example, the results of the relative cost function could be attained using the absolute cost function by including a weighting term of 10 on the ratio of $\chi^{riv}_{K^+}/\chi^{riv}_{Na^+}$ and a weighting term of 1 on $\chi^{riv}_{Ca^{2+}}/\chi^{riv}_{Na^+}$. In other words, the difference between the absolute and relative cost functions can be partially negated through the use of appropriate weights.

Isotopic ratios introduce an important complication to these considerations. For data reported in δ notation, where 0‰ means having an isotopic ratio equal to international reference materials, proportional misfit is less meaningful than absolute misfit. That is, a difference of 1‰ in δ units between observations and model results should incur the same cost if that difference occurs when the observed value is 0‰ or 20‰. We note that this expectation assumes linearity in δ values, which is generally appropriate at Earth's surface conditions for isotopic systems heavier than hydrogen. Where the 0‰ observation would have infinite proportional misfit as evaluated with a relative cost function (eq 17), fractional misfit for the 20‰ case would be merely 5%.

We identify two main approaches for addressing the reference frame problem associated with δ notation. The first approach, which we do not recommend, is to use an absolute cost function for the isotopic data in δ notation while using a proportional cost function for variables describing normalized elemental abundances. The second mechanism, which we do recommend, is to convert δ notation to isotopic ratios prior to inversion in order to remove the reference frame that defines 0‰. When considering isotopic ratios, rather than δ notation, proportional differences between observations and inversion results become meaningful. Because isotopic data are often reported in δ notation, MEANDIR is able to convert user-supplied δ values to isotopic ratios for inversion with a proportional cost function (eq 17) and then convert the results back to δ notation for ease of analysis. MEANDIR comes equipped with defined values for the isotopic ratios of common reference materials in order to perform the conversion from δ notation to isotopic ratios (Moore and Machlan, 1972;

Baertschi, 1976; Chang and Li, 1990; Taylor and others, 1992; Qi and others, 1997; Ding and others, 2001; Valkiers and others, 2005; Bizzarro and others, 2011; Brand and others, 2014; Mayer and Wiser, 2014; Daëron and others, 2016), but users can easily modify these values to reflect the specific reference materials underlying their isotopic measurements.

In summary, MEANDIR allows users to specify whether the cost function should be the built-in functions mldivide or lsqnonneg or should be a user-defined function with weighting terms. In general, we recommend that inversions use a proportional cost function for chemical observations to ensure that variables at low relative abundance are faithfully reconstructed. When inverting isotopic information, we likewise recommend using a proportional cost function for isotopic ratios but, if required, an absolute cost function for data in δ notation. To balance these competing demands the default optimization in MEANDIR is to minimize a mixed cost function that combines absolute and proportional misfit (eq 18), but where each dissolved variable only contributes to one of the two terms (indicated through the vector **ω**, which only contains values of 1 or 0).

$$c(\mathbf{f}) = \sqrt{\Sigma_i^k \left[(\xi_i \Upsilon_i) \left(\omega_i \left(\Sigma_s^n [A_{i,s} f_s] - b_i \right)^2 + (1 - \omega_i) \left(\frac{\Sigma_s^n [A_{i,s} f_s] - b_i}{b_i} \right)^2 \right) \right]} \tag{18}$$

Initial values for the optimization can be set equal to the output of the built-in absolute cost functions or set uniformly equal to 1 divided by the number of end-members. Moreover, MEANDIR allows for only a subset of dissolved variables to be included in the cost function evaluation. This serves the purpose of allowing degenerate variables, such as $\chi^{riv}_{HCO_3^-}$ when calculated through charge balance, to be included in the inversion without impacting evaluation of the cost function. To allow observations to be excluded from the cost function, the vector **ξ** contains values of only 0 or 1 (eq 18). Lastly, the use of custom cost functions also allows users to supply custom optimization criteria. For example, MEANDIR could bound end-member fractional contributions between arbitrary ranges or constrain the contributions of certain end-members to be negative.

Selection of Successful Simulations

Misfit between inversion results and river observations occurs when the chemical composition of end-members is unable to generate sample observations. As discussed above, when dissolved chemistry is normalized to χ_{Na^+} the mass balance equation for $\chi^{riv}_{Na^+}$ simplifies to $1 = \Sigma_s^n \left[f^s_{Na^+} \right]$ (eq 13). However, in inversions that are over-constrained or with inappropriate end-members, in many results $1 \neq \Sigma_s^n \left[f^s_{Na^+} \right]$; rather, $\Sigma_s^n \left[f^s_{Na^+} \right]$ will equal a value that, in conjunction with the other equations being inverted, optimizes the relevant cost function (eq 18). This example demonstrates that, even though the equations given to the inversion are derived from mass balance, simulations may return results that are offset from observations. The user is thus left with either a set of results that require sub-sampling prior to analysis or the implementation of a quality test during each simulation.

A first solution to the problem of low-quality fits is to accept a fraction of all simulations with the lowest misfit between results and observations (Torres and others, 2016). However, this approach does not guarantee that the isolated subset of simulations is a reasonable match to observations. The additional question arises of whether simulations should be culled at the level of each individual river sample or across the entire sample suite. MEANDIR is able to run calculations of this type, in which only a

small fraction of simulations with lowest misfit from observations are retained. Based on user selection, MEANDIR can isolate this best fitting fraction at the level of either an individual sample or the entire sample set.

A second solution to the problem of low-quality fits is to accept simulations based on the magnitude of misfit from observations, rather than on misfit relative to other results. One important approach to this problem is to only accept simulations that meet a criterion in which all variables are modeled within a desired precision. We call this approach "sample matching" because the condition for a simulation to count as successful is whether the result recreates sample observations. Analytical error during quantification of major ion concentrations is typically about 5%, so forcing model results to match observations of dissolved concentrations within about 15% (3σ) would include ~99% of likely values. Notably, if the inversion model already accounts for analytical error when defining the vector $\mathbf{b}$ of river observations, allowing for misfit between model results and observations may still be required. The sample matching approach ensures that only simulations with acceptable misfit between inversion results and observations are kept while allowing simulations with high misfit to be removed efficiently during the calculation.

The 15% sample matching criteria described above is equivalent to the condition that, for a non-isotopic variable, $0.85 \leq \Sigma_s^n[f_i^s] \leq 1.15$. However, for isotopic information the individual f_i^s values reference the ratio of the product of concentration and isotopic ratio (eq 6), so bounding the sum of such terms between 85% and 115% does not guarantee robust consistency between inversion results and isotopic observations. Rather, MEANDIR accomplishes sample matching for isotopic data by evaluating whether the absolute difference between sample observations and model-reconstructed isotope value is within user-defined limits. This condition can be expressed as whether $\mathrm{diff}_i^{low} \leq {}^{A}R_i^{riv} - \Sigma_s^n[f_i^s \cdot {}^{A}R_i^s]/\Sigma_s^n[f_i^s] \leq \mathrm{diff}_i^{high}$ given user-supplied values of diff_i^{low} and diff_i^{high} as permissible differences. For example, if an inversion included data on both $\chi^{riv}_{SO_4^{2-}}$ and ${}^{34}R^{riv}_{SO_4^{2-}}$, users could specify to only accept simulation results that recreate between 85% and 115% of $\chi^{riv}_{SO_4^{2-}}$ and recreate within ±1‰ of the $\delta^{34}S$ value corresponding to ${}^{34}R^{riv}_{SO_4^{2-}}$.

Defining the Fraction of $\chi^{riv}_{Cl^-}$ from Precipitation ($\chi^{riv}_{Cl^-\ critical}$ Values)

Quantifying the sources of $\chi^{riv}_{Cl^-}$ is important for separating the components of river chemistry that derive from chemical weathering from those derived from cyclic salts. $\chi^{riv}_{Cl^-}$ is often attributed to either precipitation or evaporite dissolution (Galy and France-Lanord, 1999), with a subset of studies also accounting for inputs from hot springs (Tipper and others, 2006) and anthropogenic pollution (Burke and others, 2018). When inverting data with multiple possible sources for $\chi^{riv}_{Cl^-}$, one approach is to first define how much $\chi^{riv}_{Cl^-}$ can be attributed to precipitation, often called "Cl^-critical" and here indicated as $\chi^{riv}_{Cl^-\ critical}$. These values can be derived from the Cl^- concentration of precipitation scaled by a factor reflecting the ratio of precipitation to discharge within a river basin (Gaillardet and others, 1999). When $\chi^{riv}_{Cl^-\ critical} \geq \chi^{riv}_{Cl^-}$, precipitation provides 100% of $\chi^{riv}_{Cl^-}$ (eq 19, where the subscript "prec" indicates the end-member representing meteoric precipitation). In turn, other end-members with non-zero normalized $\chi^{s}_{Cl^-}$ ratios must then have zero fractional contribution to the normalization variable. When $\chi^{riv}_{Cl^-\ critical} < \chi^{riv}_{Cl^-}$, precipitation does not fully account for $\chi^{riv}_{Cl^-}$ and additional Cl^--bearing end-members make contributions to dissolved chemistry (eq 20). Note that equation (19) and equation (20) are specific instances of equation (14).

$$\chi^{\text{riv}}_{\text{Cl}^-\ \text{critical}} \geq \chi^{\text{riv}}_{\text{Cl}^-}:\ \text{f}^{\text{prec}}_{\text{Cl}^-} = 1,\ \text{f}^{\text{prec}}_{\text{i}} = \frac{\left(\frac{\chi^{\text{prec}}_{\text{i}}}{\chi^{\text{prec}}_{\text{Cl}^-}}\right)}{\left(\frac{\chi^{\text{riv}}_{\text{i}}}{\chi^{\text{riv}}_{\text{Cl}^-}}\right)} \tag{19}$$

$$\chi^{\text{riv}}_{\text{Cl}^-\ \text{critical}} < \chi^{\text{riv}}_{\text{Cl}^-}:\ \text{f}^{\text{prec}}_{\text{Cl}^-} = \frac{\chi^{\text{riv}}_{\text{Cl}^-\ \text{critical}}}{\chi^{\text{riv}}_{\text{Cl}^-}},\ \text{f}^{\text{prec}}_{\text{i}} = \text{f}^{\text{prec}}_{\text{Cl}^-} \frac{\left(\frac{\chi^{\text{prec}}_{\text{i}}}{\chi^{\text{prec}}_{\text{Cl}^-}}\right)}{\left(\frac{\chi^{\text{riv}}_{\text{i}}}{\chi^{\text{riv}}_{\text{Cl}^-}}\right)} \tag{20}$$

Precipitation also sources dissolved variables other than Cl^-, and the chemistry of the river water sample must be manually adjusted to reflect these additional inputs when correcting $\chi^{\text{riv}}_{\text{Cl}^-}$ with $\chi^{\text{riv}}_{\text{Cl}^-\ \text{critical}}$ values. Mathematically, the vector **b** must be updated (eqs 21 and 22), the matrix **A** should no longer have a column for precipitation, and the vector **f** should no longer have a row for precipitation.

$$\mathbf{b}(\text{i}) = \left(\frac{\chi^{\text{riv}}_{\text{i}}}{\chi^{\text{riv}}_{\text{norm}}}\right) - \text{f}^{\text{prec}}_{\text{norm}} \left(\frac{\chi^{\text{prec}}_{\text{i}}}{\chi^{\text{prec}}_{\text{norm}}}\right) \tag{21}$$

$$\mathbf{b}(\text{i}) = \left(\frac{\chi^{\text{riv}}_{\text{i}} \cdot {}^{A}\text{R}^{\text{riv}}_{\text{i}}}{\chi^{\text{riv}}_{\text{norm}}}\right) - \text{f}^{\text{prec}}_{\text{norm}} \left(\frac{\chi^{\text{prec}}_{\text{i}} \cdot {}^{A}\text{R}^{\text{prec}}_{\text{i}}}{\chi^{\text{prec}}_{\text{norm}}}\right) \tag{22}$$

The application of $\chi^{\text{riv}}_{\text{Cl}^-\ \text{critical}}$ values becomes difficult when $\chi^{\text{riv}}_{\text{Cl}^-}$ and $\chi^{\text{riv}}_{\text{Cl}^-\ \text{critical}}$ are sufficiently large relative to other dissolved variables that removal of $\chi^{\text{riv}}_{\text{Cl}^-\ \text{critical}}$ from the water sample causes element ratios to become negative (eq 21). A first solution to this problem is to remove from the river sample as much $\chi^{\text{riv}}_{\text{Cl}^-}$ as possible without causing other ratios to attain negative values. However, if the limiting variable is an observation such as $\chi^{\text{riv}}_{\text{Ca}^{2+}}$, most of the remaining end-members are likely to source this constituent and it becomes difficult to find a solution that faithfully reconstructs dissolved chemistry. Moreover, if precipitation is the only source of $\chi^{\text{riv}}_{\text{Cl}^-}$, removal of only a fraction of $\chi^{\text{riv}}_{\text{Cl}^-}$ will not satisfy sample matching requirements. Instead, the solution implemented in MEANDIR is to continuously re-select the chemical composition of the precipitation end-member until removal of the specified $\chi^{\text{riv}}_{\text{Cl}^-\ \text{critical}}$ would not produce negative ratios for the other observations. After the inversion, comparison of the initial and inversion-constrained distributions of normalized $\chi^{\text{prec}}_{\text{Cl}^-}$ ratios can guide decisions on whether the chosen values of $\chi^{\text{riv}}_{\text{Cl}^-\ \text{critical}}$ resulted in reasonable changes to the precipitation end-member. Note that additional complexity arises when using $\chi^{\text{riv}}_{\text{Cl}^-\ \text{critical}}$ values in simulations that also account for the formation of secondary phases. In this case, removal of the specified amount of $\chi^{\text{riv}}_{\text{Cl}^-\ \text{critical}}$ resulting in negative values could be a meaningful result reflecting uptake into secondary phases. As a result, MEANDIR does not continuously re-draw the end-member compositions when using $\chi^{\text{riv}}_{\text{Cl}^-\ \text{critical}}$ values and also quantifying secondary phase formation.

Overall, MEANDIR allows the user to choose whether $\chi^{\text{riv}}_{\text{Cl}^-\ \text{critical}}$ values are used in the inversion. When $\chi^{\text{riv}}_{\text{Cl}^-\ \text{critical}}$ values are used, MEANDIR sets the contribution of the precipitation end-member and precipitation is removed from the inversion. Notably, Cl^- is not removed entirely from the inversion unless $\chi^{\text{riv}}_{\text{Cl}^-} \leq \chi^{\text{riv}}_{\text{Cl}^-\ \text{critical}}$, in which case precipitation accounts for 100% of the observed value. When $\chi^{\text{riv}}_{\text{Cl}^-\ \text{critical}}$

values are not used, $\chi^{riv}_{Cl^-}$ is treated like any other dissolved variables and precipitation is treated like any other end-member.

Mineralogical Constraints on the Evaporite End-member

Inversion models frequently include an evaporite end-member capable of sourcing $\chi^{riv}_{Cl^-}$ and other dissolved variables to river water. As a simple case, the chemical ratios characterizing such an evaporite could simply reflect user-defined distributions. However, it is also possible to limit the allowable composition of an evaporite end-member by imposing mineralogical constraints. In particular, evaporites are often considered to reflect a stoichiometric combination of gypsum ($CaSO_4 \cdot 2H_2O$) and halite (NaCl), with secondary contributions from additional phases such as epsomite ($MgSO_4 \cdot 7H_2O$) and sylvite (KCl). To reflect this mineral composition, MEANDIR is able to impose an optional constraint on an evaporite end-member that the mole contribution of SO_4^{2-} must equal the sum of contributions from Ca^{2+}, Mg^{2+}, and Sr^{2+} (eq 23), while the molar contribution of Cl^- must equal the contribution of all other cations (eq 24). We generally recommend applying this mineralogical constraint when quantifying the contributions from an evaporite end-member. Indeed, we apply the constraint during most of the inversion scenarios discussed below for data from Gaillardet and others (1999) and Burke and others (2018).

$$\chi^{evap}_{SO_4^{2-}} = \chi^{evap}_{Ca^{2+}} + \chi^{evap}_{Mg^{2+}} + \chi^{evap}_{Sr^{2+}} \tag{23}$$

$$\chi^{evap}_{Cl^-} = \chi^{evap}_{Na^+} + \chi^{evap}_{K^+} + \text{other cations} \tag{24}$$

Normalization with the Sum of Cations (χ_{Σ^+})

χ_{Na^+} is commonly used as χ_{norm} even though some common end-members, such as carbonate, do not contain substantial Na^+ (Négrel and others, 1993; Gaillardet and others, 1999). This problem has previously been addressed by using high ratios of $\chi^{carb}_{Ca^{2+}}/\chi^{carb}_{Na^+}$, such as 60 ± 30 (Burke and others, 2018), but this approach still allows for simulation results where carbonate provides a meaningful fraction of $\chi^{riv}_{Na^+}$. An alternative approach is to instead normalize to the charge-weighted sum of cations (χ_{Σ^+}, eq 25), which removes the need for a common element among all end-members and allows lithologies such as carbonate to be represented stoichiometrically (Torres and others, 2016). That is, when normalizing with χ_{Σ^+}, the carbonate end-member can have $\chi^{carb}_{Na^+}/\chi^{carb}_{\Sigma^+} = 0$ and $2\chi^{carb}_{Ca^{2+}}/\chi^{carb}_{\Sigma^+} = 1$ (the factor of 2 reflects that χ_{Σ^+} is defined in units of charge-equivalent moles, while $\chi_{Ca^{2+}}$ is defined in units of moles, and the conversion factor is 2 because that value is the charge of dissolved Ca^{2+}). Although the specific example of χ_{Σ^+} (eq 25) considers $\chi_{Ca^{2+}}$, $\chi_{Mg^{2+}}$, χ_{Na^+}, and χ_{K^+}, the mathematics underlying normalization by χ_{Σ^+} are similar regardless of which cations are included. That is, χ_{Σ^+} could also include χ_{Li^+} or $\chi_{Sr^{2+}}$, when available, or not include χ_{K^+}. We stress that normalizing to χ_{Σ^+} does not introduce new information into the inversion but is merely a restatement of measured quantities that allows for improved representation of end-members.

$$\chi_{\Sigma^+} = 2\chi_{Ca^{2+}} + 2\chi_{Mg^{2+}} + \chi_{Na^+} + \chi_{K^+} \tag{25}$$

Analogous to normalization with a single dissolved variable such as χ_{Na^+}, the ratio $\alpha_i\chi^{riv}_i/\chi^{riv}_{\Sigma^+}$ equals the sum of the end-member $\alpha_i\chi^s_i/\chi^s_{\Sigma^+}$ scaled by fractional contributions to $\chi^{riv}_{\Sigma^+}$ (eq 26, where α_i is a factor to convert between units of moles and charge for the i^{th} dissolved variable and s and s′ independently index the same list of

length n containing all end-members). Observations of dissolved river chemistry normalized with $\chi^{riv}_{\Sigma^+}$ again define a series of k linear equations where the solution vector **f** contains $f^s_{\Sigma^+}$ values (eq 26).

$$\begin{aligned}
\left(\frac{\alpha_i \chi^{riv}_i}{\chi^{riv}_{\Sigma^+}}\right) &= \left(\frac{\alpha_i \chi^{riv}_i}{2\chi^{riv}_{Ca^{2+}} + 2\chi^{riv}_{Mg^{2+}} + \chi^{riv}_{Na^+} + \chi^{riv}_{K^+}}\right) \\
&= \alpha_i \left(\frac{\Sigma^n_s[\chi^s_i]}{\Sigma^n_{s'}\left[2\chi^{s'}_{Ca^{2+}}\right] + \Sigma^n_{s'}\left[2\chi^{s'}_{Mg^{2+}}\right] + \Sigma^n_{s'}\left[\chi^{s'}_{Na^+}\right] + \Sigma^n_{s'}\left[\chi^{s'}_{K^+}\right]}\right) \\
&= \alpha_i \Sigma^n_s \left[\frac{\chi^s_i}{\Sigma^n_{s'}\left[2\chi^{s'}_{Ca^{2+}} + 2\chi^{s'}_{Mg^{2+}} + \chi^{s'}_{Na^+} + \chi^{s'}_{K^+}\right]}\right] \\
&= \alpha_i \Sigma^n_s \left[\left(\frac{\chi^s_i}{\Sigma^n_{s'}\left[2\chi^{s'}_{Ca^{2+}} + 2\chi^{s'}_{Mg^{2+}} + \chi^{s'}_{Na^+} + \chi^{s'}_{K^+}\right]}\right)\left(\frac{2\chi^s_{Ca^{2+}} + 2\chi^s_{Mg^{2+}} + \chi^s_{Na^+} + \chi^s_{K^+}}{2\chi^s_{Ca^{2+}} + 2\chi^s_{Mg^{2+}} + \chi^s_{Na^+} + \chi^s_{K^+}}\right)\right] \\
&= \alpha_i \Sigma^n_s \left[\left(\frac{2\chi^s_{Ca^{2+}} + 2\chi^s_{Mg^{2+}} + \chi^s_{Na^+} + \chi^s_{K^+}}{\Sigma^n_{s'}\left[2\chi^{s'}_{Ca^{2+}} + 2\chi^{s'}_{Mg^{2+}} + \chi^{s'}_{Na^+} + \chi^{s'}_{K^+}\right]}\right)\left(\frac{\chi^s_i}{2\chi^s_{Ca^{2+}} + 2\chi^s_{Mg^{2+}} + \chi^s_{Na^+} + \chi^s_{K^+}}\right)\right] \\
&= \Sigma^n_s \left[f^s_{\Sigma^+}\left(\frac{\alpha_i \chi^s_i}{\chi^s_{\Sigma^+}}\right)\right]
\end{aligned} \tag{26}$$

Normalization with χ_{Σ^+} does not simply result in the equation $1 = \Sigma^n_s\left[f^s_{\Sigma^+}\right]$. This is different from normalization with χ_{Na^+}, where the equation $1 = \Sigma^n_s\left[f^s_{Na^+}\right]$ resulted naturally from the mass balance equation corresponding to the variable χ_{Na^+} (eq 13). However, the equation $1 = \Sigma^n_s\left[f^s_{\Sigma^+}\right]$ can be reached as the sum of mass balance equations for the individual variables normalized by $\chi^{riv}_{\Sigma^+}$ (eq 27). Including the equation $1 = \Sigma^n_s\left[f^s_{\Sigma^+}\right]$ in the inversion is thus degenerate when the mass balance equations for all the elements contributing to χ_{Σ^+} are included. Stated another way, an inversion consisting of concentration data for $\chi^{riv}_{Na^+}$, $\chi^{riv}_{K^+}$, $\chi^{riv}_{Ca^{2+}}$, and $\chi^{riv}_{Mg^{2+}}$ yields a maximum of 4 mixing equations for inversion regardless of whether normalizing the data by one element (χ_{Na^+}) or the sum of all the major cations (χ_{Σ^+}).

$$\begin{aligned}
1 &= \left(\frac{2\chi^{riv}_{Ca^{2+}}}{\chi^{riv}_{\Sigma^+}}\right) + \left(\frac{2\chi^{riv}_{Mg^{2+}}}{\chi^{riv}_{\Sigma^+}}\right) + \left(\frac{\chi^{riv}_{Na^+}}{\chi^{riv}_{\Sigma^+}}\right) + \left(\frac{\chi^{riv}_{K^+}}{\chi^{riv}_{\Sigma^+}}\right) \\
&= \Sigma^n_s\left[f^s_{\Sigma^+}\left(\frac{2\chi^s_{Ca^{2+}}}{\chi^s_{\Sigma^+}}\right)\right] + \Sigma^n_s\left[f^s_{\Sigma^+}\left(\frac{2\chi^s_{Mg^{2+}}}{\chi^s_{\Sigma^+}}\right)\right] + \Sigma^n_s\left[f^s_{\Sigma^+}\left(\frac{\chi^s_{Na^+}}{\chi^s_{\Sigma^+}}\right)\right] + \Sigma^n_s\left[f^s_{\Sigma^+}\left(\frac{\chi^s_{K^+}}{\chi^s_{\Sigma^+}}\right)\right] \\
&= \Sigma^n_s\left[f^s_{\Sigma^+}\left(\frac{2\chi^s_{Ca^{2+}} + 2\chi^s_{Mg^{2+}} + \chi^s_{Na^+} + \chi^s_{K^+}}{\chi^s_{\Sigma_+}}\right)\right] = \Sigma^n_s\left[f^s_{\Sigma^+}\right]
\end{aligned} \tag{27}$$

When $\chi_{norm} = \chi_{\Sigma^+}$, the set of river water ratios will be internally consistent when the denominator $\chi^{riv}_{\Sigma^+}$ is calculated using the values of $\chi^{riv}_{Ca^{2+}}$, $\chi^{riv}_{Mg^{2+}}$, $\chi^{riv}_{Na^+}$, $\chi^{riv}_{K^+}$, $\chi^{riv}_{Sr^{2+}}$, *et cetera* in the numerators of each ratio. However, ensuring internal consistency is more challenging when selecting end-member ratios from user-defined distributions. If all $\alpha_i \chi^s_i / \chi^s_{\Sigma^+}$ ratios are selected from given distributions, the resulting set of

values will not necessarily sum to unity and would define an internally inconsistent end-member. For example, when χ_{Σ^+} includes $\chi_{Ca^{2+}}$, $\chi_{Mg^{2+}}$, χ_{Na^+}, and χ_{K^+}, only three of the four χ_{Σ^+}-normalized ratios can be selected independently from user-supplied end-member distributions before the fourth is uniquely defined. It is convenient to select a number of $\alpha_i \chi_i^s / \chi_{\Sigma^+}^s$ ratios from their respective distributions equal to 1 less than the number of cations constituent to χ_{Σ^+} and calculate the final ratio by difference from 1 to ensure the internal consistency of the end-member. In general, the ratio calculated by mass balance should be that with the largest expected $\alpha_i \chi_i^s / \chi_{\Sigma^+}^s$ value.

An additional constraint from charge balance occurs when all major cations and anions are included in the inversion. In this case, the sum of cation ratios normalized with χ_{Σ^+} must equal the sum of the anion ratios normalized with χ_{Σ^+} (eq 28). Similar to ensuring the internal consistency of each end-member by selecting one $\alpha_i \chi_i^s / \chi_{\Sigma^+}^s$ ratio to be calculated from the other selections, charge balance is attained by defining a second $\alpha_i \chi_i^s / \chi_{\Sigma^+}^s$ ratio for each end-member to be calculated from the other selections.

$$1 = \frac{2\chi_{Ca^{2+}}}{\chi_{\Sigma^+}} + \frac{2\chi_{Mg^{2+}}}{\chi_{\Sigma^+}} + \frac{\chi_{Na^+}}{\chi_{\Sigma^+}} + \frac{\chi_{K^+}}{\chi_{\Sigma^+}} = \frac{2\chi_{SO_4^{2-}}}{\chi_{\Sigma^+}} + \frac{\chi_{Cl^-}}{\chi_{\Sigma^+}} + \frac{\chi_{HCO_3^-}}{\chi_{\Sigma^+}} \tag{28}$$

When normalizing with χ_{Σ^+}, the user inputs to MEANDIR which elements should be included in the normalization variable and provides end-member distributions for $\alpha_i \chi_i^s / \chi_{\Sigma^+}^s$. Furthermore, the user specifies which of the constituent variables should be calculated through mass balance to ensure the internal consistency of each end-member. When all cations and anions are included in the inversion, the user also selects which variable for each end-member should be calculated through charge balance. MEANDIR does not currently allow the ratio calculated by charge balance to have its numerator constituent to the normalization variable; if the normalization is the sum of $2\chi_{Ca^{2+}}$, $2\chi_{Mg^{2+}}$, and χ_{Na^+}, neither $\chi_{Ca^{2+}}$, $\chi_{Mg^{2+}}$, or χ_{Na^+} could be used to ensure charge balance (eq 28).

Modeling the Formation of Secondary Phases with Isotopic Fractionation

The formation of secondary clays and calcite is common in river systems (Gíslason and others, 1996; Jacobson and others, 2002; Bickle and others, 2015, 2018). While end-members in river mixing models typically source dissolved constituents to solution and contribute positively to river dissolved load, secondary phases can be viewed as end-members that remove dissolved constituents from solution and contribute negatively to river dissolved load. In MEANDIR, the formation of secondary phases is represented as end-members that make negative contributions to the normalization variable ($\chi_{norm}^s < 0$, $f_{norm}^s < 0$). As a result, in inversions including the formation of secondary phases the sum of fractional contributions from primary end-members may exceed the upper boundary of the user-defined range for sample matching while the sum of fractional contributions from all end-members will still fall within the user-defined criteria.

Robust quantification of secondary phase formation requires that secondary products are chemically distinct from the primary lithologies. Secondary clays are often distinct from bedrock and form with isotopic fractionation, suggesting that river mixing models should be able to accurately quantify clay formation. Likewise, MEANDIR can be used to quantify the formation of secondary carbonate if there is a chemical distinction relative to the weathering end-members. In the absence of a chemical or isotopic signal to differentiate primary from secondary carbonate, such as

$\chi^{s}_{Ca^{2+}}/\chi^{s}_{Mg^{2+}}$ or $^{44}Ca/^{40}Ca$, formation of secondary calcite is difficult to separate from a scenario with less gross carbonate weathering.

Modeling river isotopic ratios in the presence of a secondary solute sink requires approaches for both stable isotopic systems, where secondary phases can have different isotopic compositions relative to primary minerals, and radiogenic isotopic systems, where isotopic fractionation is relatively small such that secondary phases have a similar isotopic composition to the weighted sum of all solute sources. For example, secondary silicate minerals tend to have lower $\delta^{30}Si$ values relative to all primary mineral sources and the magnitude of the isotopic offset tends to vary with the amount of the total Si supply that is incorporated into secondary minerals (Bouchez and others, 2013). Conversely, mass-dependent fractionation in systems such as $^{87}Sr/^{86}Sr$ may be much smaller than radiogenic variations among the sources of Sr^{2+} to river water (de Souza and others, 2010), leading the $^{87}Sr/^{86}Sr$ ratio of clays to approximately match the Sr isotope ratio of sources to the river.

To address these complexities MEANDIR allows users to define the elemental or isotopic composition of secondary end-members relative to the measured values of individual samples or with fractionation relative to sources of the relevant element from all other end-members. For example, rather than setting distributions for the isotopic ratio of a clay end-member prior to inversion, MEANDIR can define the clay $^{87}Sr/^{86}Sr$ ratio to equal the $^{87}Sr/^{86}Sr$ ratio in each river water sample or to equal the $^{87}Sr/^{86}Sr$ ratio of all weathering sources. Similarly, MEANDIR can set the clay end-member to have a $^{30}Si/^{28}Si$ ratio pulled from a uniform distribution corresponding to 1‰ to 2‰ lower than the sample $\delta^{30}Si$ value, or to have its $^{30}Si/^{28}Si$ ratio equal to a value fractionated relative to weathering inputs. As with pre-defined chemical distributions, users can select if the isotopic composition of a secondary end-member should have a normal, uniform, or log-uniform distribution of fractionation factors or of values offset from the observed value.

The isotopic composition of secondary phases formed with fractionation depends on the contribution and isotopic composition of all other end-members in the inversion. The isotopic composition of a secondary phase thus cannot be set prior to inversion because it depends on the inversion results. This is fundamentally different from weathering end-members, where user-defined end-member distributions are selected prior to inversion. MEANDIR addresses this problem by employing the optimization process to iteratively re-define the isotopic value of secondary end-members while also solving for fractional contributions, allowing for the representation of isotopic fractionation during the formation of secondary phases.

MEANDIR's treatment of fractionation utilizes a user-supplied fractionation factor (Δ_i) or distribution of fractionation factors that set the degree of isotopic discrimination during secondary phase formation (eq 29, where we use the superscript s^{second} to refer to a generic secondary phase such as a clay, and negative values of Δ_i reflect isotope effects favoring the movement of the light isotope to the secondary phase). In turn, the isotopic difference between the river and the contribution-weighted isotopic composition of sources is equal to the fractionation factor scaled by fractional uptake into the secondary phase (eq 30; Bouchez and others, 2013). Rearranging these equations yields an expression for the isotopic composition of the secondary phase (eq 31) as a function of the fractional contributions of each end-member (eq 32). MEANDIR is able to account for fractionation during the formation of secondary phases by repeatedly applying equation (32) during the optimization process to continuously re-define the isotopic composition of secondary phases based on the active values for the fractional contributions. In considering equation (29) to equation (32), recall

that f_i^{second} is negative when there is net formation of a secondary phase, and that a negative value of Δ_i favors movement of the lighter isotope to the secondary phase.

$$ {}^{A}R_i^{second} - {}^{A}R_i^{riv} = \Delta_i \tag{29} $$

$$ {}^{A}R_i^{riv} - {}^{A}R_i^{source} = \left(\frac{f_i^{second}}{\Sigma_{s_i}^{n_i^{source}} \left[f_i^{s_i^{source}} \right]} \right) \Delta_i \tag{30} $$

$$ {}^{A}R_i^{second} = ({}^{A}R_i^{source} + \Delta_i) + \left(\frac{f_i^{second}}{\Sigma_{s_i}^{n_i^{source}} \left[f_i^{s_i^{source}} \right]} \right) \Delta_i \tag{31} $$

$$ {}^{A}R_i^{second} = \left(\frac{\Sigma_{s_i}^{n_i^{source}} \left[f_i^{s_i^{source}} \cdot {}^{A}R_i^{s_i^{source}} \right]}{\Sigma_{s_i}^{n_i^{source}} \left[f_i^{s_i^{source}} \right]} + \Delta_i \right) + \left(\frac{f_i^{second}}{\Sigma_{s_i}^{n_i^{source}} \left[f_i^{s_i^{source}} \right]} \right) \Delta_i \tag{32} $$

In summary, MEANDIR quantifies the formation of secondary phases by allowing the fractional contributions from those end-members to be negative. Moreover, MEANDIR provides three mechanisms for regulating the isotopic composition of secondary phases. First, users can simply set a desired distribution of values. Second, users can define the isotopic composition of the secondary phase relative to the observed value for each river water sample. However, because the water chemistry reconstructed by MEANDIR may not perfectly match observations, this approach does not guarantee agreement between model-constructed river chemistry and the isotopic value of the secondary phase. For example, when setting the $^{87}Sr/^{86}Sr$ ratio of a secondary phase equal to the sample ratio, the $^{87}Sr/^{86}Sr$ ratio of the secondary phase may differ from the inversion-constructed $^{87}Sr/^{86}Sr$ ratio of river water. Conversely, in the final method users can define a fractionation factor that sets the isotopic offset of secondary phases from the sources of the corresponding element. For the same example, if the fractionation factor is set to zero, the $^{87}Sr/^{86}Sr$ ratio of the secondary phase would match the reconstructed value of river water chemistry, but both would likely be offset from the actual measured value. Although all three approaches have their uses depending on the specific isotopic system and environment under consideration, we generally recommend the final treatment when seeking an internally consistent method for quantifying the formation of secondary phases with or without isotopic fractionation.

Sulfide Oxidation

FeS_2 oxidation consumes ALK and increases both the concentration of marine SO_4^{2-} and atmospheric pCO_2. Currently, the river inversion literature contains two main approaches for calculating the fraction of $\chi_{SO_4^{2-}}^{riv}$ derived from FeS_2 oxidation, both of which can be implemented in MEANDIR (Torres and others, 2016; Burke and others, 2018; Hemingway and others, 2020; Kemeny and others, 2021a). After discussing these two techniques, later in this text we present a third, improved method for quantifying the fraction of $\chi_{SO_4^{2-}}^{riv}$ derived from FeS_2 oxidation and evaluate the mutual consistency of the three approaches.

Burke and others (2018) quantified $\chi_{SO_4^{2-}}^{riv}$ which could not be attributed to precipitation, evaporites, carbonates, or silicates and called this quantity "excess SO_4^{2-}"

(in our notation, $\chi^{riv}_{excess\ SO_4^{2-}}$) (eq 33), which is proposed to mainly derive from FeS_2 oxidation and anthropogenic inputs. When quantifying FeS_2 oxidation this way the inversion must first calculate the fractional contributions of end-members using the non-SO_4^{2-} variables and, after the inversion is complete, each $\chi^{s}_{SO_4^{2-}}$ value can be calculated to then compute $\chi^{riv}_{excess\ SO_4^{2-}}$. In this approach $\chi^{riv}_{SO_4^{2-}}$ values should not be included directly in the inversion; if they are the second term of equation (33) $\left(\Sigma^{n}_{s}\left[\chi^{s}_{SO_4^{2-}}\right]\right)$ will be optimized to equal the first term of equation (33) ($\chi^{riv}_{SO_4^{2-}}$) and leave $\chi^{riv}_{excess\ SO_4^{2-}}$ as the residual of the optimization. Likewise, $^{34}R^{riv}_{excess\ SO_4^{2-}}$ is calculated following inversion from $^{34}R^{riv}_{SO_4^{2-}}$ and each $^{34}R^{s}_{SO_4^{2-}}$ values (eq 34).

$$\chi^{riv}_{excess\ SO_4^{2-}} = \chi^{riv}_{SO_4^{2-}} - \Sigma^{n}_{s}\left[\chi^{s}_{SO_4^{2-}}\right] \tag{33}$$

$$^{34}R^{riv}_{excess\ SO_4^{2-}} = \frac{\left(\chi^{riv}_{SO_4^{2-}} \cdot {}^{34}R^{riv}_{SO_4^{2-}}\right) - \Sigma^{n}_{s}\left[\chi^{s}_{SO_4^{2-}} \cdot {}^{34}R^{s}_{SO_4^{2-}}\right]}{\chi^{riv}_{SO_4^{2-}} - \Sigma^{n}_{s}\left[\chi^{s}_{SO_4^{2-}}\right]} \tag{34}$$

An advantage of the Burke and others (2018) treatment is that, because it solves for the total amount and isotopic composition of $\chi^{riv}_{excess\ SO_4^{2-}}$ after the inversion is complete, it does not incur computational expense from testing values of normalized $\chi^{s}_{SO_4^{2-}}$ or $^{34}R^{s}_{SO_4^{2-}}$. Second, this treatment allows for identification of $\chi^{riv}_{SO_4^{2-}}$ in excess of conservative mixing without explicitly assuming its source, leaving open the interpretation of $\chi^{riv}_{excess\ SO_4^{2-}}$. Conversely, by not explicitly connecting sources of SO_4^{2-} with carbonate or silicate weathering, this method does not easily resolve the relative fractions of carbonate or silicate weathering driven with H_2SO_4. This approach also allows the inversion to over-predict measured $\chi^{riv}_{SO_4^{2-}}$, resulting in negative values of $\chi^{riv}_{excess\ SO_4^{2-}}$.

A second approach, used in Torres and others (2016), Hemingway and others (2020), and Kemeny and others (2021a), assigns a value for normalized SO_4^{2-} to a subset of end-members that do not contain structural SO_4^{2-}. In this case, the normalized ratios do not reflect SO_4^{2-} sourced from the lithology itself, but instead reflect SO_4^{2-} released into solution when H_2SO_4 formed through FeS_2 oxidation weathers the corresponding end-member. In our notation we reference this type of FeS_2-derived SO_4^{2-} as "FeS_2 SO_4^{2-}". For example, a silicate rock without structural SO_4^{2-} would have $2\chi^{slct}_{SO_4^{2-}}/\chi^{slct}_{\Sigma^+} = 0$, while a silicate rock where 50% of weathering is done by H_2SO_4 would have $2\chi^{slct}_{FeS_2\ SO_4^{2-}}/\chi^{slct}_{\Sigma^+} = 0.5$. Following inversion, $^{34}R_{FeS_2\ SO_4^{2-}}$ is calculated from $^{34}R^{riv}_{SO_4^{2-}}$ and $^{34}R^{s}_{SO_4^{2-}}$ (eqs 35 and 36, where $s_{FeS_2\ SO_4^{2-}}$ indexes a list of length $n_{FeS_2\ SO_4^{2-}}$ containing end-members where SO_4^{2-} reflects FeS_2 oxidation and $s_{SO_4^{2-}}$ indexes a list of length $n_{SO_4^{2-}}$ containing end-members where SO_4^{2-} reflects non-FeS_2-derived SO_4^{2-}). Unlike the inversion scheme of Burke and others (2018), this approach constrains the normalized $\chi^{s}_{FeS_2\ SO_4^{2}}$ ratios for each end-member and prevents negative values of $\chi^{riv}_{excess\ SO_4^{2-}}$. However, as shown below, this approach can result in problematic behavior at low values of $2\chi^{riv}_{SO_4^{2-}}/\chi^{riv}_{\Sigma^+}$.

$$\chi^{\mathrm{riv}}_{\mathrm{FeS_2\ SO_4^{2-}}} = \Sigma^{\mathrm{n_{FeS_2\ SO_4^{2-}}}}_{\mathrm{s_{FeS_2\ SO_4^{2-}}}} \left[\chi^{\mathrm{s_{FeS_2\ SO_4^{2-}}}}_{\mathrm{FeS_2\ SO_4^{2-}}} \right] \tag{35}$$

$$^{34}\mathrm{R}^{\mathrm{riv}}_{\mathrm{FeS_2\ SO_4^{2-}}} = \frac{\left(\chi^{\mathrm{riv}}_{\mathrm{SO_4^{2-}}} \cdot {}^{34}\mathrm{R}^{\mathrm{riv}}_{\mathrm{SO_4^{2-}}} \right) - \Sigma^{\mathrm{n_{SO_4^{2-}}}}_{\mathrm{s_{SO_4^{2-}}}} \left[\chi^{\mathrm{s_{SO_4^{2-}}}}_{\mathrm{SO_4^{2-}}} \cdot {}^{34}\mathrm{R}^{\mathrm{s_{SO_4^{2-}}}}_{\mathrm{SO_4^{2-}}} \right]}{\Sigma^{\mathrm{n_{FeS_2\ SO_4^{2-}}}}_{\mathrm{s_{FeS_2\ SO_4^{2-}}}} \left[\chi^{\mathrm{s_{FeS_2\ SO_4^{2-}}}}_{\mathrm{FeS_2\ SO_4^{2-}}} \right]} \tag{36}$$

In Torres and others (2016) the silicate and carbonate end-members had well-defined values of $^{34}\mathrm{R}^{\mathrm{s}}_{\mathrm{FeS_2\ SO_4^{2-}}}$ in addition to normalized $\chi^{\mathrm{s}}_{\mathrm{FeS_2\ SO_4^{2-}}}$ ratios. This choice was motivated by actual measurements of FeS_2 $\delta^{34}S$ such that the inclusion of sulfur isotope ratios added new constraint to the inversion. When FeS_2 $\delta^{34}S$ has not been measured, including $\delta^{34}S$ in the inversion merely adds computational expense to isolate the subset of simulations that select the correct $^{34}\mathrm{R}^{\mathrm{s}}_{\mathrm{FeS_2\ SO_4^{2-}}}$ value to generate $^{34}\mathrm{R}^{\mathrm{riv}}_{\mathrm{SO_4^{2-}}}$ given a successful combination of normalized $\chi^{\mathrm{s}}_{\mathrm{FeS_2\ SO_4^{2-}}}$ values. In this case, it is more efficient to instead calculate the $\delta^{34}S$ of FeS_2-derived SO_4^{2-} after the inversion is complete (Kemeny and others, 2021a).

Including $\chi^{riv}_{HCO_3^-}$ in Inversions

Quantifying sources of $\chi^{\mathrm{riv}}_{\mathrm{HCO_3^-}}$ and interpreting $^{13}\mathrm{R}^{\mathrm{riv}}_{\mathrm{HCO_3^-}}$ are recalcitrant problems in river geochemistry. In part, this difficulty reflects that the non-conservative behavior of $\chi^{\mathrm{riv}}_{\mathrm{HCO_3^-}}$, the specific methods used to determine $\chi^{\mathrm{riv}}_{\mathrm{HCO_3^-}}$, and the numerical approaches to quantifying sources of $\chi^{\mathrm{riv}}_{\mathrm{HCO_3^-}}$ each engender substantial confusion. Each of these problems is briefly discussed below. Later in this article, we present a method of river inversion focused on quantifying sources of $\chi^{\mathrm{riv}}_{\mathrm{ALK}}$ and $\chi^{\mathrm{riv}}_{\mathrm{DIC}}$ rather than $\chi^{\mathrm{riv}}_{\mathrm{HCO_3^-}}$.

In-situ $\chi^{\mathrm{riv}}_{\mathrm{HCO_3^-}}$ is determined by *in-situ* $\chi^{\mathrm{riv}}_{\mathrm{ALK}}$ and *in-situ* $\chi^{\mathrm{riv}}_{\mathrm{DIC}}$. As processes such as carbonate weathering, degassing, and aquatic respiration alter $\chi^{\mathrm{riv}}_{\mathrm{DIC}}$, or processes such as FeS_2 oxidation or weathering alter $\chi^{\mathrm{riv}}_{\mathrm{ALK}}$, the value of $\chi^{\mathrm{riv}}_{\mathrm{HCO_3^-}}$ does not change linearly. That is, due to the speciation dynamics of dissolved CO_2, $\chi^{\mathrm{riv}}_{\mathrm{HCO_3^-}}$ is not a weighted linear combination of lithologic and atmospheric sources reflecting the integrated history of upstream chemical processes. The non-linearity of $\chi^{\mathrm{riv}}_{\mathrm{HCO_3^-}}$ may present substantial complexity when using linear algebra to model its sources, although there are also situations in which the error is likely to be negligible. In contrast, $\chi^{\mathrm{riv}}_{\mathrm{ALK}}$ and $\chi^{\mathrm{riv}}_{\mathrm{DIC}}$ do mix linearly. Moreover, $\chi^{\mathrm{riv}}_{\mathrm{ALK}}$ and $\chi^{\mathrm{riv}}_{\mathrm{DIC}}$ are often the quantities actually measured during research on river systems and later used to infer $\chi^{\mathrm{riv}}_{\mathrm{HCO_3^-}}$. While $\chi^{\mathrm{riv}}_{\mathrm{ALK}}$, $\chi^{\mathrm{riv}}_{\mathrm{DIC}}$, and $\chi^{\mathrm{riv}}_{\mathrm{HCO_3^-}}$ are occasionally viewed as interchangeable, and indeed one can sometimes be used as an approximation for the others, their mutual distinctions become important when using MEANDIR to model processes such as FeS_2 oxidation and CO_2 degassing across the river-atmosphere boundary; FeS_2 oxidation impacts $\chi^{\mathrm{riv}}_{\mathrm{ALK}}$, CO_2 degassing impacts $\chi^{\mathrm{riv}}_{\mathrm{DIC}}$, and both alter $\chi^{\mathrm{riv}}_{\mathrm{HCO_3^-}}$.

Quantification of $\chi^{\mathrm{riv}}_{\mathrm{HCO_3^-}}$ often occurs either through measurement of $\chi^{\mathrm{riv}}_{\mathrm{ALK}}$ or through calculation by charge balance. In the former case, it is typical to assume that $\chi^{\mathrm{riv}}_{\mathrm{HCO_3^-}}$ equals $\chi^{\mathrm{riv}}_{\mathrm{ALK}}$, which is generally an appropriate assumption for rivers near circumneutral pH and without substantial organic matter content. In the case of charge balance, $\chi^{\mathrm{riv}}_{\mathrm{HCO_3^-}}$ is quantified as the difference between the charge-equivalent sum of conservative cations and conservative anions. When $\chi^{\mathrm{riv}}_{\mathrm{HCO_3^-}}$ is determined through

charge balance, it only provides new information for the inversion when the constituent measurements are not all included in the inversion. For example, if $\chi_{Ca^{2+}}$, $\chi_{Mg^{2+}}$, $\chi_{Na^{+}}$, $\chi_{K^{+}}$, $\chi_{SO_4^{2-}}$, and $\chi_{Cl^{-}}$ are all included in the inversion, the mass balance equation for $\chi^{riv}_{HCO_3^-}$ would be degenerate with a linear combination of the other equations. Notably, including a degenerate equation in the inversion can result in a different answer than in an inversion with only linearly independent information because the additional equation still contributes to the cost function. Indeed, it can be useful to include $\chi^{riv}_{HCO_3^-}$ in inversions to ensure that results match the value of $\chi^{riv}_{HCO_3^-}$ to within a user-specified range for sample matching. MEANDIR thus allows the user to include the constraint that inversion results should recreate $\chi^{riv}_{HCO_3^-}$ within a specified range, but not include the misfit of $\chi^{riv}_{HCO_3^-}/\chi^{riv}_{\Sigma^+}$ when evaluating the cost function.

Analogous to FeS_2 oxidation and weathering with H_2SO_4, the addition of HCO_3^- to rivers from weathering with H_2CO_3 is often reflected within the end-member values of $\chi^{s}_{HCO_3^-}/\chi^{s}_{\Sigma^+}$. For silicate, $\chi^{slct}_{HCO_3^-}$ entirely reflects HCO_3^- sourced from the deprotonation of atmospheric CO_2. For carbonate, $\chi^{carb}_{HCO_3^-}$ has previously represented the combination of structural CO_3^{2-} and atmospheric CO_2. Recent work has explicitly separated the weathering of carbonate and silicate end-members with carbonic or sulfuric acid (Blattmann and others, 2019). In this case, each end-member reflects a single lithology being weathered with a single acid. Rather than having an end-member for each type of lithology with variable $\chi^{s}_{HCO_3^-}/\chi^{s}_{\Sigma^+}$ and $2\chi^{s}_{FeS_2\ SO_4^{2-}}/\chi^{s}_{\Sigma^+}$, the explicit separation requires two end-members for each type of lithology where each has fixed ratios for $\chi^{s}_{HCO_3^-}/\chi^{s}_{\Sigma^+}$ and $2\chi^{s}_{FeS_2\ SO_4^{2-}}/\chi^{s}_{\Sigma^+}$. Below, we compare results when using variable or fixed ratios of $\chi^{s}_{HCO_3^-}/\chi^{s}_{\Sigma^+}$.

Overall, MEANDIR is able to invert observations of $\chi^{riv}_{HCO_3^-}$, ${}^{13}R^{riv}_{HCO_3^-}$, and ${}^{14}R^{riv}_{HCO_3^-}$ for the fractional contributions of end-members by assuming linear behavior of user-defined end-member ratios. Furthermore, MEANDIR is able to invert observations of χ^{riv}_{ALK} and χ^{riv}_{DIC}, as well as measurements of ${}^{13}R^{riv}_{DIC}$ and ${}^{14}R^{riv}_{DIC}$. While MEANDIR represents a step forward in inverting observations of dissolved CO_2, studies of ${}^{13}R^{riv}_{DIC}$ and ${}^{13}R^{riv}_{HCO_3^-}$ may continue to be hindered by fractionation during degassing and the continued re-equilibration among dissolved CO_2 species. Although it is possible that degassing could be approximated using the approach MEANDIR takes to model isotopic fractionation during secondary phase formation, along with a deliberate choice of normalization variable, this idea has not been independently tested and may not capture important complexities that are explicitly resolved in purpose-built models of river gas exchange (Polsenaere and Abril, 2012).

Writing Chemical Weathering Reactions with DIC as HCO_3^- or H_2CO_3

The geochemical literature on river inversion contains competing standards of how to write the basic chemical reactions for weathering of carbonate and silicate minerals with H_2CO_3 and H_2SO_4. The different equations matter because they generate variable expectations for carbonate $2\chi^{carb}_{FeS_2\ SO_4^{2-}}/\chi^{carb}_{\Sigma^+}$ and impede comparison across studies attempting to quantify the role of FeS_2 oxidation in the long-term carbon cycle. The difference in weathering equations results from whether reactions are written with chemical species at the circumneutral pH of most rivers or at the carbonic acid equivalence point (Zeebe and Wolf-Gladrow, 2001). More broadly, these different equations reflect differing opinions on the importance of DIC degassing during downstream transport.

When written at ambient conditions with DIC in the form of HCO_3^- (eqs 37–40), carbonate weathering is constrained to have $\chi^{carb}_{HCO_3^-}/\chi^{carb}_{\Sigma^+}$ between 0.5 and 1 (eqs 37 and 38) and silicate weathering is constrained to have $\chi^{slct}_{HCO_3^-}/\chi^{slct}_{\Sigma^+}$ between 0 and 1 (eqs 39 and 40). Similarly, the carbonate end-member $2\chi^{carb}_{FeS_2\ SO_4^{2-}}/\chi^{carb}_{\Sigma^+}$ is bounded between 0 (eq 37) and 0.5 (eq 38), while silicate $2\chi^{slct}_{FeS_2\ SO_4^{2-}}/\chi^{slct}_{\Sigma^+}$ is bounded between 0 (eq 39) and 1 (eq 40).

$$\frac{1}{2}CaCO_3 + \frac{1}{2}CO_2 + \frac{1}{2}H_2O \rightarrow \frac{1}{2}Ca^{2+} + HCO_3^- \tag{37}$$

$$\frac{1}{2}CaCO_3 + \frac{1}{8}FeS_2 + \frac{15}{32}O_2 + \frac{1}{4}H_2O \rightarrow \frac{1}{2}Ca^{2+} + \frac{1}{2}HCO_3^- + \frac{1}{4}SO_4^{2-} + \frac{1}{16}Fe_2O_3 \tag{38}$$

$$\frac{1}{2}CaSiO_3 + CO_2 + \frac{1}{2}H_2O \rightarrow \frac{1}{2}Ca^{2+} + \frac{1}{2}SiO_2 + HCO_3^- \tag{39}$$

$$\frac{1}{2}CaSiO_3 + \frac{1}{4}FeS_2 + \frac{15}{16}O_2 \rightarrow \frac{1}{2}Ca^{2+} + \frac{1}{2}SiO_2 + \frac{1}{2}SO_4^{2-} + \frac{1}{8}Fe_2O_3 \tag{40}$$

When written at the carbonic acid equivalence point (eqs 41–44), both carbonate $2\chi^{carb}_{FeS_2\ SO_4^{2-}}/\chi^{carb}_{\Sigma^+}$ and silicate $2\chi^{slct}_{FeS_2\ SO_4^{2-}}/\chi^{slct}_{\Sigma^+}$ are bounded between 0 (eqs 41 and 43) and 1 (eqs 42 and 44). The higher value for carbonate $2\chi^{carb}_{FeS_2\ SO_4^{2-}}/\chi^{carb}_{\Sigma^+}$ in this second set of equations occurs because DIC from the carbonate mineral is now written as the uncharged species H_2CO_3, not as the charged species HCO_3^-. As a result, the positive charge of $\chi^{carb}_{Ca^{2+}}$ is compensated by the negative charge of $\chi^{carb}_{FeS_2\ SO_4^{2-}}$ and not the negative charge of $\chi^{carb}_{HCO_3^-}$. Because weathering of silicate minerals with sulfuric acid does not result in release of HCO_3^-, equations (40) and (44) are identical.

$$\frac{1}{2}CaCO_3 + H^+ \rightarrow \frac{1}{2}Ca^{2+} + \frac{1}{2}H_2CO_3 \tag{41}$$

$$\frac{1}{2}CaCO_3 + \frac{1}{4}FeS_2 + \frac{15}{16}O_2 + \frac{1}{2}H_2O \rightarrow \frac{1}{2}Ca^{2+} + \frac{1}{2}H_2CO_3 + \frac{1}{2}SO_4^{2-} + \frac{1}{8}Fe_2O_3 \tag{42}$$

$$\frac{1}{2}CaSiO_3 + H^+ \rightarrow \frac{1}{2}Ca^{2+} + \frac{1}{2}SiO_2 + \frac{1}{2}H_2O \tag{43}$$

$$\frac{1}{2}CaSiO_3 + \frac{1}{4}FeS_2 + \frac{15}{16}O_2 \rightarrow \frac{1}{2}Ca^{2+} + \frac{1}{2}SiO_2 + \frac{1}{2}SO_4^{2-} + \frac{1}{8}Fe_2O_3 \tag{44}$$

There are thus two common sets of values for $2\chi^{carb}_{FeS_2\ SO_4^{2-}}/\chi^{carb}_{\Sigma^+}$ that differ only in the choice of whether DIC released during weathering is written as H_2CO_3 or HCO_3^-. Moreover, while both sets of weathering reactions predict that $2\chi^{riv}_{SO_4^{2-}}/\chi^{riv}_{\Sigma^+} \leq 1$, natural waters with $2\chi^{riv}_{SO_4^{2-}}/\chi^{riv}_{\Sigma^+} > 1$ have been reported (Torres and others, 2016). As an extreme example, $2\chi^{riv}_{SO_4^{2-}}$ can substantially exceed $\chi^{riv}_{\Sigma^+}$ in acid mine drainage (Hubbard and others, 2009). These observations show that FeS_2 oxidation can

proceed without weathering of either carbonate or silicate lithologies, and that neither set of equations (eqs 37–40, 41–44) fully captures relevant weathering dynamics. As described below, MEANDIR begins to address this problem by explicitly separating the production and consumption of ALK, rather than explicitly tying together the source of acid and the weathering lithology; this new framework allows MEANDIR to model river waters where $2\chi^{riv}_{SO_4^{2-}}/\chi^{riv}_{\Sigma^+} > 1$.

Oxidation of FeS_2 and C_{org} as Independent End-members

The preceding sections discussed normalization to χ_{Σ^+}, accounting for $\chi^{riv}_{SO_4^{2-}}$ sourced from FeS_2 oxidation, including $\chi^{riv}_{HCO_3^-}$ in the inversion, and the different forms of chemical weathering reactions. In this section, we extend prior techniques to propose a new normalization strategy that allows for direct representation of FeS_2 oxidation, C_{org} oxidation, and CO_2 degassing as independent end-members decoupled from chemical weathering of lithologic end-members. The development underlying our approach is the inclusion of additional dissolved constituents into the normalization variable, such as $\chi^{riv}_{SO_4^{2-}}$, χ^{riv}_{ALK}, or χ^{riv}_{DIC}. Similar to how normalization by χ_{Σ^+} rather than χ_{Na^+} allows a carbonate end-member to become stoichiometric, normalization to additional sums of variables enables representation of new end-member and processes that have previously eluded direct quantification. The myriad applications of our new method include disentangling contributions to $\chi^{riv}_{SO_4^{2-}}$ from multiple FeS_2 end-members with distinct $\delta^{34}S$ values and apportioning χ^{riv}_{DIC} between carbonate weathering, atmospheric CO_2, and petrogenic C_{org} oxidation. Example end-member compositions for several prior and new normalizations are given in table 4.

Normalization with arbitrary sum of dissolved variables.—We first derive the basic mass balance equations of normalization with an arbitrary sum of dissolved constituents (eq 45, with i_{norm} indexing a list of length k_{norm} containing all variables included in the normalization χ_{norm}, and eq 46, where s and s′ independently index the same list of length n containing all end-members in the inversion). The derivation of the general equation follows the logic of our earlier derivation for the specific case of normalization with χ_{Σ^+} (eq 26). As before, normalization with an arbitrary sum of dissolved variables generates a series of k linear equations that can be written as $\mathbf{b} = \mathbf{A} \cdot \mathbf{f}$ where each equation is of the form $\alpha_i \chi^{riv}_i / \chi^{riv}_{norm} = \Sigma^n_s \left[f^s_{norm} \left(\frac{\alpha_i \chi^s_i}{\chi^s_{norm}} \right) \right]$ (eq 46).

$$\chi_{norm} = \Sigma^{k_{norm}}_{i_{norm}} \left[\alpha_{i_{norm}} \chi_{i_{norm}} \right] \tag{45}$$

$$\begin{aligned} \frac{\alpha_i \chi^{riv}_i}{\chi^{riv}_{norm}} &= \frac{\Sigma^n_s [\alpha_i \chi^s_i]}{\Sigma^{k_{norm}}_{i_{norm}} \left[\alpha_{i_{norm}} \chi^{riv}_{i_{norm}} \right]} = \Sigma^n_s \left[\frac{\alpha_i \chi^s_i}{\Sigma^{k_{norm}}_{i_{norm}} \left[\Sigma^n_{s'} \left[\alpha_{i_{norm}} \chi^{s'}_{i_{norm}} \right] \right]} \right] \\ &= \Sigma^n_s \left[\left(\frac{\Sigma^{k_{norm}}_{i_{norm}} \left[\alpha_{i_{norm}} \chi^s_{i_{norm}} \right]}{\Sigma^n_{s'} \left[\Sigma^{k_{norm}}_{i_{norm}} \left[\alpha_{i_{norm}} \chi^{s'}_{i_{norm}} \right] \right]} \right) \left(\frac{\alpha_i \chi^s_i}{\Sigma^{k_{norm}}_{i_{norm}} \left[\alpha_{i_{norm}} \chi^s_{i_{norm}} \right]} \right) \right] = \Sigma^n_s \left[f^s_{norm} \left(\frac{\alpha_i \chi^s_i}{\chi^s_{norm}} \right) \right] \end{aligned} \tag{46}$$

MEANDIR can normalize river data to arbitrary sums of dissolved constituents in order to best fit the requirements of individual studies. As described below, a very general choice of normalization is the sum of χ_{Σ^+}, χ_{ALK}, and χ_{DIC}, as this normalization allows for quantification of most end-members of interest and can include arbitrary sources of weathering acids.

Normalization to $\chi_{\Sigma^+ + SO_4^{2-}}$ and $\chi_{\Sigma^+ + ALK}$.—Modeling FeS_2 oxidation as an independent end-member is untenable when normalizing with χ_{Na^+} or χ_{Σ^+} because FeS_2 oxidation alone does not generate cations (eq 47). For this reason, SO_4^{2-} from FeS_2 oxidation has previously been included in the chemical composition of weathering end-members as values of $\chi^s_{FeS_2\ SO_4^{2-}}$ (Torres and others, 2016). However, because FeS_2 oxidation is a source of SO_4^{2-} and a sink of ALK (eq 47), including $\chi_{SO_4^{2-}}$ or χ_{ALK} in χ_{norm} allows FeS_2 oxidation to be modeled as an end-member independent of weathering lithology. Examples of such normalizations are the sum of $\chi^s_{\Sigma^+}$ and $2\chi^s_{SO_4^{2-}}$ ($\chi^s_{\Sigma^+ + SO_4^{2-}}$; eq 48) or $\chi^s_{\Sigma^+}$ and χ^s_{ALK} ($\chi^s_{\Sigma^+ + ALK}$; eq 49).

$$\frac{1}{4}FeS_2 + \frac{15}{16}O_2 + \frac{1}{2}H_2O \rightarrow \frac{1}{2}SO_4^{2-} + H^+ + \frac{1}{8}Fe_2O_3 \tag{47}$$

$$\chi^s_{\Sigma^+ + SO_4^{2-}} = 2\chi^s_{Ca^{2+}} + 2\chi^s_{Mg^{2+}} + \chi^s_{Na^+} + \chi^s_{K^+} + 2\chi^s_{SO_4^{2-}} \tag{48}$$

$$\chi^s_{\Sigma^+ + ALK} = 2\chi^s_{Ca^{2+}} + 2\chi^s_{Mg^{2+}} + \chi^s_{Na^+} + \chi^s_{K^+} + \chi^s_{ALK} \tag{49}$$

When normalizing to $\chi_{\Sigma^+ + SO_4^{2-}}$, the end-member for FeS_2 oxidation has $2\chi^{FeS_2\ ox.}_{SO_4^{2-}}/\chi^{FeS_2\ ox.}_{\Sigma^+ + SO_4^{2-}} = 1$ and all normalized cation ratios equal to zero. Note that, in the expression $\chi^{FeS_2\ ox.}_{SO_4^{2-}}$, FeS_2 oxidation is now written as a superscript on χ to indicate its status as an end-member that sources SO_4^{2-} to the river. Assuming that the carbonate and silicate end-members do not contain structural SO_4^{2-} ($\chi^s_{SO_4^{2-}} = 0$), these end-members have $2\chi^s_{SO_4^{2-}}/\chi^s_{\Sigma^+ + SO_4^{2-}} = 0$ and the same cation ratios as when normalizing with χ_{Σ^+}: $2\chi^{slct}_{Ca^{2+}}/\chi^{slct}_{\Sigma^+ + SO_4^{2-}} = 2\chi^{slct}_{Ca^{2+}}/\chi^{slct}_{\Sigma^+}$. For end-members that source SO_4^{2-}, like evaporite or precipitation, cation ratios normalized with $\chi_{\Sigma^+ + SO_4^{2-}}$ are decreased relative to normalization by χ_{Σ^+} because $\chi^s_{SO_4^{2-}}$ is included in the denominator of the ratio: $2\chi^{evap}_{Ca^{2+}}/\chi^{evap}_{\Sigma^+ + SO_4^{2-}} < 2\chi^{evap}_{Ca^{2+}}/\chi^{evap}_{\Sigma^+}$ (table 4).

When normalizing to $\chi^s_{\Sigma^+ + ALK}$, FeS_2 oxidation has $2\chi^{FeS_2\ ox.}_{SO_4^{2-}}/\chi^{FeS_2\ ox.}_{\Sigma^+ + ALK} = -1$, $\chi^{FeS_2\ ox.}_{ALK}/\chi^{FeS_2\ ox.}_{\Sigma^+ + ALK} = 1$, and all other normalized non-isotopic ratios equal to zero. Similarly, because carbonate and silicate weathering source ALK, $2\chi^{carb}_{Ca^{2+}}/\chi^{carb}_{\Sigma^+ + ALK} < 2\chi^{carb}_{Ca^{2+}}/\chi^{carb}_{\Sigma^+}$ and $2\chi^{slct}_{Ca^{2+}}/\chi^{slct}_{\Sigma^+ + ALK} < 2\chi^{slct}_{Ca^{2+}}/\chi^{slct}_{\Sigma^+}$. The normalization with $\chi_{\Sigma^+ + ALK}$ is more general than normalization with $\chi_{\Sigma^+ + SO_4^{2-}}$ because it allows for representation of any acid source or sink. For example, a process such as NH_3 oxidation could not be directly modeled when $\chi_{norm} = \chi_{\Sigma^+ + SO_4^{2-}}$ because neither $\chi_{NO_3^-}$ nor χ_{ALK} are in the normalization variable. Conversely, NH_3 oxidation can be included in a model normalized to $\chi_{\Sigma^+ + ALK}$. Analogous to FeS_2 oxidation, the end-member for NH_3 oxidation would have $\chi^{NH_3\ ox.}_{NO_3^-}/\chi^{NH_3\ ox.}_{\Sigma^+ + ALK} = -1$, $\chi^{NH_3\ ox.}_{ALK}/\chi^{NH_3\ ox.}_{\Sigma^+ + ALK} = 1$, and all other non-isotopic normalized ratios equal to zero.

Normalization with $\chi_{\Sigma^+ + SO_4^{2-}}$ or $\chi_{\Sigma^+ + ALK}$ entails a constraint on the normalized ratios to achieve internal consistency (eqs 50 and 51). As in the case of $\chi_{norm} = \chi_{\Sigma^+}$, the requirement for internal consistency is satisfied by selecting a single ratio with a numerator constituent to the normalization variable to be solved using the other end-member selections.

TABLE 4

Example end-member ratios for normalization to χ_{Na^+}, χ_{Σ^+}, $\chi_{\Sigma^+ + ALK + DIC}$, *and* $\chi_{\Sigma^+ + SO_4^{2-} + DIC}$

-	Carbonate	Dolomite	Silicate	Evaporite	FeS_2 ox.	C_{org} ox.
Normalization with χ_{Na^+} (μM/μM)						
$\chi^s_{Ca^{2+}}$	-	-	0.30	0.375	-	-
$\chi^s_{Mg^{2+}}$	-	-	0.20	0.375	-	-
$\chi^s_{Na^+}$	-	-	1.00	1.00	-	-
$\chi^s_{SO_4^{2-}}$	-	-	0.00	0.75	-	-
$\chi^s_{Cl^-}$	-	-	0.00	1.00	-	-
χ^s_{ALK}	-	-	2.00	0.00	-	-
χ^s_{DIC}	-	-	0.00	0.00	-	-
Normalization with χ_{Σ^+} (eq/eq)						
$2\chi^s_{Ca^{2+}}$	1.00	0.50	0.30	0.30	-	-
$2\chi^s_{Mg^{2+}}$	0.00	0.50	0.20	0.30	-	-
$\chi^s_{Na^+}$	0.00	0.00	0.50	0.40	-	-
$2\chi^s_{SO_4^{2-}}$	0.00	0.00	0.00	0.60	-	-
$\chi^s_{Cl^-}$	0.00	0.00	0.00	0.40	-	-
χ^s_{ALK}	1.00	1.00	1.00	0.00	-	-
χ^s_{DIC}	0.50	0.50	0.00	0.00	-	-
Normalization with $\chi_{\Sigma^+ + ALK + DIC}$ (eq/eq)						
$2\chi^s_{Ca^{2+}}$	0.40	0.20	0.15	0.30	0.00	0.00
$2\chi^s_{Mg^{2+}}$	0.00	0.20	0.10	0.30	0.00	0.00
$\chi^s_{Na^+}$	0.00	0.00	0.25	0.40	0.00	0.00
$2\chi^s_{SO_4^{2-}}$	0.00	0.00	0.00	0.60	-1.00	0.00
$\chi^s_{Cl^-}$	0.00	0.00	0.00	0.40	0.00	0.00
χ^s_{ALK}	0.40	0.40	0.50	0.00	1.00	0.00
χ^s_{DIC}	0.20	0.20	0.00	0.00	0.00	1.00
Normalization with $\chi_{\Sigma^+ + SO_4^{2-} + DIC}$ (eq/eq)						
$2\chi^s_{Ca^{2+}}$	0.66	0.33	0.30	0.1875	0.00	0.00
$2\chi^s_{Mg^{2+}}$	0.00	0.33	0.20	0.1875	0.00	0.00
$\chi^s_{Na^+}$	0.00	0.00	0.50	0.25	0.00	0.00
$2\chi^s_{SO_4^{2-}}$	0.00	0.00	0.00	0.375	1.00	0.00
$\chi^s_{Cl^-}$	0.00	0.00	0.00	0.25	0.00	0.00
χ^s_{ALK}	0.66	0.66	1.00	0.00	-1.00	0.00
χ^s_{DIC}	0.33	0.33	0.00	0.00	0.00	1.00

All normalized ratios are given for the same arbitrary, but realistic, carbonate, dolomite, silicate and evaporite end-members. Note that $\chi^{evap}_{SO_4^{2-}} = \chi^{evap}_{Ca^{2+}} + \chi^{evap}_{Mg^{2+}}$ and $\chi^{evap}_{Cl^-} = \chi^{evap}_{Na^+}$. See tables 7, 9, 11, and 13 for the end-member ratios used in the scenarios discussed in the text.

$$1 = \frac{2\chi^{s}_{Ca^{2+}}}{\chi^{s}_{\Sigma^{+}+SO_4^{2-}}} + \frac{2\chi^{s}_{Mg^{2+}}}{\chi^{s}_{\Sigma^{+}+SO_4^{2-}}} + \frac{\chi^{s}_{Na^{+}}}{\chi^{s}_{\Sigma^{+}+SO_4^{2-}}} + \frac{\chi^{s}_{K^{+}}}{\chi^{s}_{\Sigma^{+}+SO_4^{2-}}} + \frac{2\chi^{s}_{SO_4^{2-}}}{\chi^{s}_{\Sigma^{+}+SO_4^{2-}}} \quad (50)$$

$$1 = \frac{2\chi^{s}_{Ca^{2+}}}{\chi^{s}_{\Sigma^{+}+ALK}} + \frac{2\chi^{s}_{Mg^{2+}}}{\chi^{s}_{\Sigma^{+}+ALK}} + \frac{\chi^{s}_{Na^{+}}}{\chi^{s}_{\Sigma^{+}+ALK}} + \frac{\chi^{s}_{K^{+}}}{\chi^{s}_{\Sigma^{+}+ALK}} + \frac{\chi^{s}_{ALK}}{\chi^{s}_{\Sigma^{+}+ALK}} \quad (51)$$

The preceding discussion focused on explicitly representing FeS_2 oxidation as an independent end-member during river inversion. However, the same equations can be used to represent any external source of $\chi^{riv}_{SO_4^{2-}}$, including inputs of SO_4^{2-} from anthropogenic pollution or from the biosphere. An independent end-member sourcing $\chi^{riv}_{SO_4^{2-}}$ not attributable to evaporites or precipitation functions very similarly to excess SO_4^{2-} (Burke and others, 2018). To distinguish the quantification of $\chi^{riv}_{excess\ SO_4^{2-}}$, where $\chi^{riv}_{SO_4^{2-}}$ is not included in the inversion, from an independent SO_4^{2-}-bearing end-member, where $\chi^{riv}_{SO_4^{2-}}$ is included in the inversion, we call the latter "other SO_4^{2-}". Because such "other SO_4^{2-}" derives from the "other" end-member, moles of other SO_4^{2-} are indicated in our notation as $\chi^{other}_{SO_4^{2-}}$; note the superscript for "other" in contrast to the subscript for "excess SO_4^{2-}", marking the former as an end-member in the inversion. An advantage of quantifying $\chi^{other}_{SO_4^{2-}}$ rather than $\chi^{riv}_{excess\ SO_4^{2-}}$ is that, while $\chi^{riv}_{excess\ SO_4^{2-}}$ can attain negative values, $\chi^{other}_{SO_4^{2-}}$ can be constrained to have a minimum value of zero by setting limits on the contribution of the "other" end-member.

As with the quantification of $\chi^{riv}_{excess\ SO_4^{2-}}$, the $\delta^{34}S$ of $\chi^{other}_{SO_4^{2-}}$ can be calculated from inversion results. For each successful simulation result, MEANDIR calculates a range of possible values for ${}^{34}R^{other}_{SO_4^{2-}}$ based on possible values for ${}^{34}R^{s}_{SO_4^{2-}}$ (eq 52). That is, when $\delta^{34}S$ is not explicitly included in the inversion, the possible $\delta^{34}S$ ranges for all end-members can be accounted for by performing a second Monte Carlo simulation on each successful set of $\chi^{s_{SO_4^{2-}}}_{SO_4^{2-}}$ values.

$${}^{34}R^{other}_{SO_4^{2-}} = \frac{\left(\chi^{riv}_{SO_4^{2-}} \cdot {}^{34}R^{riv}_{SO_4^{2-}}\right) - \Sigma^{n_{SO_4^{2-}}}_{s_{SO_4^{2-}}}\left[\chi^{s_{SO_4^{2-}}}_{SO_4^{2-}} \cdot {}^{34}R^{s_{SO_4^{2-}}}_{SO_4^{2-}}\right]}{\chi^{other}_{SO_4^{2-}}} \quad (52)$$

Normalization to $\chi_{\Sigma^{+}+DIC}$.—The oxidation of petrogenic organic carbon has an important role in chemical weathering budgets (Bolton and others, 2006; Bouchez and others, 2010; Horan and others, 2019; Hilton and West, 2020). Including C_{org} oxidation in inversion models allows for quantification of DIC impacts from C_{org} oxidation which, along with quantification of ALK sinks from FeS_2 oxidation and sources from chemical weathering, enables assessing the influence of weathering systems on atmospheric CO_2. Including C_{org} oxidation in inversion models would be beneficial when employing tracers like ${}^{13}R^{riv}_{DIC}$ or χ^{riv}_{Re} as these variables are influenced by weathering of multiple lithologies in addition to C_{org} oxidation (Horan and others, 2019). However, there has been limited success in representing petrogenic organic carbon oxidation directly in river inversion models. Like FeS_2 oxidation, the lack of prior

explicit C_{org} representation partially reflects that the oxidation of C_{org} does not source cations to river water, and cannot be included as an independent end-member when normalizing to χ_{Na^+} or χ_{Σ^+} (eq 53). Instead, including χ_{DIC} in χ_{norm} enables the direct representation of C_{org} oxidation. One such example is the sum of $\chi^s_{\Sigma^+}$ and χ^s_{DIC} ($\chi^s_{\Sigma^+ + DIC}$; eqs 54 and 55).

$$CH_2O + O_2 \rightarrow H_2CO_3 \tag{53}$$

$$\chi^s_{\Sigma^+ + DIC} = 2\chi^s_{Ca^{2+}} + 2\chi^s_{Mg^{2+}} + \chi^s_{Na^+} + \chi^s_{K^+} + \chi^s_{DIC} \tag{54}$$

$$1 = \frac{2\chi^s_{Ca^{2+}}}{\chi^s_{\Sigma^+ + DIC}} + \frac{2\chi^s_{Mg^{2+}}}{\chi^s_{\Sigma^+ + DIC}} + \frac{\chi^s_{Na^+}}{\chi^s_{\Sigma^+ + DIC}} + \frac{\chi^s_{K^+}}{\chi^s_{\Sigma^+ + DIC}} + \frac{\chi^s_{DIC}}{\chi^s_{\Sigma^+ + DIC}} \tag{55}$$

Setting $\chi_{norm} = \chi_{\Sigma^+ + DIC}$ also enables representation of CO_2 exchange between the river and atmosphere. By allowing end-members for atmospheric CO_2 or C_{org} oxidation to have either positive or negative fractional contributions to $\chi^{riv}_{\Sigma^+ + DIC}$, MEANDIR allows the former process to represent net gas exchange across the river/atmosphere boundary and the latter process to represent net uptake or release of DIC through oxidation or fixation of organic carbon. Because the end-members for both C_{org} oxidation and atmospheric CO_2 have $\chi^s_{DIC}/\chi^s_{\Sigma^+ + DIC} = 1$ and all dissolved cations ratios equal to zero, distinguishing their relative influence on river water requires characteristic values for $^{13}R^s_{DIC}$, $^{14}R^s_{DIC}$, or trace metal ratios. Silicate weathering has $\chi^{slct}_{DIC}/\chi^{slct}_{\Sigma^+ + DIC} = 0$, while carbonate weathering has $\chi^{carb}_{DIC}/\chi^{carb}_{\Sigma^+ + DIC} = 1/3$ as it sources 1 mole of DIC per two charge-equivalent moles of cations (table 4).

The preceding discussion highlights the utility of including χ_{Σ^+}, χ_{ALK}, and χ_{DIC} in χ_{norm}. Inclusion of χ_{Σ^+} enables representation of end-members such as evaporites that only source conservative ions, inclusion of χ_{ALK} allows representation of end-members such as FeS_2 oxidation that alter χ^{riv}_{ALK}, and inclusion of χ_{DIC} allow representation of end-members such as C_{org} oxidation that alter χ^{riv}_{DIC}. A highly generic choice of normalization variable is thus the sum of χ_{Σ^+}, χ_{ALK}, and χ_{DIC} ($\chi^s_{\Sigma^+ + ALK + DIC}$; eq 56), with an associated normalization constraint (eq 57). Below, we use this normalization with the data of Horan and others (2019) to simultaneously constrain the fraction of $\chi^{riv}_{SO_4^{2-}}$ derived from FeS_2 oxidation and χ^{riv}_{DIC} derived from petrogenic C_{org} oxidation.

$$\chi^s_{\Sigma^+ + ALK + DIC} = 2\chi^s_{Ca^{2+}} + 2\chi^s_{Mg^{2+}} + \chi^s_{Na^+} + \chi^s_{K^+} + \chi^s_{ALK} + \chi^s_{DIC} \tag{56}$$

$$1 = \frac{2\chi^s_{Ca^{2+}}}{\chi^s_{\Sigma^+ + ALK + DIC}} + \frac{2\chi^s_{Mg^{2+}}}{\chi^s_{\Sigma^+ + ALK + DIC}} + \frac{\chi^s_{Na^+}}{\chi^s_{\Sigma^+ + ALK + DIC}} + \frac{\chi^s_{K^+}}{\chi^s_{\Sigma^+ + ALK + DIC}} + \frac{\chi^s_{ALK}}{\chi^s_{\Sigma^+ + ALK + DIC}} + \frac{\chi^s_{DIC}}{\chi^s_{\Sigma^+ + ALK + DIC}} \tag{57}$$

Charge balance when normalizing to sums of dissolved variables.—An additional constraint from charge balance occurs when all cations and anions are explicitly included in the inversion model. Practically, this would occur when all major conservative cations and anions are measured and either $\chi^s_{HCO_3^-}$ or χ^s_{ALK} is included in the inversion (eq 58). Each term in the charge balance equation can then be normalized (eq 59), and a specific equation for charge balance found by substitution and simplification

using the internal consistency of end-members (eqs 60–63). In MEANDIR, these equations are solved by selecting one ratio with numerator constituent to the normalization and one ratio with numerator external to the normalization to calculate using the other ratios drawn from user-defined distributions.

$$2\chi^{s}_{Ca^{2+}} + 2\chi^{s}_{Mg^{2+}} + \chi^{s}_{Na^{+}} + \chi^{s}_{K^{+}} = 2\chi^{s}_{SO_4^{2-}} + \chi^{s}_{Cl^{-}} + \chi^{s}_{ALK} \tag{58}$$

$$\left(\frac{2\chi^{s}_{Ca^{2+}}}{\chi^{s}_{norm}} + \frac{2\chi^{s}_{Mg^{2+}}}{\chi^{s}_{norm}} + \frac{\chi^{s}_{Na^{+}}}{\chi^{s}_{norm}} + \frac{\chi^{s}_{K^{+}}}{\chi^{s}_{norm}}\right) = \left(\frac{2\chi^{s}_{SO_4^{2-}}}{\chi^{s}_{norm}} + \frac{\chi^{s}_{Cl^{-}}}{\chi^{s}_{norm}} + \frac{\chi^{s}_{ALK}}{\chi^{s}_{norm}}\right) \tag{59}$$

$$\begin{aligned}\left(\frac{2\chi^{s}_{Ca^{2+}}}{\chi^{s}_{\Sigma^{+}+SO_4^{2-}}} + \frac{2\chi^{s}_{Mg^{2+}}}{\chi^{s}_{\Sigma^{+}+SO_4^{2-}}} + \frac{\chi^{s}_{Na^{+}}}{\chi^{s}_{\Sigma^{+}+SO_4^{2-}}} + \frac{\chi^{s}_{K^{+}}}{\chi^{s}_{\Sigma^{+}+SO_4^{2-}}} + \frac{2\chi^{s}_{SO_4^{2-}}}{\chi^{s}_{\Sigma^{+}+SO_4^{2-}}}\right) \\ = \left(2\left(\frac{2\chi^{s}_{SO_4^{2-}}}{\chi^{s}_{\Sigma^{+}+SO_4^{2-}}}\right) + \frac{\chi^{s}_{Cl^{-}}}{\chi^{s}_{\Sigma^{+}+SO_4^{2-}}} + \frac{\chi^{s}_{ALK}}{\chi^{s}_{\Sigma^{+}+SO_4^{2-}}}\right) = 1\end{aligned} \tag{60}$$

$$\begin{aligned}\left(\frac{2\chi^{s}_{Ca^{2+}}}{\chi^{s}_{\Sigma^{+}+ALK}} + \frac{2\chi^{s}_{Mg^{2+}}}{\chi^{s}_{\Sigma^{+}+ALK}} + \frac{\chi^{s}_{Na^{+}}}{\chi^{s}_{\Sigma^{+}+ALK}} + \frac{\chi^{s}_{K^{+}}}{\chi^{s}_{\Sigma^{+}+ALK}} + \frac{\chi^{s}_{ALK}}{\chi^{s}_{\Sigma^{+}+ALK}}\right) \\ = \left(\frac{2\chi^{s}_{SO_4^{2-}}}{\chi^{s}_{\Sigma^{+}+ALK}} + \frac{\chi^{s}_{Cl^{-}}}{\chi^{s}_{\Sigma^{+}+ALK}} + 2\left(\frac{\chi^{s}_{ALK}}{\chi^{s}_{\Sigma^{+}+ALK}}\right)\right) = 1\end{aligned} \tag{61}$$

$$\begin{aligned}\left(\frac{2\chi^{s}_{Ca^{2+}}}{\chi^{s}_{\Sigma^{+}+DIC}} + \frac{2\chi^{s}_{Mg^{2+}}}{\chi^{s}_{\Sigma^{+}+DIC}} + \frac{\chi^{s}_{Na^{+}}}{\chi^{s}_{\Sigma^{+}+DIC}} + \frac{\chi^{s}_{K^{+}}}{\chi^{s}_{\Sigma^{+}+DIC}} + \frac{\chi^{s}_{DIC}}{\chi^{s}_{\Sigma^{+}+DIC}}\right) \\ = \left(\frac{2\chi^{s}_{SO_4^{2-}}}{\chi^{s}_{\Sigma^{+}+DIC}} + \frac{\chi^{s}_{Cl^{-}}}{\chi^{s}_{\Sigma^{+}+DIC}} + \frac{\chi^{s}_{ALK}}{\chi^{s}_{\Sigma^{+}+DIC}} + \frac{\chi^{s}_{DIC}}{\chi^{s}_{\Sigma^{+}+DIC}}\right) = 1\end{aligned} \tag{62}$$

$$\begin{aligned}\left(\frac{2\chi^{s}_{Ca^{2+}}}{\chi^{s}_{\Sigma^{+}+ALK+DIC}} + \frac{2\chi^{s}_{Mg^{2+}}}{\chi^{s}_{\Sigma^{+}+ALK+DIC}} + \frac{\chi^{s}_{Na^{+}}}{\chi^{s}_{\Sigma^{+}+ALK+DIC}} + \frac{\chi^{s}_{K^{+}}}{\chi^{s}_{\Sigma^{+}+ALK+DIC}} + \frac{\chi^{s}_{ALK}}{\chi^{s}_{\Sigma^{+}+ALK+DIC}} + \frac{\chi^{s}_{DIC}}{\chi^{s}_{\Sigma^{+}+ALK+DIC}}\right) \\ = \left(\frac{2\chi^{s}_{SO_4^{2-}}}{\chi^{s}_{\Sigma^{+}+ALK+DIC}} + \frac{\chi^{s}_{Cl^{-}}}{\chi^{s}_{\Sigma^{+}+ALK+DIC}} + 2\left(\frac{\chi^{s}_{ALK}}{\chi^{s}_{\Sigma^{+}+ALK+DIC}}\right) + \frac{\chi^{s}_{DIC}}{\chi^{s}_{\Sigma^{+}+ALK+DIC}}\right) = 1\end{aligned} \tag{63}$$

Calculation of R, Z, Y, W, and *C*

Definition of R, Z, Y, W, C and calculation of χ_{ALK}/χ_{DIC}.—Prior work has quantified the impact of chemical weathering on the global carbon cycle by considering the relative fractions of carbonate weathering (R) and sulfuric acid weathering (Z) (Torres and others, 2016). Below, we update the formalism of Torres and others (2016) to define a variable C that reflects the net effect of organic carbon production and oxidation. We also define the variable Y to represent the fraction of $\chi^{riv}_{SO_4^{2-}}$ sourced from FeS_2 oxidation and the variable W to represent the ratio of $\chi^{riv}_{SO_4^{2-}}$ sourced from FeS_2 oxidation relative to χ^{riv}_{norm}. Variables Y and W have previously been used without formal definition (Torres and others, 2016; Kemeny and others, 2021a). We note that defining the carbonate weathering fraction with the variable R is the second definition of R, which is defined earlier in this text as an isotopic ratio (table 2).

Unfortunately, the symbol R is already established as representing both isotopic ratios and carbonate weathering fraction. Although not ideal, the two uses of R are generally distinguishable by context.

The weathering of carbonate and silicate rock can be written as generic H^+ consuming reactions (eqs 41 and 43), while H^+ for weathering can be sourced from H_2SO_4 following FeS_2 oxidation (eq 47). Similarly, carbonate weathering and C_{org} oxidation source DIC (eq 53). To represent the net effect of chemical weathering in a river catchment, we consider the weighted sums of carbonate weathering, silicate weathering, FeS_2 oxidation, and net C_{org} oxidation (eq 64). The variables ϕ and β are taken to represent the alkalinity released by carbonate weathering and silicate weathering, respectively, the variable γ is taken to represent the alkalinity consumed through FeS_2 oxidation, and the variable θ is taken to represent the DIC released through net C_{org} oxidation (eq 64; table 2). Because the aggregate chemical weathering reaction is written at the carbonic acid equivalence point, the net effect of the reaction on ALK is the factor on H^+ $(\phi + \beta - \gamma)$ and the net effect on DIC is the factor on H_2CO_3 $(\frac{1}{2}\phi + \theta)$ (eq 64).

$$(\phi + \beta - \gamma)H^+ + \left(\frac{1}{2}\phi\right)CaCO_3 + \left(\frac{1}{2}\beta\right)CaSiO_3 + \left(\frac{1}{4}\gamma\right)FeS_2 + \left(\frac{15}{16}\gamma + \theta\right)O_2 + (\theta)CH_2O + \left(\frac{1}{2}\gamma - \frac{1}{2}\beta\right)H_2O \rightarrow \left(\frac{1}{2}\phi + \frac{1}{2}\beta\right)Ca^{2+} + \left(\frac{1}{2}\phi + \theta\right)H_2CO_3 + \left(\frac{1}{2}\beta\right)SiO_2 + \left(\frac{1}{2}\gamma\right)SO_4^{2-} + \left(\frac{1}{8}\gamma\right)Fe_2O_3 \quad (64)$$

The condition $\theta < 0$ is a possible scenario reflecting net biomass generation in excess of organic carbon oxidation. However, given that biospheric C_{org} is typically exported as a solid phase, quantifying the overall θ value for a watershed system may be complicated as solutes and particulates obey different concentration-discharge relationships (Torres and others, 2015; Turowski and others, 2016), biospheric C_{org} export may be highly episodic (West and others, 2011), and biospheric C_{org} fluxes are rapidly degraded in downstream settings such as floodplains (Scheingross and others, 2021) and near-shore marine environments (Blair and Aller, 2012). As MEANDIR focuses on solutes, in this work we limit our use of θ to chemical weathering processes. This approach captures useful information on offsets in silicate weathering due to petrogenic organic carbon oxidation but does not capture every terrestrial process that affects atmospheric pCO_2.

We define the variable R as the ratio of alkalinity released during carbonate weathering to alkalinity released during carbonate and silicate weathering (eq 65). We define the variable Z as the ratio of alkalinity consumed during sulfide oxidation relative to alkalinity released during carbonate and silicate weathering (eq 66). We define the variable C as DIC released during oxidation of organic matter relative to alkalinity released during carbonate and silicate weathering (eq 67). The normalization for C is chosen to match the normalization of R and Z. Although alternative choices for the normalization of C are possible, the normalization matching R and Z is useful. With these definitions, the net χ_{ALK}/χ_{DIC} of a weathering system is a simple function of R, Z, and C (eq 68). At a non-zero value of χ_{ALK}/χ_{DIC} the variables R, Z, and C form the plane $1/\left(\frac{\chi_{ALK}}{\chi_{DIC}}\right) = R/2 + Z/\left(\frac{\chi_{ALK}}{\chi_{DIC}}\right) + C$. That is, accounting for organic carbon oxidation alters the relationships among R, Z, and χ_{ALK}/χ_{DIC} that were established in Torres and others (2016).

$$R = \frac{\phi}{\phi + \beta} \tag{65}$$

$$Z = \frac{\gamma}{\phi + \beta} \tag{66}$$

$$C = \frac{\theta}{\phi + \beta} \tag{67}$$

$$\frac{\chi_{ALK}}{\chi_{DIC}} = \frac{(\phi + \beta - \gamma)}{\left(\frac{1}{2}\phi + \theta\right)} = \frac{\frac{(\phi + \beta - \gamma)}{(\phi + \beta)}}{\frac{\left(\frac{1}{2}\phi + \theta\right)}{\phi + \beta}} = \frac{2(1 - Z)}{R + 2C} \tag{68}$$

Calculating R, Z, Y, W, and C from inversion results.—The carbonate weathering fraction R can be calculated in several ways. First, when χ^{riv}_{ALK} is included in the inversion, R is equal to the ratio of ALK from carbonate weathering to ALK from carbonate and silicate weathering (R_{ALK}; eq 69, where s_{carb} indexes the list of length n_{carb} containing all carbonate end-member, and s_{weath} indexes the list of length n_{weath} containing all weathering end-members). R is also calculated as the charge-equivalent cation contributions of carbonate end-members relative to the sum of charge-equivalent contributions from all weathering end-members ($R_{i_{RZC}\ldots k_{RZC}}$; eq 70, where i_{RZC} indexes the list of length k_{RZC} containing the cations used to calculate the denominators of R, Z, and C, and $\alpha_{i_{RZC}}$ is the charge of the relevant variable). We use the subscript $i_{RZC} \ldots k_{RZC}$ on R to indicate which observations are in the calculation; as discussed below, this is in response to disagreement regarding whether χ_{Na^+} and χ_{K^+} should be included in R, and thus whether the denominator of R reflects the total alkalinity released from all carbonate and silicate sources. As argued below, it is our opinion that the list indexed by i_{RZC} should generally include all cations sourced to the river from weathering, including χ_{Na^+} and χ_{K^+}.

$$R_{ALK} = \frac{\Sigma^{n_{carb}}_{s_{carb}}\left[\chi^{s_{carb}}_{ALK}\right]}{\Sigma^{n_{weath}}_{s_{weath}}\left[\chi^{s_{weath}}_{ALK}\right]} \tag{69}$$

$$R_{i_{RZC}\ldots k_{RZC}} = \frac{\Sigma^{n_{carb}}_{s_{carb}}\left[\Sigma^{k_{RZC}}_{i_{RZC}}\left[\alpha_{i_{RZC}}\chi^{s_{carb}}_{i_{RZC}}\right]\right]}{\Sigma^{n_{weath}}_{s_{weath}}\left[\Sigma^{k_{RZC}}_{i_{RZC}}\left[\alpha_{i_{RZC}}\chi^{s_{weath}}_{i_{RZC}}\right]\right]} \tag{70}$$

Examples of R_{ALK} (eqs 71) and $R_{i_{RZC}\ldots k_{RZC}}$ (eqs 72 and 73) are given for an inversion including χ_{ALK}, $\chi_{Ca^{2+}}$, $\chi_{Mg^{2+}}$, χ_{Na^+}, and χ_{Cl^-} with four end-members: calcite (calc), dolomite (dolo), silicate (slct), and precipitation (prec). Only $\chi_{Ca^{2+}}$ and $\chi_{Mg^{2+}}$ contribute to R in equation (72) ($R_{Ca,\ Mg}$), while in equation (73) the calculation also includes χ_{Na^+} ($R_{Ca,\ Mg,\ Na}$).

$$R_{ALK} = \frac{\chi^{calc}_{ALK} + \chi^{dolo}_{ALK}}{\chi^{calc}_{ALK} + \chi^{dolo}_{ALK} + \chi^{slct}_{ALK}} \tag{71}$$

$$R_{Ca,\ Mg} = \frac{2\chi^{calc}_{Ca^{2+}} + 2\chi^{dolo}_{Ca^{2+}} + 2\chi^{dolo}_{Mg^{2+}}}{2\chi^{calc}_{Ca^{2+}} + 2\chi^{dolo}_{Ca^{2+}} + 2\chi^{dolo}_{Mg^{2+}} + 2\chi^{slct}_{Ca^{2+}} + 2\chi^{slct}_{Mg^{2+}}} \tag{72}$$

$$R_{Ca,\ Mg,\ Na} = \frac{2\chi^{calc}_{Ca^{2+}} + 2\chi^{dolo}_{Ca^{2+}} + 2\chi^{dolo}_{Mg^{2+}}}{2\chi^{calc}_{Ca^{2+}} + 2\chi^{dolo}_{Ca^{2+}} + 2\chi^{dolo}_{Mg^{2+}} + 2\chi^{slct}_{Ca^{2+}} + 2\chi^{slct}_{Mg^{2+}} + \chi^{slct}_{Na^{+}}} \tag{73}$$

Calculation of the sulfuric acid weathering fraction Z depends on how FeS_2 oxidation is represented. When FeS_2 is treated as a stand-alone end-member, Z can be calculated as the alkalinity consumed during FeS_2 oxidation relative to alkalinity released during chemical weathering ($Z^{FeS_2\ ox.\ ALK}_{ALK}$; eq 74) or as the charge-equivalent $\chi^{FeS_2\ ox.}_{SO_4^{2-}}$ relative to cations sourced from weathering end-members ($Z^{FeS_2\ ox.\ SO_4^{2-}}_{i_{RZC}\ldots k_{RZC}}$; eq 75). When attributing $\chi^{riv}_{excess\ SO_4^{2-}}$ to FeS_2 oxidation, Z is the charge-equivalent ratio of $\chi^{riv}_{excess\ SO_4^{2-}}$ to the charge-equivalent sum of cation contributions from all weathering end-members ($Z^{excess\ SO_4^{2-}}_{i_{RZC}\ldots k_{RZC}}$; eq 76). When values of $\chi^{s}_{FeS_2\ SO_4^{2-}}$ are constrained, Z is calculated as the ratio of the sum of FeS_2-derived SO_4^{2-} contributions relative to cations sourced from weathering end-members ($Z^{FeS_2\ SO_4^{2-}}_{i_{RZC}\ldots k_{RZC}}$; eq 77, where $s_{FeS_2\ SO_4^{2-}}$ indexes the list of length $n_{FeS_2\ SO_4^{2-}}$ containing end-members weathered by H_2SO_4).

$$Z^{FeS_2\ ox.\ ALK}_{ALK} = \frac{-\chi^{FeS_2\ ox.}_{ALK}}{\sum^{n_{weath}}_{s_{weath}}\left[\chi^{s_{weath}}_{ALK}\right]} \tag{74}$$

$$Z^{FeS_2\ ox.\ SO_4^{2-}}_{i_{RZC}\ldots k_{RZC}} = \frac{2\chi^{FeS_2\ ox.}_{SO_4^{2-}}}{\sum^{n_{weath}}_{s_{weath}}\left[\sum^{k_{RZC}}_{i_{RZC}}\left[\alpha_{i_{RZC}}\chi^{s_{weath}}_{i_{RZC}}\right]\right]} \tag{75}$$

$$Z^{excess\ SO_4^{2-}}_{i_{RZC}\ldots k_{RZC}} = \frac{2\chi^{riv}_{excess\ SO_4^{2-}}}{\sum^{n_{weath}}_{s_{weath}}\left[\sum^{k_{RZC}}_{i_{RZC}}\left[\alpha_{i_{RZC}}\chi^{s_{weath}}_{i_{RZC}}\right]\right]} \tag{76}$$

$$Z^{FeS_2\ SO_4^{2-}}_{i_{RZC}\ldots k_{RZC}} = \frac{\sum^{n_{FeS_2\ SO_4^{2-}}}_{s_{FeS_2\ SO_4^{2-}}}\left[2\chi^{s_{FeS_2\ SO_4^{2-}}}_{FeS_2\ SO_4^{2-}}\right]}{\sum^{n_{weath}}_{s_{weath}}\left[\sum^{k_{RZC}}_{i_{RZC}}\left[\alpha_{i_{RZC}}\chi^{s_{weath}}_{i_{RZC}}\right]\right]} \tag{77}$$

For the example given above but also including SO_4^{2-} and FeS_2 oxidation, the sulfuric acid weathering fraction is given for inversions when FeS_2 is explicitly included as an end-member in the inversion (eqs 78 and 79) or when quantifying FeS_2 oxidation with $\chi^{riv}_{excess\ SO_4^{2-}}$ (eq 80) or with $\chi^{s}_{FeS_2\ SO_4^{2-}}$ values (eq 81).

$$Z^{FeS_2\ ox.\ ALK}_{ALK} = \frac{-\chi^{FeS_2\ ox.}_{ALK}}{\chi^{carb}_{ALK} + \chi^{dolo}_{ALK} + \chi^{slct}_{ALK}} \tag{78}$$

$$Z^{FeS_2\ ox.\ SO_4^{2-}}_{Ca,\ Mg,\ Na} = \frac{2\chi^{FeS_2\ ox.}_{SO_4^{2-}}}{2\chi^{calc}_{Ca^{2+}} + 2\chi^{dolo}_{Ca^{2+}} + 2\chi^{dolo}_{Mg^{2+}} + 2\chi^{slct}_{Ca^{2+}} + 2\chi^{slct}_{Mg^{2+}} + \chi^{slct}_{Na^{+}}} \tag{79}$$

$$Z^{\text{excess } SO_4^{2-}}_{\text{Ca, Mg, Na}} = \frac{2\chi^{\text{riv}}_{\text{excess } SO_4^{2-}}}{2\chi^{\text{calc}}_{Ca^{2+}} + 2\chi^{\text{dolo}}_{Ca^{2+}} + 2\chi^{\text{dolo}}_{Mg^{2+}} + 2\chi^{\text{slct}}_{Ca^{2+}} + 2\chi^{\text{slct}}_{Mg^{2+}} + \chi^{\text{slct}}_{Na^{+}}} \tag{80}$$

$$Z^{FeS_2\ SO_4^{2-}}_{\text{Ca, Mg, Na}} = \frac{2\chi^{\text{carb}}_{FeS_2\ SO_4^{2-}} + 2\chi^{\text{dolo}}_{FeS_2\ SO_4^{2-}} + 2\chi^{\text{slct}}_{FeS_2\ SO_4^{2-}}}{2\chi^{\text{calc}}_{Ca^{2+}} + 2\chi^{\text{dolo}}_{Ca^{2+}} + 2\chi^{\text{dolo}}_{Mg^{2+}} + 2\chi^{\text{slct}}_{Ca^{2+}} + 2\chi^{\text{slct}}_{Mg^{2+}} + \chi^{\text{slct}}_{Na^{+}}} \tag{81}$$

Two variables related to Z are the charge-equivalent ratio of FeS_2-derived SO_4^{2-} to $\chi^{\text{riv}}_{SO_4^{2-}}$ (eqs 82–85) and to $\chi^{\text{riv}}_{\text{norm}}$ (eqs 86–89), which we define as Y and W, respectively. These ratios have been used in prior publications to evaluate the importance of FeS_2 oxidation relative to dissolved SO_4^{2-} and the sum of cations (Torres and others, 2016; Kemeny and others, 2021a) and are reported among the results of MEANDIR.

$$Y^{FeS_2 \text{ ox. ALK}} = \frac{-\chi^{FeS_2 \text{ ox.}}_{\text{ALK}}}{2\chi^{\text{riv}}_{SO_4^{2-}}} \tag{82}$$

$$Y^{FeS_2 \text{ ox. } SO_4^{2-}} = \frac{\chi^{FeS_2 \text{ ox.}}_{SO_4^{2-}}}{\chi^{\text{riv}}_{SO_4^{2-}}} \tag{83}$$

$$Y^{\text{excess } SO_4^{2-}} = \frac{\chi^{\text{riv}}_{\text{excess } SO_4^{2-}}}{\chi^{\text{riv}}_{SO_4^{2-}}} \tag{84}$$

$$Y^{FeS_2\ SO_4^{2-}} = \frac{\Sigma^{n_{FeS_2\ SO_4^{2-}}}_{s_{FeS_2\ SO_4^{2-}}} \left[{}^{s_{FeS_2\ SO_4^{2-}}}\chi_{FeS_2\ SO_4^{2-}} \right]}{\chi^{\text{riv}}_{SO_4^{2-}}} \tag{85}$$

$$W^{FeS_2 \text{ ox. ALK}} = \frac{-\chi^{FeS_2 \text{ ox.}}_{\text{ALK}}}{\chi^{\text{riv}}_{\text{norm}}} \tag{86}$$

$$W^{FeS_2 \text{ ox. } SO_4^{2-}} = \frac{2\chi^{FeS_2 \text{ ox.}}_{SO_4^{2-}}}{\chi^{\text{riv}}_{\text{norm}}} \tag{87}$$

$$W^{\text{excess } SO_4^{2-}} = \frac{2\chi^{\text{riv}}_{\text{excess } SO_4^{2-}}}{\chi^{\text{riv}}_{\text{norm}}} \tag{88}$$

$$W^{FeS_2\ SO_4^{2-}} = \frac{\Sigma^{n_{FeS_2\ SO_4^{2-}}}_{s_{FeS_2\ SO_4^{2-}}} \left[2\,{}^{s_{FeS_2\ SO_4^{2-}}}\chi_{FeS_2\ SO_4^{2-}} \right]}{\chi^{\text{riv}}_{\text{norm}}} \tag{89}$$

When C_{org} oxidation is treated as a stand-alone end-member, the organic carbon weathering fraction C is calculated as $\chi^{C_{org} \text{ ox.}}_{\text{DIC}}$ relative to charge-equivalent cations sourced from weathering end-members (eqs 90 and 91).

$$C_{i_{RZC}\ldots k_{RZC}} = \frac{\chi_{DIC}^{C_{org}\ ox.}}{\Sigma_{s_{weath}}^{n_{weath}}\left[\Sigma_{i_{RZC}}^{k_{RZC}}\left[\alpha_{i_{RZC}}\chi_{i_{RZC}}^{s_{weath}}\right]\right]} \tag{90}$$

$$C_{Ca,\ Mg,\ Na} = \frac{\chi_{DIC}^{C_{org}\ ox.}}{2\chi_{Ca^{2+}}^{carb} + 2\chi_{Ca^{2+}}^{dolo} + 2\chi_{Mg^{2+}}^{dolo} + 2\chi_{Ca^{2+}}^{slct} + 2\chi_{Mg^{2+}}^{slct} + \chi_{Na^{+}}^{slct}} \tag{91}$$

R, Z, Y, W, and C values accounting for secondary phase formation.—The formation of secondary phases removes solutes from river water and reduces each term in the summations that underlie calculation of R, Z, Y, W, and C. In the presence of secondary phases, we thus need to distinguish between gross (^{g}R, ^{g}Z, ^{g}C) and net (^{n}R, ^{n}Z, ^{n}C) weathering variables, both of which are reported in the results of MEANDIR. To calculate the net weathering parameters, we assume that the formation of secondary phases removes solutes in proportion to the fraction in which they are sourced from primary end-members.

As an example, consider a case where a carbonate end-member and a silicate end-member are the only sources to $\chi_{Ca^{2+}}^{riv}$ and $\chi_{Na^{+}}^{riv}$ and there is formation of a single secondary phase that uptakes both Ca^{2+} and Na^{+}. If the carbonate and silicate end-members contribute equally to $\chi_{Ca^{2+}}^{riv}$, MEANDIR will calculate that half the Ca^{2+} taken up into the secondary phase derives from the carbonate end-member and the remaining half derives from the silicate end-member. In this case, the gross values of $\chi_{Ca^{2+}}^{carb}$ and $\chi_{Ca^{2+}}^{slct}$ are reduced by the same amount to reach net values. Conversely, if the gross $\chi_{Ca^{2+}}^{carb} = 2\chi_{Ca^{2+}}^{slct}$, then the net values of $\chi_{Ca^{2+}}^{carb}$ and $\chi_{Ca^{2+}}^{slct}$ are reached after removing twice as much from the gross value of $\chi_{Ca^{2+}}^{carb}$ as from that of $\chi_{Ca^{2+}}^{slct}$. If we assume that the carbonate end-member does not contain Na^{+}, the net value of $\chi_{Na^{+}}^{slct}$ is found by subtracting the full amount of Na^{+} taken up into the secondary phase from the gross value of $\chi_{Na^{+}}^{slct}$. If the gross ratio of Na^{+} to Ca^{2+} released from the carbonate and silicate end-members is different than the ratio of Na^{+} to Ca^{2+} in the secondary phase, the net and gross values of R will be different. Below, we give a generalized mathematical treatment of these effects from secondary phase formation on contributions to R, Z, Y, W, and C.

We initially consider the effect of two secondary phases referenced with the superscripts s_1^{second} and s_2^{second}. When considering the net contribution of solute i_{RZC} from end-member s, the net value $^{n}\chi_{i_{RZC}}^{s}$ is calculated by scaling the gross value $^{g}\chi_{i_{RZC}}^{s}$ by one plus the ratio of the uptake into secondary phases, $\chi_{i_{RZC}}^{s_1^{second}}$ and $\chi_{i_{RZC}}^{s_2^{second}}$, to the sum of all sources of i_{RZC}, indexed by $s_{i_{RZC}}^{source}$ over a list of length $n_{i_{RZC}}^{source}$ (eq 92). In turn, the terms for secondary uptake are aggregated into a sum over $s_{i_{RZC}}^{sink}$ indexing a list of length $n_{i_{RZC}}^{sink}$ containing all end-members that uptake solute i_{RZC} from river water. To account for secondary phase formation each gross term in the calculation of R, Z, Y, W, and C must be multiplied by the sum of 1 and the ratio of all solute sinks to all solute sources (eq 93 for $^{n}R_{i_{RZC}\ldots k_{RZC}}$ and eq 94 for $^{n}Z_{i_{RZC}\ldots k_{RZC}}^{FeS_2\,SO_4^{2-}}$). In MEANDIR, the individual gross terms of Y, W, and C are likewise modified to reach net values.

$$
\begin{aligned}
{}^{n}\chi^{s}_{i_{RZC}} &= {}^{g}\chi^{s}_{i_{RZC}} \left(1 + \left(\frac{\chi^{s_1^{second}}_{i_{RZC}}}{\Sigma^{n^{source}_{i_{RZC}}}_{s^{source}_{i_{RZC}}} \left[{}^{g}\chi^{s^{source}_{i_{RZC}}}_{i_{RZC}} \right]} \right) + \left(\frac{\chi^{s_2^{second}}_{i_{RZC}}}{\Sigma^{n^{source}_{i_{RZC}}}_{s^{source}_{i_{RZC}}} \left[{}^{g}\chi^{s^{source}_{i_{RZC}}}_{i_{RZC}} \right]} \right) + \cdots \right) \\
&= {}^{g}\chi^{s}_{i_{RZC}} \left(1 + \frac{\Sigma^{n^{sink}_{i_{RZC}}}_{s^{sink}_{i_{RZC}}} \left[\chi^{s^{sink}_{i_{RZC}}}_{i_{RZC}} \right]}{\Sigma^{n^{source}_{i_{RZC}}}_{s^{source}_{i_{RZC}}} \left[{}^{g}\chi^{s^{source}_{i_{RZC}}}_{i_{RZC}} \right]} \right)
\end{aligned}
\tag{92}
$$

$$
{}^{n}R_{\,i_{RZC}\ldots k_{RZC}} = \frac{\Sigma^{n_{carb}}_{s_{carb}} \left[\Sigma^{k_{RZC}}_{i_{RZC}} \left[\alpha_{i_{RZC}} \left({}^{g}\chi^{s_{carb}}_{i_{RZC}} \right) \left(1 + \frac{\Sigma^{n^{sink}_{i_{RZC}}}_{s^{sink}_{i_{RZC}}} \left[\chi^{s^{sink}_{i_{RZC}}}_{i_{RZC}} \right]}{\Sigma^{n^{source}_{i_{RZC}}}_{s^{source}_{i_{RZC}}} \left[{}^{g}\chi^{s^{source}_{i_{RZC}}}_{i_{RZC}} \right]} \right) \right] \right]}{\Sigma^{n_{weath}}_{s_{weath}} \left[\Sigma^{k_{RZC}}_{i_{RZC}} \left[\alpha_{i_{RZC}} \left({}^{g}\chi^{s_{weath}}_{i_{RZC}} \right) \left(1 + \frac{\Sigma^{n^{sink}_{i_{RZC}}}_{s^{sink}_{i_{RZC}}} \left[\chi^{s^{sink}_{i_{RZC}}}_{i_{RZC}} \right]}{\Sigma^{n^{source}_{i_{RZC}}}_{s^{source}_{i_{RZC}}} \left[{}^{g}\chi^{s^{source}_{i_{RZC}}}_{i_{RZC}} \right]} \right) \right] \right]} \tag{93}
$$

$$
{}^{n}Z^{FeS_2\ SO_4^{2-}}_{i_{RZC}\ldots k_{RZC}} = \frac{\Sigma^{n_{FeS_2\ SO_4^{2-}}}_{s_{FeS_2\ SO_4^{2-}}} \left[2\,{}^{g}\chi^{s_{FeS_2\ SO_4^{2-}}}_{FeS_2\ SO_4^{2-}} \left(1 + \frac{\Sigma^{n^{sink}_{SO_4^{2-}}}_{s^{sink}_{SO_4^{2-}}} \left[\chi^{s^{sink}_{SO_4^{2-}}}_{SO_4^{2-}} \right]}{\Sigma^{n^{source}_{SO_4^{2-}}}_{s^{source}_{SO_4^{2-}}} \left[{}^{g}\chi^{s^{source}_{SO_4^{2-}}}_{SO_4^{2-}} \right]} \right) \right]}{\Sigma^{n_{weath}}_{s_{weath}} \left[\Sigma^{k_{RZC}}_{i_{RZC}} \left[\alpha_{i_{RZC}} \left({}^{g}\chi^{s_{weath}}_{i_{RZC}} \right) \left(1 + \frac{\Sigma^{n^{sink}_{i_{RZC}}}_{s^{sink}_{i_{RZC}}} \left[\chi^{s^{sink}_{i_{RZC}}}_{i_{RZC}} \right]}{\Sigma^{n^{source}_{i_{RZC}}}_{s^{source}_{i_{RZC}}} \left[{}^{g}\chi^{s^{source}_{i_{RZC}}}_{i_{RZC}} \right]} \right) \right] \right]} \tag{94}
$$

R, Z, Y, W, and C with scaled values.—A final complexity in calculating R, Z, Y, W, and C arises in the case of systematic difference between inversion results and river observations. In general, the composition of a river sample calculated using the inversion model results may not exactly match river observations. In a case where the model results consistently under-predict observed $\chi^{riv}_{Na^+}$ $\left(\Sigma^{n}_{s}\left[f^{s}{}_{Na^+}\right] < 1\right)$ and over-predict observed $\chi^{riv}_{Ca^{2+}}$ $\left(\Sigma^{n}_{s}\left[f^{s}{}_{Ca^{2+}}\right] > 1\right)$ in a sample, the calculated value of R will likely be different compared to a case where both $\chi^{riv}_{Na^+}$ and $\chi^{riv}_{Ca^{2+}}$ are reconstructed more accurately. To enforce the condition that fractional contributions should sum to 1, even when the results of the cost function optimization do not meet that criteria, it is formally possible to normalize each fractional contribution to the sum of all fractional contributions during the calculation of weathering parameters (eqs 95–97, where s indexes the list of length n containing all end-members). We refer to this normalization as the "scaled" value of a parameter. That is, the calculation of scaled weathering parameters ($_{sc}$R, $_{sc}$Z, $_{sc}$Y, $_{sc}$W, and $_{sc}$C) adapts the inversion results to better recreate sample observations. Results with and without scaling will be very similar if MEANDIR is able to fit observations well and converge to the same value when observations are perfectly reconstructed ($\Sigma^{n}_{s}[f^{s}{}_{i}] = 1$). In general, we urge caution in using scaled parameters as these derived variables are a modified version of the inversion results and are not natural solutions to the mixing model.

$$ {}^{n}_{sc}\chi^{s}_{i_{RZC}} = \frac{{}^{n}\chi^{s}_{i_{RZC}}}{\Sigma^{n}_{s}\left[f^{s}_{i_{RZC}}\right]} = \frac{{}^{g}\chi^{s}_{i_{RZC}}}{\Sigma^{n}_{s}\left[f^{s}_{i_{RZC}}\right]}\left(1+\frac{\Sigma^{n^{sink}_{i_{RZC}}}_{s^{sink}_{i_{RZC}}}\left[\chi^{s^{sink}_{i_{RZC}}}_{i_{RZC}}\right]}{\Sigma^{n^{source}_{i_{RZC}}}_{s^{source}_{i_{RZC}}}\left[{}^{g}\chi^{s^{source}_{i_{RZC}}}_{i_{RZC}}\right]}\right) \tag{95} $$

$$ {}^{n}_{sc}R_{i_{RZC}\ldots k_{RZC}} = \frac{\Sigma^{n_{carb}}_{s_{carb}}\left[\Sigma^{k_{RZC}}_{i_{RZC}}\left[\alpha_{i_{RZC}}\left(\frac{{}^{g}\chi^{s_{carb}}_{i_{RZC}}}{\Sigma^{n}_{s}\left[f^{s}_{i_{RZC}}\right]}\right)\left(1+\frac{\Sigma^{n^{sink}_{i_{RZC}}}_{s^{sink}_{i_{RZC}}}\left[\chi^{s^{sink}_{i_{RZC}}}_{i_{RZC}}\right]}{\Sigma^{n^{source}_{i_{RZC}}}_{s^{source}_{i_{RZC}}}\left[{}^{g}\chi^{s^{source}_{i_{RZC}}}_{i_{RZC}}\right]}\right)\right]\right]}{\Sigma^{n_{weath}}_{s_{weath}}\left[\Sigma^{k_{RZC}}_{i_{RZC}}\left[\alpha_{i_{RZC}}\left(\frac{{}^{g}\chi^{s_{weath}}_{i_{RZC}}}{\Sigma^{n}_{s}\left[f^{s}_{i_{RZC}}\right]}\right)\left(1+\frac{\Sigma^{n^{sink}_{i_{RZC}}}_{s^{sink}_{i_{RZC}}}\left[\chi^{s^{sink}_{i_{RZC}}}_{i_{RZC}}\right]}{\Sigma^{n^{source}_{i_{RZC}}}_{s^{source}_{i_{RZC}}}\left[{}^{g}\chi^{s^{source}_{i_{RZC}}}_{i_{RZC}}\right]}\right)\right]\right]} \tag{96} $$

$$ {}^{n}_{sc}Z^{FeS_2\ SO_4^{2-}}_{i_{RZC}\ldots k_{RZC}} = \frac{\Sigma^{n_{FeS_2\ SO_4^{2-}}}_{s_{FeS_2\ SO_4^{2-}}}\left[\left(\frac{2\,{}^{g}\chi^{s_{FeS_2\ SO_4^{2-}}}_{FeS_2\ SO_4^{2-}}}{\Sigma^{n}_{s}\left[f^{s}_{SO_4^{2-}}\right]}\right)\left(1+\frac{\Sigma^{n^{sink}_{SO_4^{2-}}}_{s^{sink}_{SO_4^{2-}}}\left[\chi^{s^{sink}_{SO_4^{2-}}}_{SO_4^{2-}}\right]}{\Sigma^{n^{source}_{SO_4^{2-}}}_{s^{source}_{SO_4^{2-}}}\left[{}^{g}\chi^{s^{source}_{SO_4^{2-}}}_{SO_4^{2-}}\right]}\right)\right]}{\Sigma^{n_{weath}}_{s_{weath}}\left[\Sigma^{k_{RZC}}_{i_{RZC}}\left[\alpha_{i_{RZC}}\left(\frac{{}^{g}\chi^{s_{weath}}_{i_{RZC}}}{\Sigma^{n}_{s}\left[f^{s}_{i_{RZC}}\right]}\right)\left(1+\frac{\Sigma^{n^{sink}_{i_{RZC}}}_{s^{sink}_{i_{RZC}}}\left[\chi^{s^{sink}_{i_{RZC}}}_{i_{RZC}}\right]}{\Sigma^{n^{source}_{i_{RZC}}}_{s^{source}_{i_{RZC}}}\left[{}^{g}\chi^{s^{source}_{i_{RZC}}}_{i_{RZC}}\right]}\right)\right]\right]} \tag{97} $$

In summary, MEANDIR calculates four different values of R, Z, Y, W, and C reflecting net or gross fluxes and with or without scaling to the sum of all fractional contributions. In the absence of secondary phase formation, the net and gross parameters are equal. For most applications, we recommend using the net weathering parameters derived without scaling (eqs 93 and 94).

Including $\chi^{slct}_{Na^+}$ and $\chi^{slct}_{K^+}$ in R and Z.—Researchers disagree on the appropriate role of $\chi^{slct}_{Na^+}$ and $\chi^{slct}_{K^+}$ when using river chemistry to study the carbon cycle. In part, this argument reflects the need to distinguish between the drawdown of atmospheric CO_2 and the drawdown of DIC. Below, we argue that $\chi^{slct}_{Na^+}$ and $\chi^{slct}_{K^+}$ can be partially neglected or excluded when quantifying the removal of DIC from the ocean-atmosphere system but should be included when quantifying the impact of chemical denudation on the concentration of atmospheric CO_2. Because R and Z capture dynamics relating to the latter, we suggest that $\chi^{slct}_{Na^+}$ and $\chi^{slct}_{K^+}$ should be included in the weathering parameters discussed above. Note, however, that MEANDIR calculates R and Z based on user-supplied criteria and is agnostic to the opinion of its authors. Regardless of which elements are included, the denominators of R, Z, and C should all be calculated using the same cations.

The common argument against including $\chi^{slct}_{Na^+}$ and $\chi^{slct}_{K^+}$ in calculations of carbon drawdown is that, because alkali cations are removed from seawater during reverse weathering, $\chi^{slct}_{Na^+}$ and $\chi^{slct}_{K^+}$ do not contribute to loss of carbon during burial of marine $CaCO_3$. In the same framework, $\chi^{slct}_{Mg^{2+}}$ is often considered interchangeable with $\chi^{slct}_{Ca^{2+}}$ despite that Mg-bearing carbonate is not directly precipitated in the modern ocean. Rather, the principal loss of marine Mg^{2+} is through hydrothermal vent circulation, which entails both Mg^{2+}-Ca^{2+} exchange and reverse weathering

reactions (Edmond and others, 1979a, 1979b). It is worth noting that fully including or excluding $\chi^{slct}_{Na^+}$ and $\chi^{slct}_{K^+}$ in calculations of carbon drawdown lacks historical precedent. For example, Gaillardet and others (1999) report results for different combinations of cations, while Galy and France-Lanord (1999) assume that 30% of $\chi^{slct}_{Na^+}$ and 20% of $\chi^{slct}_{K^+}$ can be included in their calculations due to the participation of these ions in exchange reactions that ultimately liberate Ca^{2+}. Overall, we largely agree with the practice of using $\chi^{slct}_{Ca^{2+}}$ and fractions of $\chi^{slct}_{Mg^{2+}}$, $\chi^{slct}_{Na^+}$ and $\chi^{slct}_{K^+}$ to quantify DIC removal from the ocean-atmosphere system.

Conversely, because atmospheric pCO_2 is set by the balance between marine ALK and DIC, accounting for the impacts of weathering on atmospheric carbon dioxide requires considering $\chi^{slct}_{Na^+}$ and $\chi^{slct}_{K^+}$. The role of $\chi^{slct}_{Na^+}$ and $\chi^{slct}_{K^+}$ in impacting pCO_2 is analogous but opposite to that of $\chi^{riv}_{SO_4^{2-}}$ derived from FeS_2 oxidation; the three fluxes alter pCO_2 through repartitioning of carbon between the ocean and atmosphere without altering total ocean-atmosphere DIC. However, like FeS_2 oxidation, $\chi^{slct}_{Na^+}$ and $\chi^{slct}_{K^+}$ only impact pCO_2 if their inputs to seawater are out of balance with their loss terms. Leaving $\chi^{slct}_{Na^+}$ and $\chi^{slct}_{K^+}$ out of R and Z is effectively assuming steady-state in the biogeochemical cycles of Na^+ and K^+, akin to setting $Z = 0$ by assuming steady-state in the global biogeochemical cycle of SO_4^{2-}. Whether or not to include $\chi^{slct}_{Na^+}$ and $\chi^{slct}_{K^+}$ in R and Z is thus a question of whether the seawater concentrations of Na^+ and K^+ are assumed to be changing. As it is common to study the role of weathering in response to geologic perturbations to the carbon cycle, such as the Paleocene Eocene Thermal Maximum, it may be particularly important to account for non-steady-state behavior in global biogeochemical cycles. Our opinion is that, when using the R-Z-C space to quantify the impacts of weathering on pCO_2, $\chi^{slct}_{Na^+}$ and $\chi^{slct}_{K^+}$ should be included in the weathering parameters so that they reflect the actual χ_{ALK}/χ_{DIC} of the weathering system itself and not an assumption of marine processes. Lastly, including Na^+ and K^+ captures the maximum alkalinity generated through chemical weathering and is more conservative than leaving them out when evaluating the impacts of FeS_2 oxidation and C_{org} oxidation on pCO_2.

APPLICATIONS OF MEANDIR

Overview of Inversion Scenarios

We present selected results from inversion of five previously published river chemistry datasets to demonstrate the functionality of MEANDIR and its sensitivity to parameter choices (tables 5, 6, 7, 8, 9, 10, 11, 12, and 13). The first dataset is a global compilation of major element concentrations from Gaillardet and others (1999), the second dataset is the major element chemistry of global river water samples from Burke and others (2018), the third is the major element chemistry and SO_4^{2-} $\delta^{34}S$ values of river water samples from the Peruvian Amazon reported in Torres and others (2016), the fourth is the major element chemistry of Icelandic rivers from Gíslason and others (1996), and the fifth is the major and trace element chemistry of Mackenzie River water samples from Horan and others (2019). The scenarios are indexed alphanumerically by the initials of the first author on the article underlying each data source: JG for Gaillardet and others (1999), AB for Burke and others (2018), MT for Torres and others (2016), SG for Gíslason and others (1996), and KH for Horan and others (2019). For a given data source, scenario numbering follows the order in which results are presented in the text. We consider results from 28 different inversion scenarios across these five datasets: 12 JG scenarios (tables 5 and 7), 6 AB

TABLE 5

Summary of river inversion scenarios using data from Gaillardet and others (1999)

Parameters	Default: JG-1	JG-2(c)	JG-3(c)	JG-4(c)	JG-5(c)	JG-6	JG-7	JG-8
Variables	$\chi_{Ca^{2+}}$, $\chi_{Mg^{2+}}$, $\chi_{Na^{+}}$, $\chi_{Cl^{-}}$						$+\chi_{HCO_3^-}$	$+\chi_{HCO_3^-}$
Reconstructed observations	10^{-4} - 10^{4} % (sensitivity testing)	85-115%	85-115%	85-115%	85-115%	N/A	85-115%	85-115%
Normalization	$\chi_{Ca^{2+}}+\chi_{Mg^{2+}}+\chi_{Na^{+}}$			$\chi_{Na^{+}}$				
EM distribution	normal		uniform				uniform	uniform
Cost function	relative				absolute			
Cull solutions	sample matching					1%, all samples		
SO_4^{2-} treatment	$\chi_{SO_4^{2-}}$ not included							
Max attempted simulations	10^5	10^6 ($3{\cdot}10^5$)	10^6 ($3{\cdot}10^5$)	10^6 ($3{\cdot}10^5$)	10^6 ($3{\cdot}10^5$)	10^5	10^6	10^6
Successful simulations (25th)	10^5	10^3 (10^3)	10^3 (10^3)	10^3 (10^3)	10^3 (10^3)	10^3	10^3	10^3
End-member distributions	$\chi_{HCO_3^-}$ not in the inversion						$\chi_{HCO_3^-}/\chi_{\Sigma^+}$ variable	$\chi_{HCO_3^-}/\chi_{\Sigma^+}$ fixed

When evaluated using values of $\chi^{riv}_{Cl^-\ critical}$, scenarios are appended with the letter "c". Blank entries indicate the parameter is unchanged from the default case (JG-1). Nearly all model results are accepted in scenario JG-1, which is used for sensitivity testing (fig. 2), while in other scenarios only a subset of simulation results are accepted based on either sample matching (JG-2 through JG-5, JG-7, JG8) or lowest misfit fraction (JG-6). In all scenarios except JG-8 the inversion end-members are precipitation, carbonate, silicate, and evaporite (stoichiometrically constrained). Scenario JG-7 has variable $\chi_{HCO_3^-}/\chi_{\Sigma^+}$ ratios, while scenario JG-8 has two silicate and two carbonate end-members with fixed ratios of $\chi_{HCO_3^-}/\chi_{\Sigma^+}$. Entries in the successful simulations row are the 25th percentile of the number of accepted simulations across all samples in the scenario.

TABLE 6

Summary of river inversion scenarios using the global river data of Burke and others (2018)

Parameters	Default: AB-1	AB-2	AB-3	AB-4	AB-5	AB-6
Variables	$\chi_{Ca^{2+}}$, $\chi_{Mg^{2+}}$, $\chi_{Na^{+}}$, $\chi_{Cl^{-}}$, $\chi_{SO_4^{2-}}$	$+\chi_{HCO_3^{-}}$, not in cost function	$+\chi_{HCO_3^{-}}$, in cost function	$-\chi_{SO_4^{2-}}$		
Reconstructed observations	85-115%					
Normalization	$\chi_{Ca^{2+}}+\chi_{Mg^{2+}}+\chi_{Na^{+}}$				$+\chi_{SO_4^{2-}}$	
EM distribution	uniform					
Cost function	relative					
Cull solutions	sample matching					
SO_4^{2-} treatment	in end-members			excess	other	
Max attempted simulations	10^6					
Successful simulations (25th)	10^3					
End-member distributions	$\chi_{FeS_2\,SO_4^{2-}}/\chi_{\Sigma^{+}}$ ranges from 0 to 1					$\chi_{FeS_2\,SO_4^{2-}}/\chi_{\Sigma^{+}}$ ranges from 0 to 0.15

Blank entries indicate the parameter is unchanged from the default case (AB-1), while entries of "Variables" (AB-2, AB-3, AB-4), "Normalization" (AB-5), or "SO_4^{2-} treatment" (AB-4, AB-5) are modifications to the default values. Scenarios AB-2 and AB-3 differ by whether the misfit of model results from calculated $\chi^{riv}_{HCO_3^{-}}/\chi^{riv}_{\Sigma^{+}}$ is included in the cost function. In scenario AB-6, the carbonate and silicate end-members have smaller ranges for $\chi_{FeS_2\,SO_4^{2-}}/\chi_{\Sigma^{+}}$, which we find impacts the inversion-constrained median values of carbonate weathering fraction (R). Inversion end-members are precipitation, silicate, carbonate, and evaporite (stoichiometrically constrained) and scenario AB-5 contains an additional end-member representing other SO_4^{2-}. Entries in the successful simulations row are the 25th percentile of the number of accepted simulations across all samples in the scenario.

TABLE 7

Summary of end-members for inversion of data from Gaillardet and others (1999) and Burke and others (2018): JG-1 through JG-8 and AB-1 through AB-6

Notes	Ratio	Precipitation	Carbonate	Silicate	Evaporite	Other
Scenarios JG-1, 2, 2c, 5, 5c, and 6. Ratios are relative to sum $\chi_{Ca^{2+}}$, $\chi_{Mg^{2+}}$, $\chi_{Na^{+}}$ in eq/eq.	$2\chi_{Ca^{2+}}$	0.036±0.015	0.663±0.173	0.315±0.138	0.454±0.183	–
	$2\chi_{Mg^{2+}}$	0.174±0.013	0.332±0.172	0.226±0.120	0.088±0.064	–
	$\chi_{Na^{+}}$	0.790±0.017	0.005±0.004	0.443±0.117	0.447±0.155	–
	$\chi_{Cl^{-}}$	0.908±0.082	0.000±0.000	0.000±0.000	0.437±0.184	–
	$2\chi_{SO_4^{2-}}$	0.095±0.016	0.001±0.001	0.017±0.007	0.342±0.226	–
Scenarios JG-3, 3c, 7, 8, AB-1, 2, 3, 4, 6. Ratios relative to sum of $\chi_{Ca^{2+}}$, $\chi_{Mg^{2+}}$, and $\chi_{Na^{+}}$ in eq/eq. In AB-6, some $\chi_{FeS_2\,SO_4^{2-}}$ ratios are lower (0-0.15).	$2\chi_{Ca^{2+}}$	0.006–0.066	0.317–1.000	0.039–0.591	0.088–0.820	–
	$2\chi_{Mg^{2+}}$	0.148–0.200	0.000–0.675	0.000–0.466	0.000–0.216	–
	$\chi_{Na^{+}}$	0.756–0.824	0.000–0.013	0.209–0.677	0.137–0.757	–
	$\chi_{Cl^{-}}$	0.744–1.072	0.000–0.000	0.000–0.000	0.069–0.805	–
	$\chi_{HCO_3^{-}}$	0.000–0.000	0.500–1.000	0.000–1.000	0.000–0.000	–
	$2\chi_{SO_4^{2-}}$	0.063–0.127	0.000–0.003	0.003–0.031	0.000–0.794	–
	$\delta^{34}S$	15–20‰	10–30‰	0–5‰	10–30‰	–
	$\chi_{FeS_2\,SO_4^{2-}}$	0.000–0.000 (0.00–0.00)	0.000–1.000 (0.00–0.15)	0.000–1.000 (0.00–0.15)	0.000–0.000 (0.00–0.00)	–
Scenarios JG-4, 4c. Ratios relative to $\chi_{Na^{+}}$ in μM/μM.	$\chi_{Ca^{2+}}$	0.023±0.010	60.00±30.00	0.350±0.250	0.500±0.500	–
	$\chi_{Mg^{2+}}$	0.110±0.010	30.00±15.00	0.250±0.200	0.100±0.080	–
	$\chi_{Na^{+}}$	1.000±0.000	1.000±0000	1.000±0.000	1.000±0.000	–
	$\chi_{Cl^{-}}$	1.150±0.100	0.000±0000	0.000±0.000	1.000±0.200	–
	$\chi_{SO_4^{2-}}$	0.060±0.010	0.060±0.030	0.019±0.005	0.400±0.200	–
Scenario AB-5. Ratios relative to sum of $\chi_{Ca^{2+}}$, $\chi_{Mg^{2+}}$, $\chi_{Na^{+}}$, and $\chi_{SO_4^{2-}}$ in eq/eq.	$2\chi_{Ca^{2+}}$	0.005–0.061	0.317–1.000	0.039–0.591	0.012–0.660	0
	$2\chi_{Mg^{2+}}$	0.133–0.185	0.000–0.675	0.000–0.466	0.000–0.159	0
	$\chi_{Na^{+}}$	0.685–0.757	0.000–0.013	0.209–0.677	0.128–0.520	0
	$\chi_{Cl^{-}}$	0.680–0.980	0.000–0.000	0.000–0.000	0.078–0.562	0
	$2\chi_{SO_4^{2-}}$	0.061–0.113	0.000–0.000	0.000–0.000	0.031–0.479	1
	$\delta^{34}S$	15–20‰	–	–	10–30‰	–

Ratios are given as the mean and standard deviation of normal distributions for variables normalized to $\chi_{\Sigma^{+}}$ or $\chi_{Na^{+}}$, as well as the minimum and maximum values of uniform distributions normalized to $\chi_{\Sigma^{+}}$ or $\chi_{\Sigma^{+}+SO_4^{2-}}$. Na^{+}-normalized values are from Burke and others (2018), and values normalized to $\chi_{\Sigma^{+}}$ or $\chi_{\Sigma^{+}+SO_4^{2-}}$ were calculated by Monte Carlo simulation from the Na^{+}-normalized distributions. All scenarios have $\chi_{Cl^{-}}^{evap} = \chi_{Na^{+}}^{evap}$ and all scenarios including $\chi_{SO_4^{2-}}$ have $\chi_{SO_4^{2-}}^{evap} = \chi_{Ca^{2+}}^{evap} + \chi_{Mg^{2+}}^{evap}$.

scenarios (tables 6 and 7), 7 MT scenarios (tables 8 and 9), 1 SG scenario (tables 10 and 11), and 2 KH scenarios (tables 12 and 13). Relevant inversion parameters and end-member chemical compositions are tabulated for all scenarios (tables 5–13), and the full suite of inversion parameters are included in the MEANDIR download.

Scenarios JG-1 through JG-8 and JG-2c through JG-5c operate on the global dataset of Gaillardet and others (1999) (tables 5 and 7). Scenario JG-1 describes a large inversion that accepts nearly all simulation results, with other parameter selections reflecting our favored settings, in order to perform sensitivity testing. Scenario JG-2 describes a modified inversion in which only a subset of results are kept, and most scenarios reflect a change of only one or two parameters from scenario JG-2. Scenario JG-3 uses uniform distributions for end-member chemistry and scenario JG-4 normalizes observations and end-members with $\chi_{Na^{+}}$ rather than $\chi_{\Sigma^{+}}$. Scenario JG-5 solves each combination of observations and end-members using a constrained optimization

TABLE 8

Summary of river inversion scenarios using data from Torres and others (2016)

Parameters	Default: MT-1	MT-2	MT-3	MT-4	MT-5	MT-6	MT-7
Variables	$\chi_{Ca^{2+}}$, $\chi_{Mg^{2+}}$, $\chi_{Sr^{2+}}$, $\chi_{Na^{+}}$, $\chi_{Cl^{-}}$, $\chi_{SO_4^{2-}}$					$-\chi_{SO_4^{2-}}$	
Reconstructed observations	85-115%		N/A	N/A			
Normalization	$\chi_{Ca^{2+}}+\chi_{Mg^{2+}}+\chi_{Na^{+}}+\chi_{Sr^{2+}}$						$+\chi_{SO_4^{2-}}$
EM distribution	uniform						
Cost function	relative	absolute		absolute			
Cull solutions	sample matching		1%, each sample	1%, each sample			
SO_4^{2-} treatment	in end-members					excess	other
Max attempted simulations	$3{\cdot}10^5$		$3{\cdot}10^4$	$3{\cdot}10^4$	$4{\cdot}10^5$	$4{\cdot}10^5$	$4{\cdot}10^5$
Successful simulations (25th)	$3{\cdot}10^2$	10^2			10^3	10^3	10^3

Blank entries indicate the parameter is unchanged from the default case (MT-1). In scenarios MT-3 and MT-4, the 1% of 30,000 simulations with lowest cost function evaluation are retained for additional analysis. Note that MT-5 is identical to MT-1 except that it has more successful simulations. Inversion end-members are precipitation, dolomite, silicate, and shale, and scenario MT-7 contains an additional end-member representing FeS_2 oxidation. $\chi^{riv}_{Cl^-}$ is not corrected using values of $\chi^{riv}_{Cl^-\ critical}$. In simulations MT-1 through MT-5, FeS_2 oxidation is included within the lithologic end-members. In MT-6, FeS_2 oxidation is diagnosed following the approach of Burke and others (2018). In MT-7, FeS_2 oxidation is an independent end-member. Entries in the successful simulations row are the 25th percentile of the number of accepted simulations across all samples in the scenario.

TABLE 9

Summary of inversion end-members for Torres and others (2016): MT-1 through MT-7

Notes	Ratio	Precipitation	Dolomite	Silicate	Shale	FeS_2
Scenarios MT-1, 2, 3, 4, 5, 6. Ratios relative to sum of $\chi_{Ca^{2+}}$, $\chi_{Mg^{2+}}$, χ_{Na^+}, and $\chi_{Sr^{2+}}$ in eq/eq.	$2\chi_{Ca^{2+}}$	0.200 – 0.650	0.500 – 1.000	0.030 – 0.400	0.030 – 0.300	–
	$2\chi_{Mg^{2+}}$	0.100 – 0.200	0.000 – 0.500	0.003 – 0.030	0.450 – 0.600	–
	$10^3 \cdot 2\chi_{Sr^{2+}}$	0.050 – 5.000	1.000 – 9.000	0.500 – 2.500	0.500 – 2.500	–
	χ_{Na^+}	0.050 – 0.430	0.000 – 0.000	0.500 – 0.800	0.100 – 0.200	–
	χ_{Cl^-}	0.060 – 0.500	0.000 – 0.000	0.000 – 0.000	0.000 – 0.000	–
	$2\chi_{SO_4^{2-}}$	0.060 – 0.400	0.000 – 0.000	0.000 – 0.000	0.000 – 0.000	–
	$\chi_{FeS_2\ SO_4^{2-}}$	0.000 – 0.000	0.000 – 1.000	0.000 – 1.000	0.000 – 1.000	–
	$\delta^{34}S$	-5‰ – 9‰	calculated	calculated	calculated	–
Scenario MT-7. Ratios relative to sum of $\chi_{Ca^{2+}}$, $\chi_{Mg^{2+}}$, χ_{Na^+}, $\chi_{Sr^{2+}}$, and $\chi_{SO_4^{2-}}$ in eq/eq.	$2\chi_{Ca^{2+}}$	0.212 – 0.600	0.500 – 1.000	0.030 – 0.400	0.030 – 0.300	0
	$2\chi_{Mg^{2+}}$	0.065 – 0.221	0.000 – 0.500	0.003 – 0.030	0.450 – 0.600	0
	$10^3 \cdot 2\chi_{Sr^{2+}}$	0.000 – 6.000	1.000 – 9.000	0.500 – 2.500	0.500 – 2.500	0
	χ_{Na^+}	0.045 – 0.413	0.000 – 0.000	0.500 – 0.800	0.100 – 0.200	0
	χ_{Cl^-}	0.000 – 0.549	0.000 – 0.000	0.000 – 0.000	0.000 – 0.000	0
	$2\chi_{SO_4^{2-}}$	0.050 – 0.390	0.000 – 0.000	0.000 – 0.000	0.000 – 0.000	1
	$\delta^{34}S$	-5‰ – 9‰	-	-	-	calculated

Chemical ratios normalized to the sum of $\chi_{Ca^{2+}}$, $\chi_{Mg^{2+}}$, χ_{Na^+}, and $\chi_{Sr^{2+}}$ are after Torres and others (2016). Ratios including $\chi_{SO_4^{2-}}$ in the normalization were reached through Monte Carlo simulation of the data normalized to χ_{Σ^+}. For all scenarios the isotopic composition of the FeS_2 end-member is constrained through inversion.

of absolute misfit rather than proportional misfit. Scenarios JG-2 through JG-5 are also evaluated using $\chi^{riv}_{Cl^-\ critical}$ values, in which case the scenario number is appended with "c". Because $\chi^{riv}_{Cl^-\ critical}$ values are not available in the original publication (Gaillardet and others, 1999), we instead select $\chi^{riv}_{Cl^-\ critical}$ values for each sample that are a random fraction of $\chi^{riv}_{Cl^-}$. This is merely for demonstration purposes; simulations with randomly selected $\chi^{riv}_{Cl^-\ critical}$ values are not used to reach conclusions regarding controls on weathering or its influence on climate. The criteria for a single simulation

TABLE 10

Summary of inversion scenario for the data of Gíslason and others (1996)

Parameters	SG-1
Variables	$\chi_{Ca^{2+}}, \chi_{Mg^{2+}}, \chi_{Na^+}, \chi_{Cl^-}$
Reconstructed observations	85-115%
Normalization	$\chi_{Ca^{2+}} + \chi_{Mg^{2+}} + \chi_{Na^+}$
EM distribution	normal
Cost function	relative
Cull solutions	sample matching
SO_4^{2-} treatment	$\chi_{SO_4^{2-}}$ not included
Max attempted simulations	10^6
Successful simulations (25^{th})	10^3

The inversion end-members are basalt, precipitation, and secondary clay formation ("clay"). Entries in the successful simulations row are the 25^{th} percentile of the number of accepted simulations across all samples in the scenario.

TABLE 11

Summary of inversion end-members for Gíslason and others (1996): SG-1

Notes	Ratio	Precipitation	Basalt	Clay
Scenario SG-1. Ratios relative to sum of $\chi_{Ca^{2+}}$, $\chi_{Mg^{2+}}$, and $\chi_{Na^{+}}$ in eq/eq.	$2\chi_{Ca^{2+}}$	0.051 ± 0.045	0.480 ± 0.062	0.500 ± 0.500
	$2\chi_{Mg^{2+}}$	0.173 ± 0.024	0.393 ± 0.111	0.500 ± 0.500
	$\chi_{Na^{+}}$	0.776 ± 0.072	0.116 ± 0.069	0.500 ± 0.500
	$\chi_{Cl^{-}}$	0.910 ± 0.150	0.000 ± 0.000	0.000 ± 0.000
	$2\chi_{SO_4}$	0.122 ± 0.108	0.000 ± 0.000	0.000 ± 0.000

Ratios are given as the mean and standard deviation of normal distributions normalized to χ_{Σ^+}. The chemistry of precipitation is calculated from observations at the Íráfoss meteorological station collected as part of the European Monitoring and Evaluation Programme under the Convention on Long-range Transboundary Air Pollution, but with reduced variability in normalized $\chi^{prec}_{Cl^-}$. The chemical composition of basalt is calculated from observations in Torssander (1989), Gíslason and others (1996), and Moulton and others (2000). The chemistry of the secondary clay is intentionally general for comparison of inversion-constrained values to the observations of Moulton and others (2000) and Thorpe and others (2019).

to count as successful in scenarios JG-2 through JG-5 and JG-2c through JG-5c is that the sum of fractional contributions from all end-members to each dissolved variable is between 85% and 115%. Conversely, in scenario JG-6 all samples are presented with the same end-members and all results are temporarily accepted. At the conclusion of the inversion, the 1% of simulations with lowest misfit between observations and model results, as evaluated across all samples, are retained for additional analysis. Scenarios JG-7 and JG-8 differ from scenario JG-3 by including $\chi^{riv}_{HCO_3^-}$ in the inversion. Scenario JG-7 uses end-members where $\chi^{s}_{HCO_3^-}/\chi^{s}_{\Sigma^+}$ ratios are drawn from distributions, while scenario JG-8 uses end-members with fixed ratios of $\chi^{s}_{HCO_3^-}/\chi^{s}_{\Sigma^+}$ (Blattmann and others, 2019).

Scenarios AB-1 through AB-6 invert the river chemistry dataset of Burke and others (2018) (tables 6 and 7). Scenarios AB-1, AB-2, and AB-3 differ by whether $\chi^{riv}_{HCO_3^-}$ is included or excluded from the inversion and cost function. Scenario AB-4 quantifies Z with $\chi^{riv}_{excess\ SO_4^{2-}}$ and does not include $\chi^{riv}_{SO_4^{2-}}$ in the inversion, and scenario AB-5 uses an independent end-member to quantify $\chi^{other}_{SO_4^{2-}}$. Notably, the AB-5 scenario uses our novel normalization where χ_{norm} includes $\chi_{SO_4^{2-}}$. Scenario AB-6 is identical to AB-1 except that the carbonate and silicate end-members are constrained to have $\chi^{s}_{FeS_2\ SO_4^{2-}}/\chi^{s}_{\Sigma^+}$ ratios ranging from 0 to 0.15 instead of from 0 to 1, which we find impacts the inversion-constrained value of the median carbonate weathering fraction.

Scenarios MT-1 through MT-7 operate on the dataset of water samples presented in Torres and others (2016) (tables 8 and 9). Scenario MT-1 is the default scenario for these inversions, and scenarios MT-2 and MT-4 differ by optimizing to absolute misfit rather than proportional misfit. Similar to scenario JG-6, in scenarios MT-3 and MT-4 all samples are presented with the same end-members and all results are temporarily accepted. At the conclusion of the inversion, the 1% of simulations with lowest misfit between observations and model results, but in this case evaluated at the level of each individual sample, are retained for additional analysis. Scenario MT-5 is identical to MT-1 except that it has ~1000 successful simulations for each sample. Scenario MT-6 differs from scenario MT-5 by calculating Z from excess SO_4^{2-} rather than including $\chi^{riv}_{SO_4^{2-}}$ directly in the inversion, and scenario MT-7 treats FeS_2 oxidation as an independent end-member. As in AB-5, in MT-7 the normalization includes $\chi_{SO_4^{2-}}$.

TABLE 12

Summary of river inversion scenarios using data from Horan and others (2019)

Parameters	Default: KH-1	KH-2
Variables	$\chi_{Ca^{2+}}$, $\chi_{Mg^{2+}}$, $\chi_{Na^{+}}$, $\chi_{Cl^{-}}$, $\chi_{SO_4^{2-}}$, χ_{Re}, χ_{ALK}, χ_{DIC}	
Reconstructed observations	85-115%	
Normalization	$\chi_{Ca^{2+}}+\chi_{Mg^{2+}}+\chi_{Na^{+}}+\chi_{ALK}+\chi_{DIC}$	$-\chi_{ALK}$, $+\chi_{SO_4^{2-}}$
EM distribution	uniform	
Cost function	relative	
Cull solutions	sample matching	
SO_4^{2-} treatment	other	
Max attempted simulations	10^6	
Successful simulations (25th)	10^3	

Blank entries indicate the parameter is unchanged from the default case (KH-1). The inversion end-members are precipitation, dolomite, silicate, FeS_2 oxidation, C_{org} oxidation, and atmospheric gas exchange. Entries in the successful simulations row are the 25th percentile of the number of accepted simulations across all samples in the scenario.

We compare estimates for the $\delta^{34}S$ of lithologic FeS_2 across scenarios MT-5, MT-6, and MG-7 and, through comparison to measured bedrock $\delta^{34}S$ values reported in Torres and others (2016), validate the application of river inversion models for constraining bedrock sulfur isotope composition.

Scenario SG-1 operates on the dataset of Icelandic river water samples from Gíslason and others (1996) (tables 10 and 11). The only solute sources in this inversion are meteoric precipitation and basalt weathering, and we consider one solute sink due to the formation of secondary clay. Our analysis focuses on using MEANDIR to quantify the chemical composition of the secondary clay end-member. We compare inversion results with observations of Icelandic clay chemistry from Moulton and others (2000) and Thorpe and others (2019).

Scenarios KH-1 and KH-2 invert water samples from the Mackenzie River reported in Horan and others (2019) (tables 12 and 13). Our analysis uses $\chi^{riv}_{\Sigma^+}$, $\chi^{riv}_{SO_4^{2-}}$, and χ^{riv}_{Re} to simultaneously quantify chemical weathering, FeS_2 oxidation, and C_{org} oxidation, respectively. The normalized χ_{Re} ratios for organic carbon oxidation are derived from the text of Horan and others (2019), while the ratios for the FeS_2 and silicate end-members are estimated from figure 4B of that same work. KH-1 is normalized to $\chi_{\Sigma^+ + ALK + DIC}$ and KH-2 is normalized to $\chi_{\Sigma^+ + SO_4^{2-} + DIC}$, but the scenarios are otherwise identical. The results of KH-1 and KH-2 are extremely similar despite the different normalizations. We only show results for KH-1 but for completeness also present the inversion parameters for KH-2 (tables 12 and 13).

Given that KH-1 and KH-2 are intended merely as proof-of-concept that MEANDIR can use new normalizations to quantify FeS_2 oxidation and C_{org} oxidation as independent end-members, we make several simplifying assumptions in these scenarios. First, we assume that no evaporites are present in the sampled catchments. Second, we allow the silicate and carbonate end-members to take on a wide range of possible chemical compositions. Third, we assume that river χ^{riv}_{ALK} and χ^{riv}_{DIC} are equal to $\chi^{riv}_{HCO_3^-}$. Although this assumption is less than ideal, the dearth of existing χ^{riv}_{Re} measurements limits the number of datasets where quantification of C_{org} oxidation

TABLE 13

Inversion end-members for Horan and others (2019): KH-1 and KH-2

Notes	Ratio	Precipitation	Carbonate	Silicate	FeS_2	C_{org}	Atmosphere
Scenario KH-1. Ratios relative to sum of $\chi_{Ca^{2+}}$, $\chi_{Mg^{2+}}$, χ_{Na^+}, χ_{ALK}, and χ_{DIC} in eq/eq.	$2\chi_{Ca^{2+}}$	0.008 – 0.060	0.20 – 0.40	0.05 – 0.25	0.0 – 0.0	00 – 00	0.0 – 0.0
	$2\chi_{Mg^{2+}}$	0.122 – 0.190	0.00 – 0.20	0.05 – 0.25	0.0 – 0.0	00 – 00	0.0 – 0.0
	χ_{Na^+}	0.586 – 0.830	0.00 – 0.00	0.05 – 0.25	0.0 – 0.0	00 – 00	0.0 – 0.0
	χ_{Cl^-}	0.564 – 0.972	0.00 – 0.00	0.00 – 0.00	0.0 – 0.0	00 – 00	0.0 – 0.0
	$2\chi_{SO_4^{2-}}$	0.050 – 0.114	0.00 – 0.00	0.00 – 0.00	-1.0 – -1.0	00 – 00	0.0 – 0.0
	$\chi_{Re}.10^9$	0.000 – 0.000	0.00 – 0.00	0.10 – 7.50	-1.0 – -0.2	25 – 37	0.0 – 0.0
	χ_{ALK}	0.000 – 0.122	0.40 – 0.40	0.50 – 0.50	1.0 – 1.0	00 – 00	0.0 – 0.0
	χ_{DIC}	0.000 – 0.122	0.20 – 0.20	0.00 – 0.00	0.0 – 0.0	01 – 01	1.0 – 1.0
Scenario KH-2. Ratios relative to sum of $\chi_{Ca^{2+}}$, $\chi_{Mg^{2+}}$, χ_{Na^+}, $\chi_{SO_4^{2-}}$, and χ_{DIC} in eq/eq.	$2\chi_{Ca^{2+}}$	0.007 – 0.059	0.33 – 0.66	0.10 – 0.50	0.0 – 0.0	00 – 00	0.0 – 0.0
	$2\chi_{Mg^{2+}}$	0.126 – 0.178	0.00 – 0.33	0.10 – 0.50	0.0 – 0.0	00 – 00	0.0 – 0.0
	χ_{Na^+}	0.618 – 0.750	0.00 – 0.00	0.10 – 0.50	0.0 – 0.0	00 – 00	0.0 – 0.0
	χ_{Cl^-}	0.598 – 0.886	0.00 – 0.00	0.00 – 0.00	0.0 – 0.0	00 – 00	0.0 – 0.0
	$2\chi_{SO_4^{2-}}$	0.054 – 0.106	0.00 – 0.00	0.00 – 0.00	1.0 – 1.0	00 – 00	0.0 – 0.0
	$\chi_{Re}.10^9$	0.000 – 0.000	0.00 – 0.00	0.20 – 15.0	0.2 – 1.0	25 – 37	0.0 – 0.0
	χ_{ALK}	0.000 – 0.126	0.66 – 0.66	1.00 – 1.00	-1.0 – -1.0	00 – 00	0.0 – 0.0
	χ_{DIC}	0.000 – 0.126	0.33 – 0.33	0.00 – 0.00	0.0 – 0.0	01 – 01	1.0 – 1.0

Values are the ranges for uniform distributions normalized to $\chi_{\Sigma^+ + ALK + DIC}$ or $\chi_{\Sigma^+ + SO_4^{2-} + DIC}$. Precipitation is calculated from the Na^+-normalized precipitation end-member in Burke and others (2018). The carbonate and silicate end-members are generic. Negative values for the FeS_2 end-member reflects that FeS_2 oxidation increases $\chi^{riv}_{SO_4^{2-}}$ and χ^{riv}_{Re} while decreasing χ^{riv}_{ALK}. The χ_{Re}/χ_{DIC} ratio is from Horan and others (2019); we estimated normalized χ_{Re} for the FeS_2 and silicate end-members using the $[Re]/[SO_4^{2-}]$ and [Re]/[Na] ranges plotted for the 'sulfides' and 'silicates' regions in figure 4B of that work. MEANDIR samples the normalized Re distributions as log-uniform distributions. These assignments for relative χ_{Re} abundance should be viewed only as approximations meant to illustrate MEANDIR's ability to quantify C_{org} oxidation.

can be demonstrated. Fourth, unlike the full analysis of Horan and others (2019), our analysis does not account for the production or burial of modern organic carbon. That is, our inversion is based only on the river water chemistry and does not consider carbon burial in floodplains or marine sediments.

Sensitivity of Results to Sample Matching or Lowest Misfit Fraction

The sensitivity of model results to changes in the fraction of retained simulations is demonstrated using scenario JG99-1, an inversion of the data from Gaillardet and others (1999) where nearly all simulation results are initially accepted (fig. 2; table 5). We calculate changes in the median fractional contribution of the carbonate end-member to $\chi^{riv}_{Ca^{2+}}$, $f^{carb}_{Ca^{2+}}$, resulting from either changing the permissible fractional difference between inversion results and observations or from considering only a fraction of simulations with the lowest misfit between inversion results and observations. Overall, imposing a selection criterion based on either sample matching or lowest misfit fraction generates large changes in the median value of $f^{carb}_{Ca^{2+}}$ (fig. 2A). For the Rhone River sample, which was selected as an example for illustrative purposes, the median value of $f^{carb}_{Ca^{2+}}$ shifts from 0.26 to 0.86 when constraining results to only those simulations that reconstruct between 85% and 118% of all river observations (fig. 2B). Likewise, the median value of $f^{carb}_{Ca^{2+}}$ shifts from 0.26 to 0.94 when only retaining the 5% of simulations with lowest misfit between inversion results and observations (fig. 2C). These 60 to 68% absolute

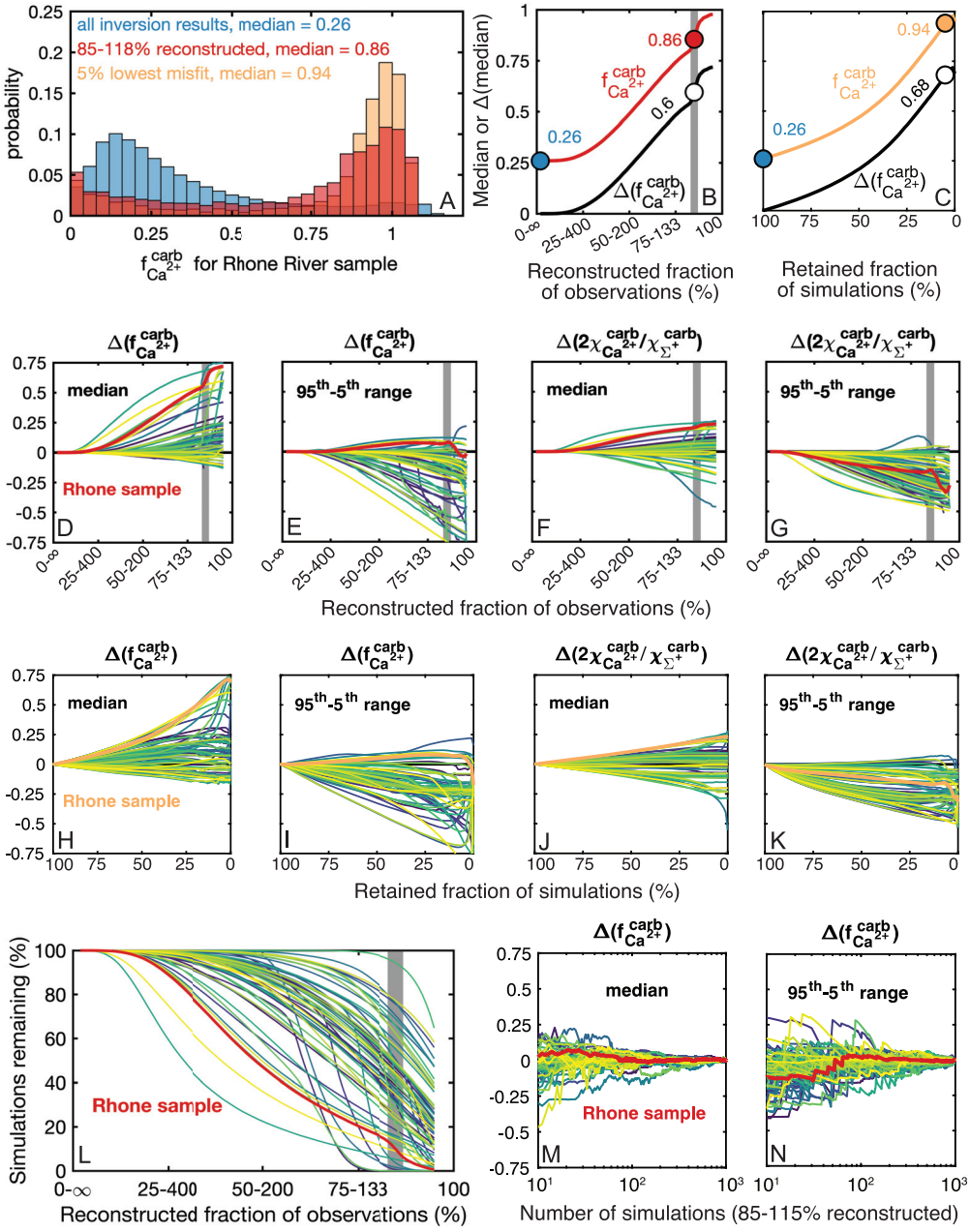

Fig. 2. Sensitivity analysis based on (A-L) scenario JG-1 and (M, N) scenario JG-2. Overall, this analysis shows that the inversion results change when isolating the simulations that reconstruct observations to within a specified fraction or which have low misfit from observations, but that the results are only minimally sensitive to small changes in the specific constraints imposed. (A) Distributions of $f^{carb}_{Ca^{2+}}$, the fraction of $\chi^{riv}_{Ca^{2+}}$ from the carbonate end-member, for a sample from the Rhone River. Results are plotted for all simulations (blue distribution), results where 85 to 118% of all observations ($\chi^{riv}_{Ca^{2+}}$, $\chi^{riv}_{Mg^{2+}}$, $\chi^{riv}_{Na^{+}}$, $\chi^{riv}_{Cl^{-}}$) are reconstructed (red distribution), and results for the 5% of simulations with the lowest misfit between model results and observations (orange distribution). (B) Median of the $f^{carb}_{Ca^{2+}}$ distribution and change in the median of the $f^{carb}_{Ca^{2+}}$ distribution ($\Delta f^{carb}_{Ca^{2+}}$) when only retaining results where all observations are reconstructed within the indicated range

legend/caption continues on the next page

changes in the inversion-constrained contribution of the carbonate end-member to $\chi^{riv}_{Ca^{2+}}$ would have substantial implications for the interpretation of inversion results.

Across most samples from Gaillardet and others (1999), the median value of $f^{carb}_{Ca^{2+}}$ increases and the inversion-constrained range in $f^{carb}_{Ca^{2+}}$ ($95^{th} - 5^{th}$ percentile) decreases with more stringent selection criteria (figs. 2D, E, H, and I). Moreover, the inversion-constrained range of carbonate $2\chi^{carb}_{Ca^{2+}}/\chi^{carb}_{\Sigma^{+}}$ also generally decreases with tighter sample matching criteria (fig. 2G) or with a lower fraction of retained simulations (fig. 2K).

To constrain the sensitivity of inversion results to the number of successful simulations, we also quantify changes in the fractional contribution of the carbonate end-member with changes in the number of simulations satisfying an imposed sample matching criteria (figs. 2M and N). These results, generated from scenario JG-2, show relatively little change in the median $f^{carb}_{Ca^{2+}}$ value or range in $f^{carb}_{Ca^{2+}}$ ($95^{th} - 5^{th}$ percentile range of the inversion-constrained distribution) after about 100 successful simulations.

This sensitivity analysis demonstrates that inversion results change drastically when removing simulations that either fail to recreate river observations or have high misfit from observations. However, the results of JG-1 appear only minimally sensitive to small changes in the specific values of success criteria. For example, results are qualitatively similar when sample matching criteria are 75 to 133% or 80 to 125%. Likewise, results are qualitatively similar when retaining the 2% or 5% of simulations with lowest misfit between model results and observations. In MEANDIR, the choice of how to subsample inversion results is left to the user.

Median Fractional Contributions to Dissolved Variables

Values of f^{s}_{i} for carbonate, silicate, and evaporite end-members show different sensitivities to common choices for inversion parameters (fig. 3). For all dissolved variables, the fractional contributions of the carbonate and silicate end-members are relatively consistent among scenario JG-2 and either scenario JG-3 (uniform end-member distributions; figs. 3A and B), scenario JG-4 ($\chi_{Na^{+}}$ normalization; figs. 3E and F) or scenario JG-5 (absolute cost function; figs. 3I and J). For these scenarios the agreement of median fractional contributions from silicate and carbonate end-members is often within 10% and frequently within 25% (fig. 3 gray shading). For any individual sample the differences in the median f^{carb}_{i} or f^{slct}_{i} values between scenarios tend to be smaller or comparable to the range in simulation results. Conversely, the fractional differences among median evaporite contributions tend to be larger (figs. 3C, G, and K). In particular, values of $f^{evap}_{Na^{+}}$ and $f^{evap}_{Cl^{-}}$ in scenario JG-5 are generally lower than in scenario JG-2 (fig. 3K), with the difference taken up by higher values of $f^{prec}_{Na^{+}}$ and $f^{prec}_{Cl^{-}}$.

continued

of fractions. (C) Median of the $f^{carb}_{Ca^{2+}}$ distribution and change in the median of the $f^{carb}_{Ca^{2+}}$ distribution when only retaining the indicated fraction of simulations with lowest misfit between inversion results and river observations. (D-G) Results where all observations are reconstructed within the indicated range of fractions. (H-K) Results when only retaining the indicated fraction of simulations with lowest misfit between model results and river observations. (D, H) Change in the median $f^{carb}_{Ca^{2+}}$, (E, I) 95^{th}-5^{th} percentile range in $f^{carb}_{Ca^{2+}}$, (F, J) median $\chi^{carb}_{Ca^{2+}}/\chi^{carb}_{\Sigma^{+}}$, and (G, K) 95^{th}-5^{th} percentile range in $\chi^{carb}_{Ca^{2+}}/\chi^{carb}_{\Sigma^{+}}$. (L) The fraction of simulations remaining when only retaining results where all observations are reconstructed within the indicated range of fractions. For all samples, fewer simulations are retained as the imposed constraint tightens. Change in the (M) median of $f^{carb}_{Ca^{2+}}$ and (N) change in the 95^{th}-5^{th} percentile of $f^{carb}_{Ca^{2+}}$ with increasing number of simulations, where all simulations reconstruct between 85% and 115% of each observation. Values in (M) and (N) are given relative to the values at 1000 successful simulations. The sample from the Rhone River is highlighted (D-G, L-N) in red or (H-K) in orange. The grey vertical bar (B, D – G, L) is centered at sample matching criteria of 85 to 118%, very similar to the 85 to 115% criteria used in most of the scenarios in this analysis. All data underlying these inversion results are from Gaillardet and others (1999).

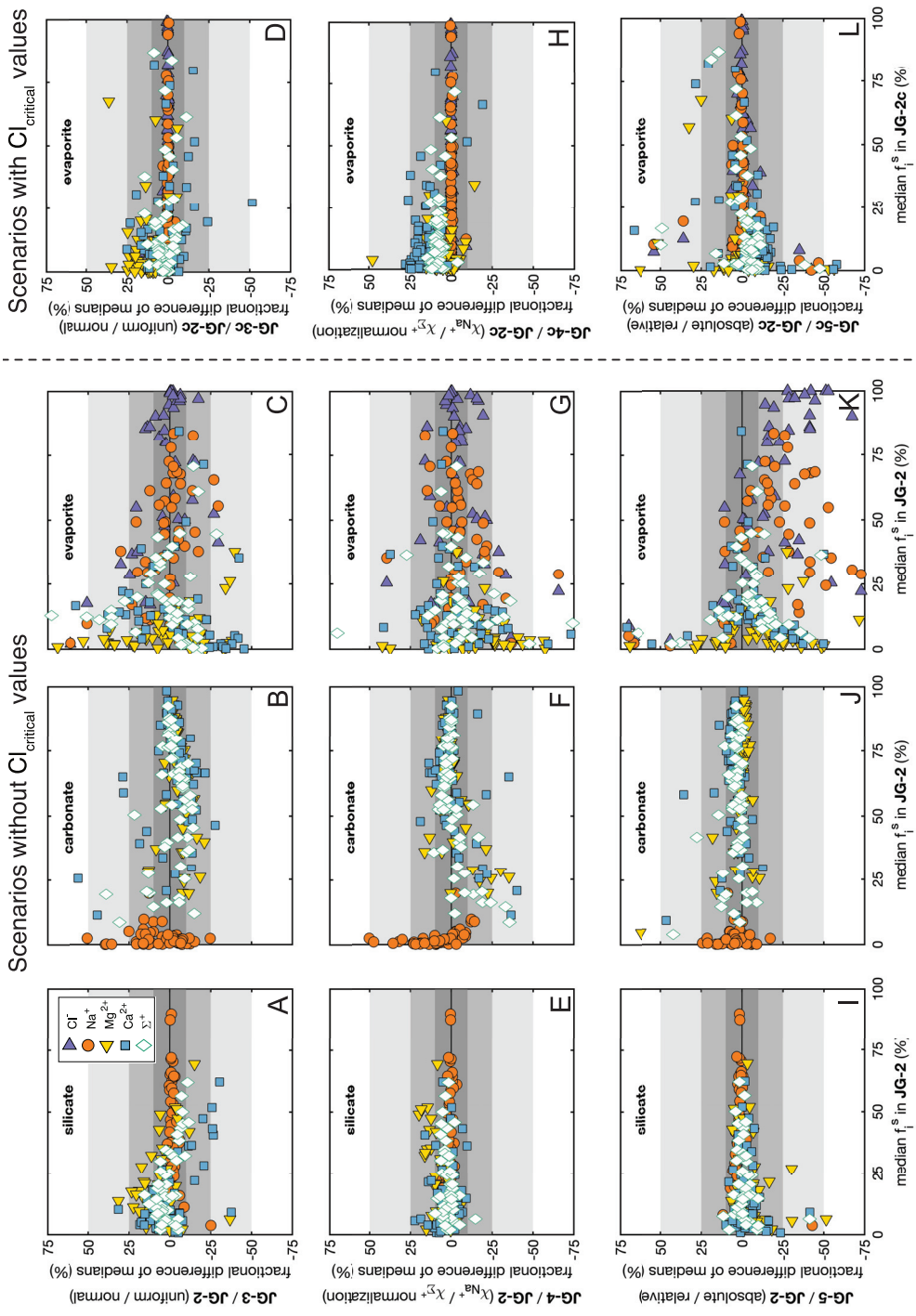

legend/caption continues on the next page

The disagreement of $f^{evap}_{Na^+}$ and $f^{evap}_{Cl^-}$ among JG-2 and the other scenarios reflects that simulations satisfying sample matching criteria can be found when the majority of $\chi^{riv}_{Cl^-}$ is sourced from either evaporite or from precipitation, such that changes in the scenario parameters alter which end-member is calculated to make the larger contribution to river dissolved load. Lacking a robust chemical basis for differentiating precipitation from evaporites, the inversion-constrained median $f^{evap}_{Na^+}$ and $f^{evap}_{Cl^-}$ values can easily shift. In general, identification of a chemical tracer distinguishing precipitation from evaporite inputs would greatly aid inversion models.

Applying values of $\chi^{riv}_{Cl^-\ critical}$ addresses this problem by explicitly assigning $f^{prec}_{Cl^-}$, which also uniquely defines $f^{evap}_{Cl^-}$ because in these scenarios only the precipitation and evaporite end-members have non-zero values of $\chi^{s}_{Cl^-}$ (table 7). When $\chi^{riv}_{Cl^-\ critical}$ values are implemented, the four scenarios are in stronger agreement for the fraction of each element sourced from each end-member (figs. 3D, H, and L). $\chi^{riv}_{Cl^-\ critical}$ values are thus a valuable tool for partitioning $\chi^{riv}_{Cl^-}$ between precipitation and evaporite end-members.

Distributions of the Sum of Fractional Contributions in Successful Simulations

Inversion models can produce results that only poorly recreate observations of river dissolved load. To demonstrate the problem, we consider distributions of the sum of inversion-constrained fractional contributions from all end-members ($\Sigma^n_s[f^s_i]$) (fig. 4). In the case that inversion results perfectly match observations, the sum of fractional contributions from all end-members would equal 100%. In scenario MT-1 (relative cost function) and scenario MT-2 (absolute cost function) distributions of $\Sigma^n_s\left[f^s_{Ca^{2+}}\right]$ (fig. 4A), $\Sigma^n_s\left[f^s_{Mg^{2+}}\right]$ (fig. 4B), $\Sigma^n_s\left[f^s_{Na^+}\right]$ (fig. 4C), and $\Sigma^n_s[f^s_{Cl^-}]$ (fig. 4D) are all constrained between 85% and 115%. Within this range, however, more values of $\Sigma^n_s\left[f^s_{Ca^{2+}}\right]$ and $\Sigma^n_s\left[f^s_{Mg^{2+}}\right]$ are close to 100% in scenario MT-2 than in scenario MT-1 (figs. 4A and B). The distribution of $\Sigma^n_s\left[f^s_{Na^+}\right]$ is similar for the two scenarios (fig. 4C), and the distribution of $\Sigma^n_s[f^s_{Cl^-}]$ in scenario MT-1 has more values close to 100% than in MT-2 (fig. 4D).

These differences reflect whether the scenario uses a cost function based on absolute misfit or relative misfit. In the former case, variables with higher normalized values are reconstructed with higher proportional fits than variables with lower normalized values. In the latter case, variables with low normalized ratios exert a relatively stronger influence on the cost function and equalize proportional misfit across observations. Because most samples have $\chi^{riv}_{Ca^{2+}} > \chi^{riv}_{Na^+} > \chi^{riv}_{Cl^-}$, results from scenario MT-2 have $\Sigma^n_s\left[f^s_{Ca^{2+}}\right]$ values near 100% but a large range in $\Sigma^n_s[f^s_{Cl^-}]$ values. Following the same logic, we would expect results from scenario MT-1 to show similar ranges in

continued

Fig. 3. Comparison of median fractional contributions in scenarios JG-3 and JG-3c (uniform end-member distributions), JG-4 and JG-4c (normalization to χ_{Na^+}), JG-5 and JG-5c (absolute cost function) relative to scenarios JG-2 and JG-2c (normal end-member distribution, normalization to χ_{Σ^+}, relative cost function) for the (A, E, I) silicate, (B, F, J) carbonate, and (C, D, G, H, K, L) evaporite end-members. Median contributions are plotted for $\chi^{riv}_{Cl^-}$ (purple right-pointing triangles), $\chi^{riv}_{Na^+}$ (orange circles), $\chi^{riv}_{Mg^{2+}}$ (yellow left-pointing triangles), $\chi^{riv}_{Ca^{2+}}$ (blue square), and $\chi^{riv}_{\Sigma^+}$ (green diamonds), in scenarios (A-C, E-G, I-K) without $\chi^{riv}_{Cl^-\ critical}$ values and (D, H, L) with $\chi^{riv}_{Cl^-\ critical}$ values. Overall, median f^{carb}_i and f^{slct}_i values are similar across scenarios while median f^{evap}_i values are only similar when comparing observations inverted using $\chi^{riv}_{Cl^-\ critical}$ values. Samples are plotted when either of the two median f^s_i values exceed 0.1%. Shading indicates proportional differences of 10%, 25%, and 50%. All data underlying these inversion results are from Gaillardet and others (1999).

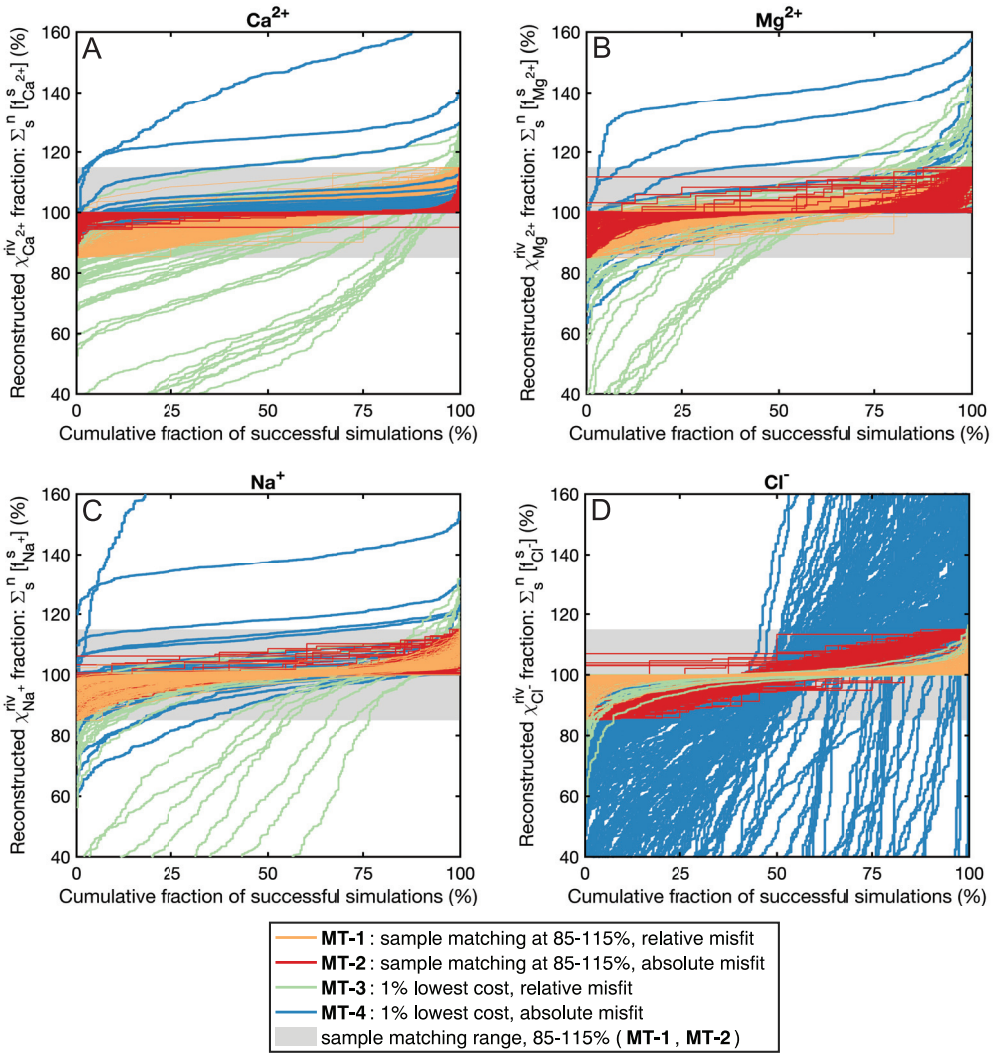

Fig. 4. Distributions of the fraction of reconstructed river observations. Each curve shows the cumulative distribution, for a single sample in one of four color-coded scenarios, of the summed fractional contributions from all end-members in accepted simulations. (A) $\Sigma_s^n\left[f_{Ca^{2+}}^s\right]$, (B) $\Sigma_s^n\left[f_{Mg^{2+}}^s\right]$, (C) $\Sigma_s^n\left[f_{Na^+}^s\right]$, and (D) $\Sigma_s^n\left[f_{Cl^-}^s\right]$. Results are shown for scenario MT-1 (orange, default scenario using relative cost function), MT-2 (red, using an absolute cost function), MT-3 (green, best 1% of simulations solved with a relative cost function) and MT-4 (blue, best 1% of simulations solved with an absolute cost function). Scenarios MT-1 and MT-2 are constrained to reconstruct between 85% and 115% of all observations (gray shaded region), while scenarios MT-3 and MT-4 are not constrained to generate results within a particular fraction of observed values. In MT-3 and MT-4 the lack of explicit sample matching criteria allows for results that disagree with observations; this misfit is exemplified by the wide range of $\Sigma_s^n\left[f_{Cl^-}^s\right]$ values in MT-4. Most samples in scenario MT-1 have 300 successful simulations, 75% of samples in MT-2 have at least 100 successful simulations, and all samples in scenarios MT-3 and MT-4 have 300 successful simulations (1% of 30,000 simulations). In all scenarios the fractional contribution of each end-member to χ_{norm} is constrained between 0 and 1. All data underlying these inversion results are from Torres and others (2016).

$\Sigma_s^n\left[f_{Ca^{2+}}^s\right]$ and $\Sigma_s^n[f_{Cl^-}^s]$. However, the results of MT-1 instead show that $\Sigma_s^n[f_{Cl^-}^s]$ values are typically closer to 100% than values of $\Sigma_s^n\left[f_{Ca^{2+}}^s\right]$ in the same scenario (figs. 4A and D). This difference from expectations potentially reflects that, while $\chi_{Cl^-}^{riv}$ is

sourced from only a single end-member in scenarios MT-1 through MT-4, multiple end-members contribute to $\chi^{riv}_{Ca^{2+}}$ and may introduce additional variability to $\Sigma^n_s\left[f^s_{Ca^{2+}}\right]$.

Successful results in scenarios MT-3 (relative cost function) and MT-4 (absolute cost function) are the 1% of simulations for each sample with the lowest misfit between model results and observations, without the explicit sample matching requirement of scenarios MT-1 and MT-2. In scenario MT-3 several samples have values for $\Sigma^n_s\left[f^s_{Ca^{2+}}\right]$, $\Sigma^n_s\left[f^s_{Mg^{2+}}\right]$, and $\Sigma^n_s\left[f^s_{Na^{+}}\right]$ substantially offset from 100% while values of $\Sigma^n_s[f^s_{Cl^-}]$ are close to 100%. Conversely, in scenario MT-4 most results have values for $\Sigma^n_s\left[f^s_{Ca^{2+}}\right]$, $\Sigma^n_s\left[f^s_{Mg^{2+}}\right]$, and $\Sigma^n_s\left[f^s_{Na^{+}}\right]$ near 100% while very few values of $\Sigma^n_s[f^s_{Cl^-}]$ are close to 100% (fig. 4D). These results are similar to those from MT-1 and MT-2, where the scenario using a proportional cost function is better able to recreate variables at low relative abundance.

Overall, this analysis demonstrates that selecting a small fraction of simulations with the lowest misfit between results and observations does not necessarily produce results consistent with dissolved river chemistry. Rather, using explicit sample matching criteria produces results consistent with observations, and using a proportional cost function helps to model observations at low relative abundance. For most applications, MT-1 (sample matching with relative misfit) is thus our favored choice among the four scenarios considered in this section.

Distributions of Constrained End-member Chemistry

The distributions of end-member chemical ratios in successful inversions can differ substantially from the initial distributions (fig. 5). To demonstrate these changes we consider the initial and final distributions of $2\chi^{carb}_{Mg^{2+}}/\chi^{carb}_{\Sigma^+}$ and $2\chi^{carb}_{Mg^{2+}}/\chi^{carb}_{Na^+}$ in inversions of the global river data of Gaillardet and others (1999) (scenarios JG-2, JG-3, JG-4, and JG-6) (figs. 5A-F) and distributions of $2\chi^{dolo}_{Mg^{2+}}/\chi^{dolo}_{\Sigma^+}$ and $2\chi^{dolo}_{SO^{2-}_4}/\chi^{dolo}_{\Sigma^+}$ in inversions of the river samples of Torres and others (2016) (scenario MT-1 and MT-3) (figs. 5G–I). Regardless of whether the initial distribution of end-member chemistry is normal (fig. 5A), uniform (fig. 5B), or normalized with χ_{Na^+} rather than χ_{Σ^+} (fig. 5D), the final distributions are typically distinct from the initial distributions. Moreover, inversion-constrained distributions of end-member chemistry can be relatively insensitive to whether the initial distribution is normal or uniform; on a percentile-percentile cross plot of $2\chi^{carb}_{Mg^{2+}}/\chi^{carb}_{\Sigma^+}$ in scenarios JG-2 and JG-3, most of the point density occurs close to a 1:1 line (fig. 5C). However, we note that the shape of the initial end-member distribution may have a larger impact on the final end-member distributions when only accepting a fraction of simulations with lowest misfit because the distributions of misfit may differ between the various scenarios. We also consider results when each sample is presented with the same set of end-members and the best 1% of simulations, as evaluated across all samples, is retained (fig 5E). In this case the distributions of end-member chemistry collapse to a single set of values. There are then large differences between this final distribution and those in a scenario where each sample defines its own distribution of end-member chemical ratios (fig. 5F).

In the river water samples of Torres and others (2016), inversion-constrained $2\chi^{dolo}_{Mg^{2+}}/\chi^{dolo}_{\Sigma^+}$ (fig. 5G) and $2\chi^{dolo}_{SO^{2-}_4}/\chi^{dolo}_{\Sigma^+}$ (fig. 5H) identify chemical gradients across sampling site. Median $2\chi^{dolo}_{SO^{2-}_4}/\chi^{dolo}_{\Sigma^+}$ values are higher in samples from Mountain-1 and Mountain-2 than in samples from the Mountain-Front, which in turn are higher than in samples from the Foreland-floodplain. These results demonstrate that, when

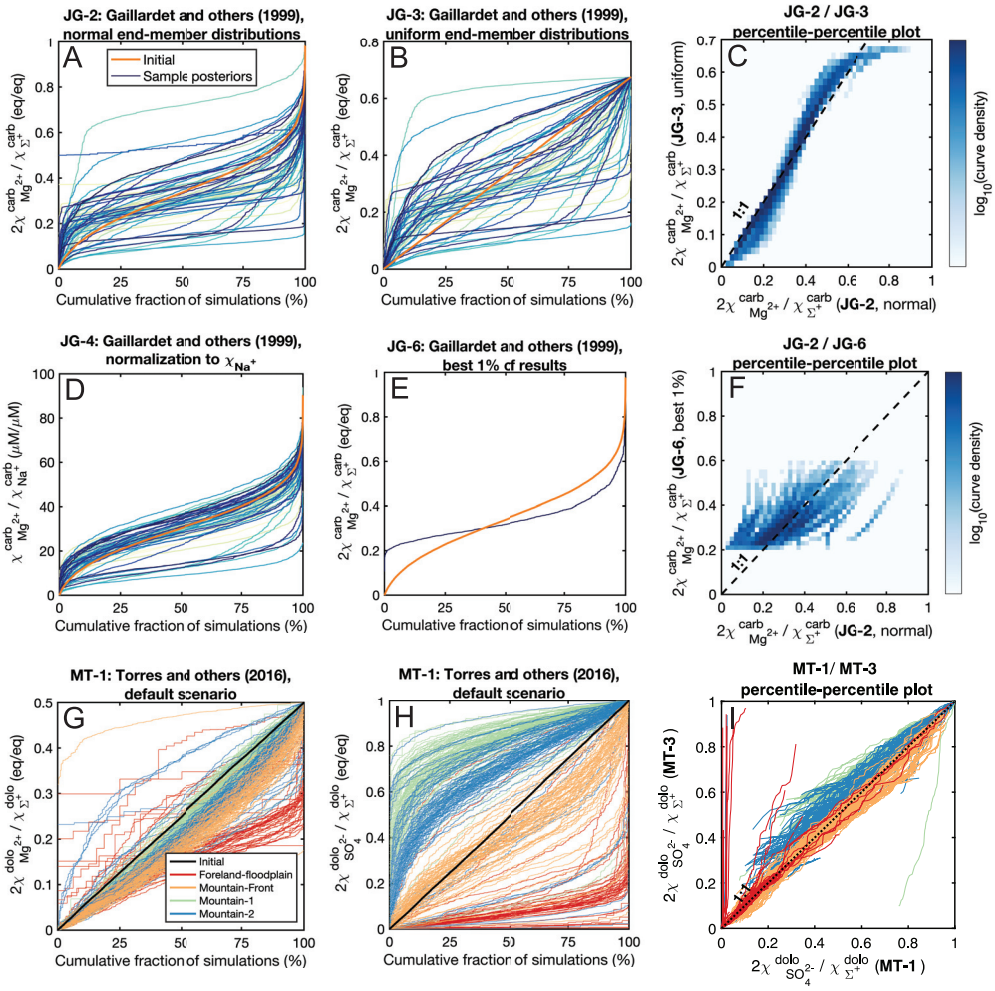

Fig. 5. Inversion-constrained end-member chemistry calculated using the data from (A-F) Gaillardet and others (1999) or (G-I) Torres and others (2016). In (A, B, D, E, G, H) each curve shows the cumulative distribution, for a single sample, of either $2\chi^{carb}_{Mg^{2+}}/\chi^{carb}_{\Sigma^+}$, $2\chi^{carb}_{Mg^{2+}}/\chi^{carb}_{Na^+}$, $2\chi^{dolo}_{Mg^{2+}}/\chi^{dolo}_{\Sigma^+}$, or $2\chi^{dolo}_{SO_4^{2-}}/\chi^{dolo}_{\Sigma^+}$. In (A, B, D) different colors reflect individual samples, and in (G, H) samples are color-coded by site of collection. (A) The distributions of end-member chemistry in successful simulations of scenario JG-2 differ from the initial distribution. Differences are also found for (B) scenario JG-3 (uniform end-member distributions) and (D) scenario JG-4 (normalization to χ_{Na^+}). (E) In scenario JG-6 (best 1% of simulation results, as evaluated across all samples), the final distribution is a set of values distinct from the initial distribution. (C, F) Curve density of percentile-percentile plots for the results of scenarios JG-2, JG-3, and JG-6. The curve density is elevated near the 1:1 line when comparing (C) JG-2 and JG-3 but is away from 1:1 line when comparing (F) JG-2 and JG-6. (G, H) In the data from Peru, the distributions of $2\chi^{dolo}_{Mg^{2+}}/\chi^{dolo}_{\Sigma^+}$ and $2\chi^{dolo}_{SO_4^{2-}}/\chi^{dolo}_{\Sigma^+}$ in successful simulations coherently vary with sampling location. (I) Distributions of inversion-constrained end-member ratios are similar in scenarios MT-1 and MT-3.

there are large chemical gradients across the sampling region, inversion-constrained distributions can be used to interrogate spatial changes in the composition of weathering lithologies. Lastly, comparison of end-member chemistry in scenarios MT-1 and MT-3 suggest minimal sensitivity to whether results are subsampled on the basis of sample matching or lowest misfit fraction (fig. 5I).

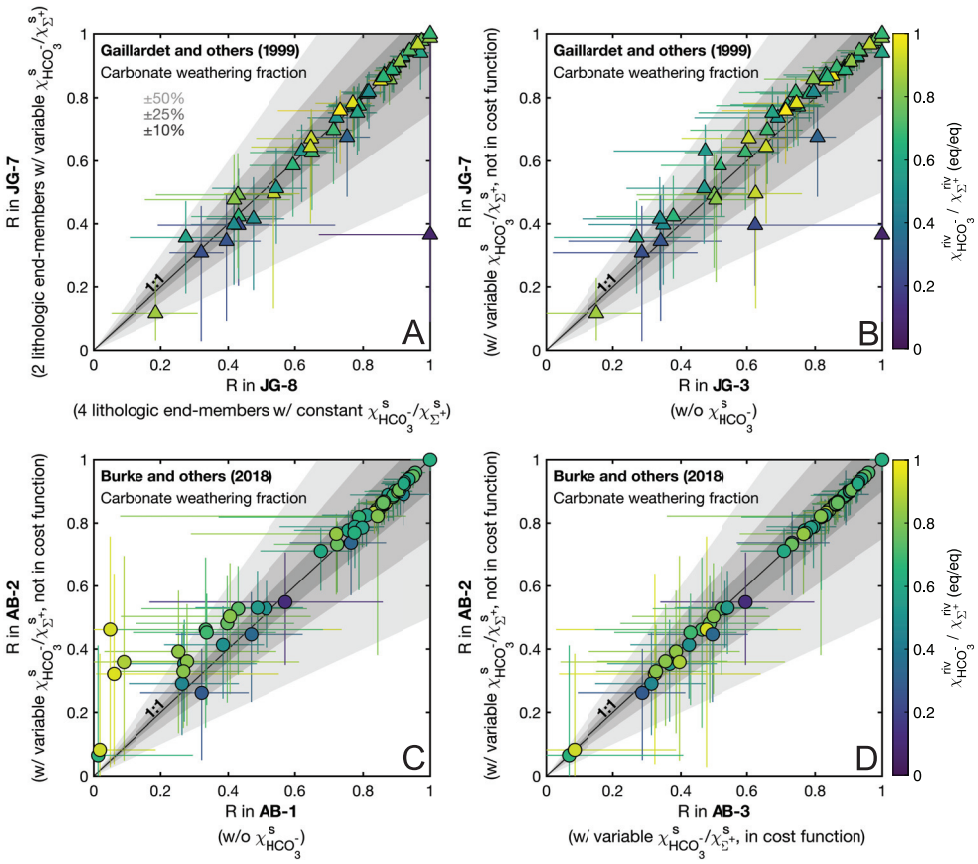

Fig. 6. Carbonate weathering fraction (R) when including $\chi^{riv}_{HCO_3^-}$ in inversions of data from (A, B) Gaillardet and others (1999) and (C, D) Burke and others (2018). (A) R is similar when calculated using two end-members with variable $\chi^{s}_{HCO_3^-}/\chi^{s}_{\Sigma^+}$ ratios or when calculated using 4 end-members with fixed $\chi^{s}_{HCO_3^-}/\chi^{s}_{\Sigma^+}$ ratios (Blattman and others, 2019). (B, C) R is generally similar with and without $\chi^{riv}_{HCO_3^-}$. At particularly high or low ratios of $\chi^{riv}_{HCO_3^-}/\chi^{riv}_{\Sigma^+}$, including $\chi^{riv}_{HCO_3^-}$ in the inversion results in higher values of R in samples with elevated ratios and lower values of R in samples with lower ratios. (D) R is similar when $\chi^{riv}_{HCO_3^-}/\chi^{riv}_{\Sigma^+}$ is included or excluded from the cost function. Plotted points are the medians of accepted simulations, error bars extend from the 25th to 75th percentiles of accepted results, and shading indicates proportional differences of 10%, 25%, and 50%.

Including $\chi^{riv}_{HCO_3^-}$ in River Inversion Models

Inversion-constrained distributions of R are similar between scenario JG-7, where $\chi^{carb}_{HCO_3^-}/\chi^{carb}_{\Sigma^+}$ and $\chi^{slct}_{HCO_3^-}/\chi^{slct}_{\Sigma^+}$ take on variable values, and JG-8, where two carbonate and two silicate end-members each have fixed $\chi^{s}_{HCO_3^-}/\chi^{s}_{\Sigma^+}$ ratios (fig. 6A; table 5). In general, including $\chi^{riv}_{HCO_3^-}$ in the inversion, such as in JG-7, has only a small impact on R when compared to an inversion without $\chi^{riv}_{HCO_3^-}$, such as JG-3 (fig. 6B). Likewise, results of scenarios AB-1 and AB-2 also indicate that R is generally insensitive to inclusion of $\chi^{riv}_{HCO_3^-}$ (fig. 6C). However, samples with particularly low or high values of $\chi^{riv}_{HCO_3^-}/\chi^{riv}_{\Sigma^+}$ may display changes in R when $\chi^{riv}_{HCO_3^-}$ is included in the inversion. For example, two to three samples from Gaillardet and others (1999) plot with lower values of R and three samples from Burke and others (2018) plot at higher values of R

when accounting for $\chi^{riv}_{HCO_3^-}$ (figs. 6B and C). Notably, the samples showing these changes exhibit large ranges in simulation results. One possible reason for the shifted distribution of R is that scenarios JG-3 and AB-1, where $\chi^{riv}_{HCO_3^-}$ is not included in the inversions, do not require MEANDIR to generate results within 15% of $\chi^{riv}_{HCO_3^-}$ in order to meet the sample matching criteria. When $\chi^{riv}_{HCO_3^-}$ is included in the inversion, as in JG-7 and AB-2, samples with low $\chi^{riv}_{HCO_3^-}/\chi^{riv}_{\Sigma^+}$ can be inconsistent with majority carbonate input and require a larger influence from silicate weathering while samples with high $\chi^{riv}_{HCO_3^-}/\chi^{riv}_{\Sigma^+}$ require additional carbonate inputs. Our results demonstrate that including $\chi^{riv}_{HCO_3^-}$ generally does not change results, but that doing so may add meaningful constraint for samples with particularly high or low values of $\chi^{riv}_{HCO_3^-}/\chi^{riv}_{\Sigma^+}$.

In the samples of Burke and others (2018), $\chi^{riv}_{HCO_3^-}$ is calculated by charge balance using reported major element concentrations. As discussed above, including $\chi^{riv}_{HCO_3^-}$ derived from charge balance accounts to adding degenerate information into the inversion when all constituent mass balance equations are also included. Users of MEANDIR can decide whether to exclude model misfit of $\chi^{riv}_{HCO_3^-}$ from the cost function. For scenarios AB-2 and AB-3, R values are similar when $\chi^{riv}_{HCO_3^-}$ is included or excluded from the cost function (fig. 6D).

Quantifying Formation of Secondary Phases

Icelandic river water samples from Gíslason and others (1996) are elevated in $2\chi^{riv}_{Ca^{2+}}/\chi^{riv}_{\Sigma^+}$ and $\chi^{riv}_{Na^+}/\chi^{riv}_{\Sigma^+}$ relative to expectations from conservative mixing between basalt and precipitation (fig. 7A). Multiple explanations of this discrepancy exist, including variable bedrock chemistry and seasonal changes in the chemistry of precipitation, but a substantial role for clay formation is supported by numerous studies across isotopic systems (Georg and others, 2007; Vigier and others, 2009; Hindshaw and others, 2013; Kemeny and others, 2021b). Assuming basalt and precipitation are the sole solute sources, we use MEANDIR to determine the chemical composition of the secondary clay phase that would be necessary to produce the river observations. We then compare this calculated value to solid-phase measurements of clay-rich soil/sediment samples from Iceland as a test of MEANDIR's ability to simulate clay formation.

MEANDIR finds that the river observations of Gíslason and others (1996) can be generated through formation of a secondary clay with low median $\chi^{clay}_{Na^+}/\chi^{clay}_{\Sigma^+}$ (figs. 7B and C). The inversion-constrained distribution of $2\chi^{clay}_{Mg^{2+}}/\chi^{clay}_{\Sigma^+}$ (fig. 7B, blue) is elevated from $2\chi^{clay}_{Ca^{2+}}/\chi^{clay}_{\Sigma^+}$ (fig. 7B, yellow), which is elevated from $\chi^{clay}_{Na^+}/\chi^{clay}_{\Sigma^+}$ (fig. 7B, red). The average median value of $2\chi^{clay}_{Ca^{2+}}/\chi^{clay}_{\Sigma^+}$ is 0.34, $2\chi^{clay}_{Mg^{2+}}/\chi^{clay}_{\Sigma^+}$ is 0.57, and $\chi^{clay}_{Na^+}/\chi^{clay}_{\Sigma^+}$ is 7% (fig. 7C). Despite the initial distribution of the clay end-member in scenario SG-1 being quite general (table 11), the chemical composition of the inversion-constrained secondary product is consistent with observations of Icelandic clay chemistry. Moulton and others (2000) report $2\chi^{clay}_{Ca^{2+}}/\chi^{clay}_{\Sigma^+}$ of 0.44, $2\chi^{clay}_{Mg^{2+}}/\chi^{clay}_{\Sigma^+}$ of 0.44, and $\chi^{clay}_{Na^+}/\chi^{clay}_{\Sigma^+}$ of 12% for the finest fraction of soils from Skorradalur (uncorrected for possible Cl^- contributions; Stefánsson and Gíslason (2001)), and Thorpe and others (2019) report $2\chi^{clay}_{Ca^{2+}}/\chi^{clay}_{\Sigma^+}$ ranging from 0.43 to 0.58, $2\chi^{clay}_{Mg^{2+}}/\chi^{clay}_{\Sigma^+}$ ranging from 0.32 to 0.49, and $\chi^{clay}_{Na^+}/\chi^{clay}_{\Sigma^+}$ ranging from 0.08 to 0.10 in the < 2 μm fraction of Hvítá River sediments (fig. 7C, shaded patches). MEANDIR's prediction of a low $\chi^{clay}_{Na^+}/\chi^{clay}_{\Sigma^+}$ ratio and elevated ratios of $2\chi^{clay}_{Ca^{2+}}/\chi^{clay}_{\Sigma^+}$ and $2\chi^{clay}_{Mg^{2+}}/\chi^{clay}_{\Sigma^+}$ approximately

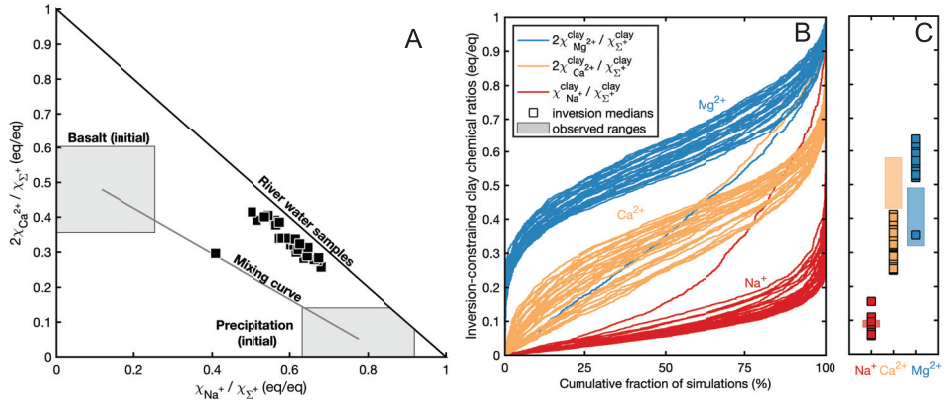

Fig. 7. Constraining the chemical composition of secondary clay. (A) Observations of $2\chi^{riv}_{Ca^{2+}}/\chi^{riv}_{\Sigma^+}$ and $\chi^{riv}_{Na^+}/\chi^{riv}_{\Sigma^+}$ in Icelandic river water samples from Gíslason and others (1996). River water is depleted in $2\chi^{riv}_{Mg^{2+}}/\chi^{riv}_{\Sigma^+}$ relative to the mixing of basalt and precipitation, which has previously been attributed to the formation of secondary clays. Shaded regions for basalt and precipitation are centered on the mean of the initial distributions and extend two standard deviations. (B) Inversion-constrained clay chemistry based on the same river data (scenario SG-1). Each curve shows the cumulative distribution, for a single sample, of inversion-constrained $2\chi^{clay}_{Mg^{2+}}/\chi^{clay}_{\Sigma^+}$ (blue), $2\chi^{clay}_{Ca^{2+}}/\chi^{clay}_{\Sigma^+}$ (yellow), or $\chi^{clay}_{Na^+}/\chi^{clay}_{\Sigma^+}$ (red). (C) The median of each inversion-constrained distribution (squares). Shaded regions indicate the range of clay observations from Thorpe and others (2019).

match these observations. Moreover, the accuracy of the SG-1 scenario could be improved by including the constraints from Moulton and others (2000) or Thorpe and others (2019) in the pre-defined chemical ranges of the secondary phase. However, in many applications secondary phase formation is expected while direct observational constraints of those phases are unavailable. Our results demonstrate that MEANDIR can generate reasonably accurate results for the chemistry of secondary clays even in the absence of direct observational constraints.

Quantifying FeS_2 Oxidation

We evaluate the mutual consistency of three techniques for quantifying the fraction of $\chi^{riv}_{SO_4^{2-}}$ sourced from FeS_2 oxidation. The three techniques are quantifying $\chi^{riv}_{SO_4^{2-}}$ not attributable to evaporites and precipitation ($\chi^{riv}_{excess\ SO_4^{2-}}$, or the "excess SO_4^{2-}" approach; Burke and others, 2018), combining FeS_2 oxidation and end-member weathering ($2\chi^{s}_{FeS_2\ SO_4^{2-}}/\chi^{s}_{\Sigma^+}$ values, or the "SO_4^{2-} in end-members" approach; Torres and others, 2016), and using an independent end-member to represent FeS_2 oxidation ($\chi^{FeS_2\ ox.}_{SO_4^{2-}}$) or inputs of other SO_4^{2-} ($\chi^{other}_{SO_4^{2-}}$) (the "independent SO_4^{2-}-bearing end-member" or "other SO_4^{2-}" approach) (fig. 8). We compare results for scenarios AB-1, AB-4, AB-5, and AB-6 using the data of Burke and others (2018) and scenarios MT-5, MT-6, and MT-7 using the data of Torres and others (2016). In the latter scenarios we also consider the $^{34}S/^{32}S$ ratio of the oxidized FeS_2.

For the data of Burke and others (2018), values of the carbonate weathering fraction R are in mutual agreement for scenarios AB-4 (excess SO_4^{2-}) and AB-5 (independent SO_4^{2-}-bearing end-member) (fig. 8A). As expected, higher values of R

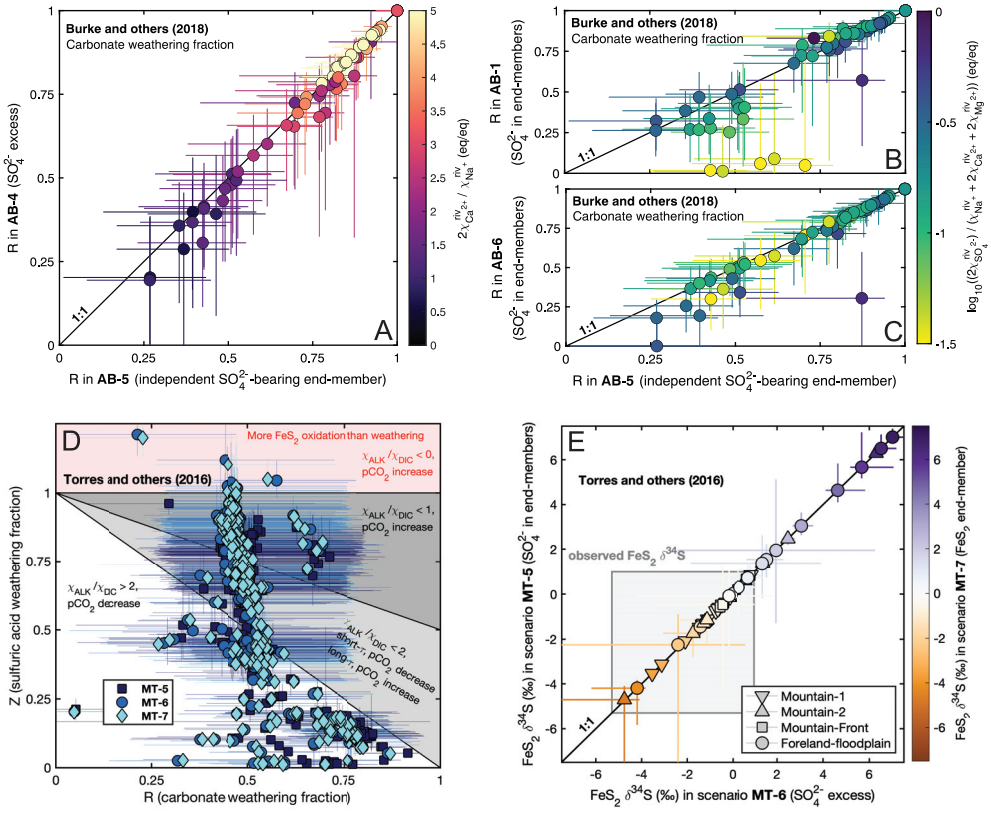

Fig. 8. Influence of different inversion methods on the carbonate weathering fraction R, the sulfuric acid weathering fraction Z, and the $^{34}S/^{32}S$ ratio of $\chi^{riv}_{SO_4^{2-}}$ derived from FeS_2 oxidation, excess SO_4^{2-}, or from other SO_4^{2-}. (A) R values in scenarios AB-4 and AB-5 are in mutual agreement and increase coherently with increasing ratios of $2\chi^{riv}_{Ca^{2+}}/\chi^{riv}_{Na^+}$. (B) R values at low $(2\chi^{riv}_{SO_4^{2-}})/(2\chi^{riv}_{Ca^{2+}}+2\chi^{riv}_{Mg^{2+}}+\chi^{riv}_{Na^+})$ disagree between scenarios AB-1 and AB-5, which we interpret as reflecting a probabilistic artifact arising during the inversion of AB-1. (C) When the carbonate and silicate end-members have a reduced range of possible $2\chi^{s}_{FeS_2\ SO_4^{2-}}/\chi^{s}_{\Sigma^+}$ ratios, as in scenario AB-6, R values in samples with low ratios of $\chi^{riv}_{SO_4^{2-}}$ are in much stronger agreement with R values from AB-5. (D) R and Z values are in mutual agreement for scenarios MT-5 (dark blue squares), MT-6 (blue circles) and MT-7 (light blue diamonds). Note that Z>1 is a natural outcome of MT-6 and MT-7, but not MT-5 (where $2\chi^{s}_{FeS_2\ SO_4^{2-}}/\chi^{s}_{\Sigma^+}\leq 1$). (E) The derived isotopic composition of FeS_2 is very similar among scenarios MT-5, MT-6 and MT-7. Moreover, the lower range of the inversion-constrained values match observations of FeS_2 $\delta^{34}S$ (Torres and others, 2016). Samples with values of FeS_2 $\delta^{34}S$ higher than the observed range are predominantly from the Foreland-floodplain and may reflect inputs of sedimentary lithologies that are not included in the inversion, such as evaporites. Notably, observed values of FeS_2 $\delta^{34}S$ were not included in the inversion to constrain the possible range of FeS_2 $\delta^{34}S$ values. Plotted points are the medians of accepted inversion results and error bars extend from the (A, B, C) 25th to 75th percentiles of accepted results or the (D, E) 5th to 95th percentiles of accepted results.

occur at higher values of $2\chi^{riv}_{Ca^{2+}}/\chi^{riv}_{Na^+}$. Conversely, R values disagree between scenarios AB-5 (independent SO_4^{2-}-bearing end-member) and AB-1 (SO_4^{2-} in end-members) in a subset of samples with low values of $2\chi^{riv}_{SO_4^{2-}}/\left(2\chi^{riv}_{Ca^{2+}}+2\chi^{riv}_{Mg^{2+}}+\chi^{riv}_{Na^+}\right)$ (fig. 8B). Median values of R in scenario AB-1 do not increase coherently with $2\chi^{riv}_{Ca^{2+}}/\chi^{riv}_{Na^+}$, suggesting a previously unrecognized complexity that arises from combining SO_4^{2-} sources with weathering. The inversion results for the discrepant samples

in scenario AB-1 tend to have many simulations where silicate inputs dominate over carbonate inputs, with either a long tail to high values of R or even a second mode at elevated values of R. About 25% to 50% of simulations for these samples predict very strong dominance of either silicate or carbonate inputs.

We hypothesize that the differences in R between AB-1 and AB-5 arise from the low ratios of $2\chi^{riv}_{SO_4^{2-}}/\left(2\chi^{riv}_{Ca^{2+}} + 2\chi^{riv}_{Mg^{2+}} + \chi^{riv}_{Na^{+}}\right)$ in the problematic samples. Because successful simulations for these samples in AB-1 requires MEANDIR to select a low $2\chi^{s}_{FeS_2\ SO_4^{2-}}/\chi^{s}_{\Sigma^{+}}$ ratio for either the carbonate or silicate end-members, but the inversion is unlikely to select low $2\chi^{s}_{FeS_2\ SO_4^{2-}}/\chi^{s}_{\Sigma^{+}}$ ratios for both end-members, successful model results have a tendency to be dominated by only one weathering lithology. For samples where the required combination of ratios is more likely to occur for the silicate end-member than the carbonate end-member, MEANDIR finds that the median value of R reflects silicate inputs. As a result, for some samples the median value of R in AB-1 disagrees with that of AB-5 and with $2\chi^{riv}_{Ca^{2+}}/\chi^{riv}_{Na^{+}}$. We test the existence of such a statistical artifact in scenario AB-1 by considering an additional scenario, AB-6, which is identical to AB-1 except the silicate and carbonate end-members are limited to have $2\chi^{s}_{FeS_2\ SO_4^{2-}}/\chi^{s}_{\Sigma^{+}}$ ratios between 0 and 0.15 rather than between 0 and 1 (table 7). This smaller range allows the inversion model to more often select two low values of $2\chi^{s}_{FeS_2\ SO_4^{2-}}/\chi^{s}_{\Sigma^{+}}$. For the problematic samples, the median R values in AB-6 are a stronger match to those of AB-5 than the median R values of scenario AB-1 (fig. 8C). However, note that the reduced range of $2\chi^{s}_{FeS_2\ SO_4^{2-}}/\chi^{s}_{\Sigma^{+}}$ in AB-6 forces the precipitation and evaporite end-members to source $\chi^{riv}_{SO_4^{2-}}$ that is attributed to FeS_2 oxidation in AB-1, resulting in large reductions to the inversion-constrained median values of Z.

These results demonstrate that, for samples with low ratios of $2\chi^{riv}_{SO_4^{2-}}/\chi^{riv}_{\Sigma^{+}}$, inversion models that combine FeS_2 oxidation with weathering can be subject to probabilistic influences reflecting the likelihood of selecting a required combination of end-member chemical ratios. In contrast, when quantifying $\chi^{riv}_{excess\ SO_4^{2-}}$ or $\chi^{other}_{SO_4^{2-}}$, the inversion is not constrained by selecting low ratios of $2\chi^{s}_{FeS_2\ SO_4^{2-}}/\chi^{s}_{\Sigma^{+}}$ and results are in stronger agreement with expectations from $2\chi^{riv}_{Ca^{2+}}/\chi^{riv}_{Na^{+}}$ (fig. 8A). Our comparison thus shows that it is preferable to treat FeS_2 oxidation independent of weathering. This result also stresses the importance of considering the full range of model results, as opposed to only the median of the inversion-constrained distributions.

In the data of Torres and others (2016), scenario MT-5 (SO_4^{2-} in end-members), scenario MT-6 (excess SO_4^{2-}), and scenario MT-7 (other SO_4^{2-}) all return similar values for R and Z (fig. 8D). The major difference among the three scenarios is that samples with the highest values of Z in scenarios MT-6 and MT-7 have lower values of Z in scenario MT-5. This downward shift reflects that, in scenario MT-5, it is impossible to attain Z values substantially above 1 because the carbonate and silicate end-members are limited to have $2\chi^{s}_{FeS_2\ SO_4^{2-}}/\chi^{s}_{\Sigma^{+}}$ values between 0 and 1. However, $Z > 1$ is a possible outcome in scenarios MT-6 and MT-7. We note that the inversion approach used in scenario MT-5 could be modified to have end-member $2\chi^{s}_{FeS_2\ SO_4^{2-}}/\chi^{s}_{\Sigma^{+}}$ values exceed 1, if motivated by observations of $2\chi^{riv}_{SO_4^{2-}}/\chi^{riv}_{\Sigma^{+}} > 1$. That is, charge equivalent $\chi^{riv}_{SO_4^{2-}}$ exceeding $\chi^{riv}_{\Sigma^{+}}$ is sometimes observed in natural waters and need not reflect analytical error if, for example, the samples also have low pH values or high iron concentrations where $\chi^{riv}_{\Sigma^{+}}$ only includes alkali and alkaline earth cations.

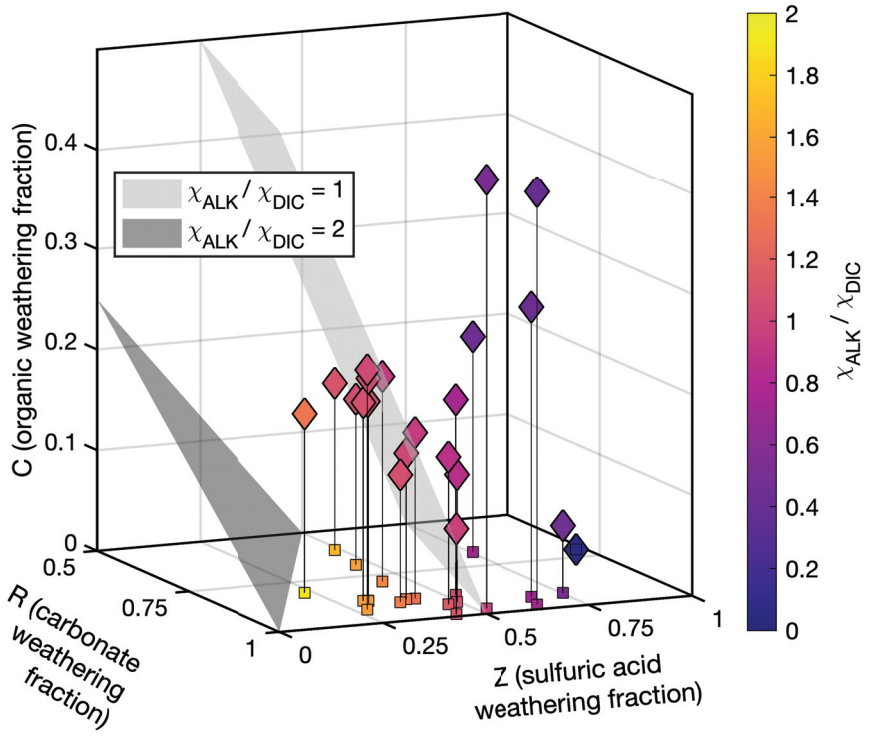

Fig. 9. Results for the simultaneous quantification of silicate weathering, carbonate weathering, precipitation inputs, FeS_2 oxidation, C_{org} oxidation, and gas exchange in the Mackenzie River basin. Carbonate weathering fraction (R), sulfuric acid weathering fraction (Z), and organic carbon oxidation relative to weathering alkalinity (C) color-coded by χ_{ALK}/χ_{DIC}, with indicated planes for $\chi_{ALK}/\chi_{DIC} = 1$ and $\chi_{ALK}/\chi_{DIC} = 2$. All river water samples have $\chi_{ALK}/\chi_{DIC} < 2$, indicating that chemical weathering upstream of these sample sites increases atmospheric CO_2 over timescales longer than carbonate burial. Vertical lines connect results accounting for non-zero C (diamonds) with results only considering the R-Z plane (squares); note the lower χ_{ALK}/χ_{DIC} ratios of the calculation accounting for C_{org} oxidation. Plotted points are the medians of accepted inversion results. All data underlying this inversion are from Horan and others (2019).

Calculated values of FeS_2 $\delta^{34}S$ agree strongly among scenarios MT-5, MT-6, and MT-7 (fig. 8E). Overall, despite observed values not being used to constrain the inversion, the calculated values of FeS_2 $\delta^{34}S$ are generally in agreement with measured bedrock $\delta^{34}S$. MEANDIR predicts values of FeS_2 $\delta^{34}S$ ranging from -4.8‰ to 7.0‰, reaching values approximately 6‰ higher than the measured range of -5‰ to 1‰ (Torres and others, 2016). Notably, most of the samples with FeS_2 $\delta^{34}S$ values higher than the measured range are from the Foreland-floodplain and may include sedimentary inputs that are not resolved in the inversion model.

Quantifying Petrogenic C_{org} Oxidation

FeS_2 and C_{org} oxidation have important roles in chemical weathering and the global carbon cycle (Torres and others, 2016; Horan and others, 2019). Using normalizations to $\chi^{riv}_{\Sigma^+ + ALK + DIC}$ and $\chi^{riv}_{\Sigma^+ + SO_4^{2-} + DIC}$, as well as the R-Z framework extended to include C, we simultaneously evaluate conventional silicate weathering, FeS_2 oxidation, and C_{org} oxidation in the catchment of the Mackenzie River using the data of Horan and others (2019). In particular, the Horan and others (2019) dataset includes

measurements of χ^{riv}_{Re} that enable quantification of C_{org} oxidation. To do so, we define a C_{org} oxidation end-member with a well-defined ratio of $\chi^{C_{org}\ ox.}_{Re} / \chi^{C_{org}\ ox.}_{\Sigma^+ + SO_4^{2-} + DIC}$ (table 13).

Model results indicate dominance of carbonate weathering over silicate weathering in the Mackenzie River (fig. 9), with substantial H_2SO_4 weathering (Calmels and others, 2007). Values of C range from 0% to 43%. The χ_{ALK}/χ_{DIC} associated with chemical weathering in the catchment upstream of each sample is calculated from R, Z, and C (fig. 9, with indicated planes for $\chi_{ALK}/\chi_{DIC} = 1$ and $\chi_{ALK}/\chi_{DIC} = 2$). All river water samples represent weathering systems with $\chi_{ALK}/\chi_{DIC} < 2$, indicating that weathering in the sampled catchments increases pCO_2 on timescales longer that marine carbonate burial. Moreover, several samples have $\chi_{ALK}/\chi_{DIC} < 1$, indicating weathering that results in instantaneous pCO_2 increase. Notably, our inversion does not constrain C_{org} production or burial, nor the cation or nitrogen fluxes associated with biomass cycling, meaning that it does not capture the full carbon cycle budget of the Mackenzie River. This caveat is important because accounting for C_{org} burial in the floodplain or marine sediments may alter the direction of how weathering in this system impacts atmospheric CO_2 (Horan and others, 2019). Regardless, our inversion demonstrates the ability of MEANDIR to quantify petrogenic C_{org} oxidation and FeS_2 oxidation from χ^{riv}_{Re} and $\chi^{riv}_{SO_4^{2-}}$ (Hilton and others, 2014).

CONCLUSIONS

Here we present Mixing Elements ANd Dissolved Isotopes in Rivers (MEANDIR), a set of MATLAB scripts for performing highly customizable inversion of river dissolved chemistry with Monte Carlo propagation of uncertainty. After introducing the mathematics underlying MEANDIR, we evaluate its performance using five previously published datasets (Gíslason and others, 1996; Gaillardet and others, 1999; Torres and others, 2016; Burke and others, 2018; Horan and others, 2019). Among others results, we evaluate the sensitivity of river inversion to the choice of cost function, review and compare multiple methods for the quantification of FeS_2 oxidation, extend an existing formalism to account for the oxidation of petrogenic organic carbon, and introduce a new normalization method. MEANDIR is available online for ongoing critique and development.

CODE AVAILABILITY AND DATA SOURCES

Mixing Elements ANd Dissolved Isotopes in Rivers (MEANDIR) and its user guide are available at https://github.com/PrestonCosslettKemeny/MEANDIR. The data analyzed in this study come from table 1 of Gíslason and others, (1996), table 1 of Gaillardet and others (1999), the supplementary materials of Torres and others (2016) and Burke and others (2018), and table 2 of Horan and others (2019).

ACKNOWLEDGMENTS

P.C.K. is supported by The Fannie and John Hertz Foundation Cohan/Jacobs and Stein Families Fellowship. M.A.T. gratefully acknowledges support from the Alfred. P. Sloan Foundation. Both authors thank J. Adkins for comments on an early draft of this article and A. Phillips for advice on the design of figures. We are grateful to J. Bouchez, A. Bufe, and an anonymous referee for thoughtful reviews.

REFERENCES

Aitchison, J., 1983, Principal component analysis of compositional data: Biometrika, v. 70, n. 1, p. 57–65, https://doi.org/10.1093/biomet/70.1.57

Baertschi, P., 1976, Absolute ^{18}O content of standard mean ocean water: Earth and Planetary Science Letters, v. 31, n. 3, p. 341–344, https://doi.org/10.1016/0012-821X(76)90115-1
Berner, R. A., 1971, Worldwide sulfur pollution of rivers: Journal of Geophysical Research, v. 76, n. 27, p. 6597–6600, https://doi.org/10.1029/JC076i027p06597
Bickle, M. J., Tipper, E., Galy, A., Chapman, H., and Harris, N., 2015, On discrimination between carbonate and silicate inputs to Himalayan rivers: American Journal of Science, v. 315, n. 2, p. 120–166, https://doi.org/10.2475/02.2015.02
Bickle, M. J., Chapman, H. J., Tipper, E., Galy, A., De La Rocha, C. L., and Ahmad, T., 2018, Chemical weathering outputs from the flood plain of the Ganga: Geochimica et Cosmochimica Acta, v. 225, p. 146–175, https://doi.org/10.1016/j.gca.2018.01.003
Bizzarro, M., Paton, C., Larsen, K., Schiller, M., Trinquier, A., and Ulfbeck, D., 2011, High-precision Mg-isotope measurements of terrestrial and extraterrestrial material by HR-MC-ICPMS—implications for the relative and absolute Mg-isotope composition of the bulk silicate Earth: Journal of Analytical Atomic Spectrometry, v. 26, n. 3, p. 565–577, https://doi.org/10.1039/c0ja00190b
Blair, N. E., and Aller, R. C., 2012, The fate of terrestrial organic carbon in the marine environment: Annual Review of Marine Science, v. 4, p. 401–423, https://doi.org/10.1146/annurev-marine-120709-142717
Blattmann, T. M., Wang, S.-L., Lupker, M., Märki, L., Haghipour, N., Wacker, L., Chung, L.-H., Bernasconi, S. M., Plötze, M., and Eglinton, T. I., 2019, Sulphuric acid-mediated weathering on Taiwan buffers geological atmospheric carbon sinks: Scientific reports, v. 9, 2945, https://doi.org/10.1038/s41598-019-39272-5
Bolton, E. W., Berner, R. A., and Petsch, S. T., 2006, The weathering of sedimentary organic matter as a control on atmospheric O_2: II. Theoretical modeling: American Journal of Science, v. 306, n. 8, p. 575–615, https://doi.org/10.2475/08.2006.01
Bouchez, J., Beyssac, O., Galy, V., Gaillardet, J., France-Lanord, C., Maurice, L., and Moreira-Turcq, P., 2010, Oxidation of petrogenic organic carbon in the Amazon floodplain as a source of atmospheric CO_2: Geology, v. 38, n. 3, p. 255–258, https://doi.org/10.1130/G30608.1
Bouchez, J., von Blanckenburg, F., and Schuessler, J. A., 2013, Modeling novel stable isotope ratios in the weathering zone: American Journal of Science, v. 313, n. 4, p. 267–308, https://doi.org/10.2475/04.2013.01
Brand, W. A., Coplen, T. B., Vogl, J., Rosner, M., and Prohaska, T., 2014, Assessment of international reference materials for isotope-ratio analysis (IUPAC Technical Report): Pure and Applied Chemistry, v. 86, n. 3, p. 425-467, https://doi.org/10.1515/pac-2013-1023
Burke, A., Present, T. M., Paris, G., Rae, E. C. M., Sandilands, B. H., Gaillardet, J., Peucker-Ehrenbrink, B., Fischer, W. W., McClelland, J. W., Spencer, R. G. M., and Voss, B. M., 2018, Sulfur isotopes in rivers: Insights into global weathering budgets, pyrite oxidation, and the modern sulfur cycle: Earth and Planetary Science Letters, v. 496, p. 168–177, https://doi.org/10.1016/j.epsl.2018.05.022
Calmels, D., Gaillardet, J., Brenot, A., and France-Lanord, C., 2007, Sustained sulfide oxidation by physical erosion processes in the Mackenzie River basin: Climatic perspectives: Geology, v. 35, n. 11, p. 1003–1006, https://doi.org/10.1130/G24132A.1
Caves, J. K., Jost, A. B., Lau, K. V., and Maher, K., 2016, Cenozoic carbon cycle imbalances and a variable weathering feedback: Earth and Planetary Science Letters, v. 450, p. 152–163, https://doi.org/10.1016/j.epsl.2016.06.035
Chang, T., and Li, W., 1990, A calibrated measurement of the atomic weight of carbon: Chinese Science Bulletin, v. 35, n. 4, p. 290–296, https://doi.org/https://doi.org/10.1360/sb1990-35-4-290
Christophersen, N., and Hooper, R. P., 1992, Multivariate analysis of stream water chemical data: The use of principal components analysis for the end-member mixing problem: Water Resources Research, v. 28, n. 1, p. 99–107, https://doi.org/10.1029/91WR02518
Daëron, M., Blamart, D., Peral, M., and Affek, H. P., 2016, Absolute isotopic abundance ratios and the accuracy of Δ_{47} measurements: Chemical Geology, v. 442, p. 83–96, https://doi.org/10.1016/j.chemgeo.2016.08.014
de Souza, G. F., Reynolds, B. C., Kiczka, M., and Bourdon, B., 2010, Evidence for mass-dependent isotopic fractionation of strontium in a glaciated granitic watershed: Geochimica et Cosmochimica Acta, v. 74, n. 9, p. 2596–2614, https://doi.org/10.1016/j.gca.2010.02.012
Ding, T., Valkiers, S., Kipphardt, H., De Bièvre, P., Taylor, P. D. P., Gonfiantini, R., and Krouse, R., 2001, Calibrated sulfur isotope abundance ratios of three IAEA sulfur isotope reference materials and V-CDT with a reassessment of the atomic weight of sulfur: Geochimica et Cosmochimica Acta, v. 65, n. 15, p. 2433–2437, https://doi.org/10.1016/S0016-7037(01)00611-1
Dunlea, A. G., and Murray, R. W., 2015, Optimization of end-members used in multiple linear regression geochemical mixing models: Geochemistry, Geophysics, Geosystems, v. 16, n. 11, p. 4021–4027, https://doi.org/10.1002/2015GC006132
Edmond, J. M., Measures, C., McDuff, R. E., Chan, L. H., Collier, R., Grant, B., Gordon, L. I., and Corliss, J. B., 1979a, Ridge crest hydrothermal activity and the balances of the major and minor elements in the ocean: The Galapagos data: Earth and Planetary Science Letters, v. 46, n. 1, p. 1–18. https://doi.org/10.1016/0012-821X(79)90061-X
Edmond, J. M., Corliss, J. B., and Gordon, L. I., 1979b, Ridge Crest-Hydrothermal Metamorphism at the Galapagos Spreading Center and Reverse Weathering : Deep Drilling Results in the Atlantic Ocean: Ocean Crust, v. 2, p. 383–390, https://doi.org/https://doi.org/10.1029/ME002p0383
France-Lanord, C., and Derry, L. A., 1997, Organic carbon burial forcing of the carbon cycle from Himalayan erosion: Nature, v. 390, n. 6655, p. 65–67, https://doi.org/10.1038/36324
Gaillardet, J., Dupré, B., Louvat, P., and Allegre, C. J., 1999, Global silicate weathering and CO_2 consumption rates deduced from the chemistry of large rivers: Chemical geology, v. 159, n. 1–4, p. 3–30, https://doi.org/10.1016/S0009-2541(99)00031-5
Galy, A., and France-Lanord, C., 1999, Weathering processes in the Ganges–Brahmaputra basin and the riverine alkalinity budget: Chemical Geology, v. 159, n. 1–4, p. 31–60, https://doi.org/10.1016/S0009-2541(99)00033-9

Genereux, D., 1998, Quantifying uncertainty in tracer-based hydrograph separations: Water Resources Research, v. 34, n. 4, p. 915–919, https://doi.org/10.1029/98WR00010
Georg, R. B., Reynolds, B. C., West, A. J., Burton, K. W., and Halliday, A. N., 2007, Silicon isotope variations accompanying basalt weathering in Iceland: Earth and Planetary Science Letters, v. 261, n. 3–4, p. 476–490, https://doi.org/10.1016/j.epsl.2007.07.004
Gíslason, S. R., Arnorsson, S., and Armannsson, H., 1996, Chemical weathering of basalt in Southwest Iceland; effects of runoff, age of rocks and vegetative/glacial cover: American Journal of Science, v. 296, n. 8, p. 837–907, https://doi.org/10.2475/ajs.296.8.837
Hartmann, J., Lauerwald, R., and Moosdorf, N., 2014, A brief overview of the GLObal RIver CHemistry Database, GLORICH: Procedia Earth and Planetary Science, v. 10, p. 23–27, https://doi.org/10.1016/j.proeps.2014.08.005
He, Z., Unger-Shayesteh, K., Vorogushyn, S., Weise, S. M., Duethmann, D., Kalashnikova, O., Gafurov, A., and Merz, B., 2020, Comparing Bayesian and traditional end-member mixing approaches for hydrograph separation in a glacierized basin: Hydrology and Earth System Sciences, v. 24, n. 6, p. 3289–3309, https://doi.org/10.5194/hess-24-3289-2020
Hemingway, J. D., Olson, H., Turchyn, A. V., Tipper, E. T., Bickle, M. J., and Johnston, D. T., 2020, Triple oxygen isotope insight into terrestrial pyrite oxidation: Proceedings of the National Academy of Sciences of the United States of America, v. 117, n. 14, p. 7650–7657, https://doi.org/10.1073/pnas.1917518117
Hilton, R. G., and West, A. J., 2020, Mountains, erosion and the carbon cycle: Nature Reviews Earth & Environment, v. 1, n. 6, p. 284–299, https://doi.org/10.1038/s43017-020-0058-6
Hilton, R. G., Gaillardet, J., Calmels, D., and Birck, J. L., 2014, Geological respiration of a mountain belt revealed by the trace element rhenium: Earth and Planetary Science Letters, v. 403, p. 27–36, https://doi.org/10.1016/j.epsl.2014.06.021
Hindshaw, R. S., Bourdon, B., von Strandmann, P. A. E. P., Vigier, N., and Burton, K. W., 2013, The stable calcium isotopic composition of rivers draining basaltic catchments in Iceland: Earth and Planetary Science Letters, v. 374, p. 173–184, https://doi.org/10.1016/j.epsl.2013.05.038
Horan, K., Hilton, R. G., Dellinger, M., Tipper, E., Galy, V., Calmels, D., Selby, D., Gaillardet, J., Ottley, C. J., Parsons, D. R., and Burton, K. W., 2019, Carbon dioxide emissions by rock organic carbon oxidation and the net geochemical carbon budget of the Mackenzie River Basin: American Journal of Science, v. 319, n. 6, p. 473–499, https://doi.org/10.2475/06.2019.02
Hubbard, C. G., Black, S., and Coleman, M. L., 2009, Aqueous geochemistry and oxygen isotope compositions of acid mine drainage from the Río Tinto, SW Spain, highlight inconsistencies in current models: Chemical Geology, v. 265, n. 3–4, p. 321–334, https://doi.org/10.1016/j.chemgeo.2009.04.009
Jacobson, A. D., Blum, J. D., and Walter, L. M., 2002, Reconciling the elemental and Sr isotope composition of Himalayan weathering fluxes: insights from the carbonate geochemistry of stream waters: Geochimica et Cosmochimica Acta, v. 66, n. 19, p. 3417–3429. https://doi.org/10.1016/S0016-7037(02)00951-1
Kemeny, P. C., Lopez, G. I., Dalleska, N. F., Torres, M., Burke, A., Bhatt, M. P., West, A. J., Hartmann, J., and Adkins, J. F., 2021a, Sulfate sulfur isotopes and major ion chemistry reveal that pyrite oxidation counteracts CO_2 drawdown from silicate weathering in the Langtang-Trisuli-Narayani River system, Nepal Himalaya: Geochimica et Cosmochimica Acta, v. 294, p. 43–69, https://doi.org/10.1016/j.gca.2020.11.009
Kemeny, P. C., Torres, M. A., Lamb, M. P., Webb, S. M., Dalleska, N., Cole, T., Hou, Y., Marske, J., Adkins, J. F., and Fischer, W. W., 2021b, Organic sulfur fluxes and geomorphic control of sulfur isotope ratios in rivers: Earth and Planetary Science Letters, v. 562, p. 116838, https://doi.org/10.1016/j.epsl.2021.116838
Lerman, A., Wu, L., and Mackenzie, F. T., 2007, CO_2 and H_2SO_4 consumption in weathering and material transport to the ocean, and their role in the global carbon balance: Marine Chemistry, v. 106, n. 1–2, p. 326–350, https://doi.org/10.1016/j.marchem.2006.04.004
Li, G., and Elderfield, H., 2013, Evolution of carbon cycle over the past 100 million years: Geochimica et Cosmochimica Acta, v. 103, p. 11–25, https://doi.org/10.1016/j.gca.2012.10.014
Mayer, A. J., and Wieser, M. E., 2014, The absolute isotopic composition and atomic weight of molybdenum in SRM 3134 using an isotopic double-spike: Journal of Analytical Atomic Spectrometry, v. 29, n. 1, p. 85–94, https://doi.org/10.1039/C3JA50164G
Miesch, A. T., 1976, Q-mode factor analysis of compositional data: Computers & Geosciences, v. 1, n. 3, p. 147–159, https://doi.org/10.1016/0098-3004(76)90003-0
Moon, S., Chamberlain, C. P., and Hilley, G. E., 2014, New estimates of silicate weathering rates and their uncertainties in global rivers: Geochimica et Cosmochimica Acta, v. 134, p. 257–274, https://doi.org/10.1016/j.gca.2014.02.033
Moore, L. J., and Machlan, L. A., 1972, High-accuracy determination of calcium in blood serum by isotope dilution mass spectrometry: Analytical Chemistry, v. 44, n. 14, p. 2291–2296, https://doi.org/10.1021/ac60322a014
Moulton, K. L., West, J., and Berner, R.A., 2000, Solute flux and mineral mass balance approaches to the quantification of plant effects on silicate weathering: American Journal of Science, v. 300, n. 7, p. 539–570, https://doi.org/10.2475/ajs.300.7.539
Négrel, P., Allègre, C. J., Dupré, B., and Lewin, E., 1993, Erosion sources determined by inversion of major and trace element ratios and strontium isotopic ratios in river water: the Congo Basin case: Earth and Planetary Science Letters, v. 120, n. 1–2, p. 59–76, https://doi.org/10.1016/0012-821X(93)90023-3
Parnell, A. C., Inger, R., Bearhop, S., and Jackson, A. L., 2010, Source partitioning using stable isotopes: coping with too much variation: PLoS ONE, v. 5, n. 3, p. e9672, https://doi.org/10.1371/journal.pone.0009672
Phillips, D. L., and Gregg, J. W., 2001, Uncertainty in source partitioning using stable isotopes: Oecologia, v. 127, n. 2, p. 171–179, https://doi.org/10.1007/s004420000578
Phillips, D. L., and Gregg, J. W., 2003, Source partitioning using stable isotopes: coping with too many sources: Oecologia, v. 136, n. 2, p. 261–269, https://doi.org/10.1007/s00442-003-1218-3

Pisias, N. G., Murray, R. W., and Scudder, R. P., 2013, Multivariate statistical analysis and partitioning of sedimentary geochemical data sets: General principles and specific MATLAB scripts: Geochemistry, Geophysics, Geosystems, v. 14, n. 10, p. 4015–4020, https://doi.org/10.1002/ggge.20247

Polsenaere, P., and Abril, G., 2012, Modelling CO_2 degassing from small acidic rivers using water pCO_2, DIC and δ^{13}C-DIC data: Geochimica et Cosmochimica Acta, v. 91, p. 220–239, https://doi.org/10.1016/j.gca.2012.05.030

Qi, H. P., Taylor, P. D. P., Berglund, M., and De Bièvre, P., 1997, Calibrated measurements of the isotopic composition and atomic weight of the natural Li isotopic reference material IRMM-016: International Journal of Mass Spectrometry and Ion Processes, v. 171, n. 1–3, p. 263–268, https://doi.org/10.1016/S0168-1176(97)00125-0

Scheingross, J. S., Repasch, M. N., Hovius, N., Sachse, D., Lupker, M., Fuchs, M., Halvy, I., Gröcke, D. R., Golombek, N. Y., Haghipour, N., Eglinton, T. I., Orfeo, O., and Schleicher, A. M., 2021, The fate of fluvially-deposited organic carbon during transient floodplain storage: Earth and Planetary Science Letters, v. 561, p. 116822, https://doi.org/10.1016/j.epsl.2021.116822

Spence, J., and Telmer, K., 2005, The role of sulfur in chemical weathering and atmospheric CO_2 fluxes: Evidence from major ions, $\delta^{13}C_{DIC}$, and $\delta^{34}S_{SO4}$ in rivers of the Canadian Cordillera: Geochimica et Cosmochimica Acta, v. 69, n. 23, p. 5441–5458, https://doi.org/10.1016/j.gca.2005.07.011

Stallard, R. F., and Edmond, J. M., 1983, Geochemistry of the Amazon: 2. The influence of geology and weathering environment on the dissolved load: Journal of Geophysical Research: Oceans, v. 88, n. C14, p. 9671–9688, https://doi.org/10.1029/JC088iC14p09671

Stefánsson, A., and Gislason, S. R., 2001, Chemical weathering of basalts, Southwest Iceland: effect of rock crystallinity and secondary minerals on chemical fluxes to the ocean: American Journal of Science, v. 301, n. 6, p. 513–556, https://doi.org/https://doi.org/10.2475/ajs.301.6.513

Taylor, P. D. P., Maeck, R., and De Biévre, P., 1992, Determination of the absolute isotopic composition and atomic weight of a reference sample of natural iron: International Journal of Mass Spectrometry and Ion Processes, v. 121, p. 111-125, https://doi.org/10.1016/0168-1176(92)80075-C

Thorpe, M. T., Hurowitz, J. A., and Dehouck, E., 2019, Sediment geochemistry and mineralogy from a glacial terrain river system in southwest Iceland: Geochimica et Cosmochimica Acta, v. 263, p. 140–166, https://doi.org/10.1016/j.gca.2019.08.003

Tipper, E. T., Bickle, M. J., Galy, A., West, A. J., Pomiès, C., and Chapman, H. J., 2006, The short term climatic sensitivity of carbonate and silicate weathering fluxes: Insight from seasonal variations in river chemistry: Geochimica et Cosmochimica Acta, v. 70, n. 11, p. 2737–2754, https://doi.org/10.1016/j.gca.2006.03.005

Torres, M. A., West, A. J., and Clark, K. E., 2015, Geomorphic regime modulates hydrologic control of chemical weathering in the Andes–Amazon: Geochimica et Cosmochimica Acta, v. 166, p. 105–128, https://doi.org/10.1016/j.gca.2015.06.007

Torres, M. A., West, A. J., Clark, K. E., Paris, G., Bouchez, J., Ponton, C., Feakins, S. J., Galy, V., and Adkins, J. F., 2016, The acid and alkalinity budgets of weathering in the Andes–Amazon system: Insights into the erosional control of global biogeochemical cycles: Earth and Planetary Science Letters, v. 450, p. 381–391, https://doi.org/10.1016/j.epsl.2016.06.012

Turowski, J. M., Hilton, R. G., and Sparkes, R., 2016, Decadal carbon discharge by a mountain stream is dominated by coarse organic matter: Geology, v. 44, n. 1, p. 27–30, https://doi.org/10.1130/G37192.1

Urey, H. C., 1952, On the early chemical history of the earth and the origin of life: Proceedings of the National Academy of Sciences of the United States of America, v. 38, n. 4, p. 351–363, https://doi.org/10.1073/pnas.38.4.351

Valkiers, S., Ding, T., Inkret, M., Ruße, K., and Taylor, P., 2005, Silicon isotope amount ratios and molar masses for two silicon isotope reference materials: IRMM-018a and NBS28: International Journal of Mass Spectrometry, v. 242, n. 2–3, p. 319–321, https://doi.org/10.1016/j.ijms.2004.11.027

Vigier, N., Gislason, S. R., Burton, K. W., Millot, R., and Mokadem, F., 2009, The relationship between riverine lithium isotope composition and silicate weathering rates in Iceland: Earth and Planetary Science Letters, v. 287, n. 3–4, p. 434–441. https://doi.org/10.1016/j.epsl.2009.08.026

Walker, J. C. G., Hays, P. B., and Kasting, J. F., 1981, A negative feedback mechanism for the long-term stabilization of Earth's surface temperature: Journal of Geophysical Research: Oceans, v. 86, n. C10, p. 9776–9782, https://doi.org/10.1029/JC086iC10p09776

West, A. J., Lin, C. W., Lin, T. C., Hilton, R. G., Liu, S. H., Chang, C.-T., Lin, K.-C., Galy, E., Sparkes, R. B., and Hovius, N., 2011, Mobilization and transport of coarse woody debris to the oceans triggered by an extreme tropical storm: Limnology and Oceanography, v. 56, n. 1, p. 77–85, https://doi.org/10.4319/lo.2011.56.1.0077

Zeebe, R. E., and Wolf-Gladrow, D., 2001, CO_2 in seawater: equilibrium, kinetics, isotopes: Amsterdam, The Netherlands, Elsevier Oceanography Series, v. 65, p. 1–346.